

**THE INTERFACIAL THERMAL CONDUCTANCE OF EPITAXIAL  
METAL-SEMICONDUCTOR INTERFACES**

by  
Ning Ye

A dissertation submitted to the Faculty of the University of Delaware in partial fulfillment of the requirements for the degree of Doctor of Philosophy in Mechanical Engineering

Summer 2017

© 2017 Ning Ye  
All Rights Reserved

**THE INTERFACIAL THERMAL CONDUCTANCE OF EPITAXIAL  
METAL-SEMICONDUCTOR INTERFACES**

by

Ning Ye

Approved: \_\_\_\_\_

Ajay K. Prasad, Ph.D.

Chair of the Department of Mechanical Engineering

Approved: \_\_\_\_\_

Babatunde A. Ogunnaike, Ph.D.

Dean of the College of Engineering

Approved: \_\_\_\_\_

Ann L. Ardis, Ph.D.

Senior Vice Provost for Graduate and Professional Education

I certify that I have read this dissertation and that in my opinion it meets the academic and professional standard required by the University as a dissertation for the degree of Doctor of Philosophy.

Signed: \_\_\_\_\_  
Joseph P. Feser, Ph.D.  
Professor in charge of dissertation

I certify that I have read this dissertation and that in my opinion it meets the academic and professional standard required by the University as a dissertation for the degree of Doctor of Philosophy.

Signed: \_\_\_\_\_  
Ajay K. Prasad, Ph.D.  
Member of dissertation committee

I certify that I have read this dissertation and that in my opinion it meets the academic and professional standard required by the University as a dissertation for the degree of Doctor of Philosophy.

Signed: \_\_\_\_\_  
M. Zubaer Hossain, Ph.D.  
Member of dissertation committee

I certify that I have read this dissertation and that in my opinion it meets the academic and professional standard required by the University as a dissertation for the degree of Doctor of Philosophy.

Signed: \_\_\_\_\_  
Chaoying Ni, Ph.D.  
Member of dissertation committee

## ACKNOWLEDGEMENTS

It has been six years since I first came to United States and started my degree in University of Delaware. Actually, I did not expect this would take so long when I just started, but the experience here would be invaluable memories and benefit me for the rest of my life.

First of all, I would like to thank my advisor Dr. Joseph Feser, who helps me out of the hardest time during my Ph.D. study and guides me patiently into this new field. I am always impressed by his broad and deep knowledge in both basic science and practical applications of this project. His humor and valuable suggestions benefit my graduation education and will continue to strengthen me in the future. Also, I am grateful to all my committee members, Dr. Ajay Prasad, Dr. Zubaer Hossain and Dr. Chaoying Ni, for spending their valuable time on reading and giving suggestions on this thesis.

Many thanks also go to group members from Microscale Thermal Transport Lab, Rohit Kakodkar, Vineet Unni, Kieran Tracy and Zachary Present. It has been a lot of fun to work with you guys and thank you for your help in my research. Some of the work in thesis could not be finished without the help from my collaborators Dr. Sridhar Sadasivam, Dr. Timothy Fisher, Tianshi Wang, Dr. Anderson Janotti, Jing Zhang, Dr. Joshua Zide, Dr. Jeremy Schroeder. Thank you for your efforts to help my research. I have also benefited from my former advisor Joshua Hertz and former group members Weida Shen, Jun Jiang, Benjamin McNealy, Philips Zandona, from who we inherited a fancy PVD system and I learnt thin film growth. Without that, this work is impossible to be finished.

I would also like to thank my advisors former colleague Gregory Hohensee, who helps me get a summer intern opportunity in Western Digital Company in summer

2016. I am also appreciated the help of my manager Antony Ajay, mentor Kumar Srinivasan and other colleagues Will Chen, Hua Yuan, Ho Hoan, Jinming Liu and Jing Jin in WDC to teach me state of the art techniques in the industry.

Last but not least, I would like to say thanks to my families for their unconditional supports for all these years. Especially, I want to thank my wife Xinran, for her encouragement when I was frustrating and all the happiness she gave to me. I want to thank my parents for always believing in me and blessing me.

## TABLE OF CONTENTS

<b>LIST OF TABLES</b> . . . . .	<b>ix</b>
<b>LIST OF FIGURES</b> . . . . .	<b>x</b>
<b>ABSTRACT</b> . . . . .	<b>xix</b>
 <b>Chapter</b>	
<b>1 INTRODUCTION</b> . . . . .	<b>1</b>
1.1 Thermal conduction: a microscopic perspective . . . . .	1
1.2 Introduction to phonons and phonon transport theory . . . . .	3
1.3 The importance of interfacial thermal conductance . . . . .	6
1.4 History of interfacial thermal resistance experiments . . . . .	7
1.5 Theory of interfacial thermal resistance . . . . .	14
1.6 Outline of thesis . . . . .	17
 <b>2 EXPERIMENTAL AND THEORETICAL METHODS</b> . . . . .	 <b>21</b>
2.1 Time-domain thermorefectance . . . . .	21
2.2 Data modeling by full phonon dispersion DMM . . . . .	31
2.2.1 Full phonon dispersion calculation . . . . .	31
2.2.2 Phonon thermal interface conductance modeling . . . . .	32
2.2.3 Diffuse mismatch modeling of transmission coefficient . . . . .	33
2.2.4 The radiative limit for interfacial heat transport . . . . .	34
2.3 Magnetron sputtering . . . . .	35
2.4 X-ray diffraction (XRD) and X-ray reflectivity (XRR) . . . . .	36
2.5 Electronic thermal conductivity measurement . . . . .	37
2.6 Transmission electron microscopy (TEM) . . . . .	38

<b>3</b>	<b>THERMAL TRANSPORT ACROSS METAL SILICIDE-SILICON INTERFACES: AN EXPERIMENTAL COMPARISON BETWEEN EPITAXIAL AND NON-EPITAXIAL INTERFACES</b>	<b>39</b>
3.1	Motivation . . . . .	39
3.2	Experimental . . . . .	41
3.2.1	Epitaxial silicide growth . . . . .	41
3.2.2	Transport characterization . . . . .	45
3.3	Modeling . . . . .	49
3.4	Results and discussion . . . . .	53
3.4.1	ITC of epitaxial and non-epitaxial silicide-silicon interfaces . .	53
3.4.2	The effect of substrate carrier concentration . . . . .	59
3.5	Summary . . . . .	60
<b>4</b>	<b>THERMAL CONDUCTANCE OF EPITAXIAL <math>\text{NiAl}_{1-x}\text{Ga}_x</math>-GAAS INTERFACES: A STUDY OF PHONON BAND ENGINEERING</b>	<b>63</b>
4.1	Motivation . . . . .	63
4.2	Experiment and modeling . . . . .	64
4.3	Results and discussion . . . . .	68
4.4	Summary . . . . .	74
<b>5</b>	<b>GROUP IV EPITAXIAL METAL NITRIDES SYSTEMS WITH ULTRAHIGH INTERFACIAL THERMAL CONDUCTANCE</b>	<b>75</b>
5.1	Motivation . . . . .	75
5.2	Experiment . . . . .	77
5.3	Results and discussion . . . . .	81
5.4	Summary . . . . .	89
<b>6</b>	<b>MULTIVALLEY III-V ALLOYS FOR IMPROVED THERMOELECTRICS</b>	<b>90</b>
6.1	Motivation . . . . .	90

6.2	Experiment . . . . .	93
6.2.1	Sample preparation . . . . .	93
6.2.2	Seebeck coefficient stage designing and assembling . . . . .	93
6.2.3	TE properties characterization . . . . .	95
6.3	Results and discussion . . . . .	96
6.4	Summary . . . . .	99
6.5	Future work . . . . .	100
<b>7</b>	<b>CREATION OF ION DEFECTS IN TRANSITION METAL FREE <math>K_2NiF_4</math> STRUCTURE . . . . .</b>	<b>101</b>
7.1	Motivation . . . . .	101
7.2	Experiments . . . . .	103
7.2.1	Synthesis and structural characterization . . . . .	103
7.2.2	Conductivity measurement . . . . .	104
7.3	Results and discussions . . . . .	105
7.4	Summary . . . . .	125
<b>8</b>	<b>CONCLUSIONS AND FUTURE WORK . . . . .</b>	<b>127</b>
8.1	Conclusions . . . . .	127
8.2	Future work . . . . .	129
	<b>BIBLIOGRAPHY . . . . .</b>	<b>131</b>
	<b>Appendix</b>	
<b>A</b>	<b>REPRINT PERMISSION LIST . . . . .</b>	<b>146</b>

## LIST OF TABLES

3.1	Calculated Optical Absorption Depth of Silicides . . . . .	46
3.2	Silicide properties at 300K . . . . .	48
3.3	DFPT Details for $\text{CoSi}_2$ / Si interface modeling . . . . .	51

## LIST OF FIGURES

1.1	(a) Schematic of 1-d monoatomic chain connected with springs; (b) Schematic of 1-d diatomic chain connected with springs . . . . .	3
1.2	(a) Plot of phonon dispersion $\omega(k)$ with $k$ vector for 1-d monoatomic chain; (b) Plot of phonon dispersion $\omega(k)$ with $k$ vector for 1-d diatomic chain . . . . .	5
1.3	(a) Top view of 3-omega method sample setup; (b) pump-probe method optical setup, reprinted from reference[1] . . . . .	11
1.4	Schematic of specular and diffuse scattering assumptions in the acoustic and diffuse mismatch models respectively. In the AMM, the reflected and transmitted waves have a definite angle determined from Snells law. In the DMM, phonon is scattered into a state with equal probability to all existing states of the same frequency as the incident phonon in either side of the interface . . . . .	14
1.5	Schematic of various mechanisms involved in heat transfer between the dominant energy carriers, i.e., electrons in the metal and phonons in the semiconductor. Phonon-phonon energy transfer across the interface could involve elastic and inelastic interfacial scattering processes. Electron-phonon coupling could involve coupling between electrons in the metal with phonons in the metal and with phonons in the semiconductor. Reprinted from reference [2] . . . . .	16
2.1	The optical setup of our time domain thermorefectance system . .	22

2.2	(a) Mode-locked pump laser with pulses before modulation; (b) Pump laser pulse after electro-optic modulation; (c) Modulated pump laser arrives on the sample surface and generates a heat response on the surface of the sample; (d) Probe pulses arrives on the sample with a time difference of $\tau$ and picks up reflectance; (e) half of the probe pulses picks out unheated reflectance signal and the other half picks heated reflectance signal, the difference of the reflectance signal due to heating is the thermorelectance signal, which with a characteristic frequency of the modulation frequency . . . . .	25
2.3	(a) Total spectrum of the laser before all the filters (black), pump beam spectrum after the tilting filter_1 (red), probe beam spectrum after filter_2 (blue), probe beam spectrum after filter_3 (magenta). Due to the high power density of laser beam and low limit of spectrum detector, the spectrum is collected with scattered lights. Because it is hard to keep the same scattering rate of the lights, the real ratio of intensity between different spectrum is not as shown in this figure. This figure could only represent the wavelength distribution; (b) pump beam spectrum after filter_1 before tilting (black) and after tilting (red) . . . . .	26
2.4	Typical TDTR data of Al(83nm)/SiO <sub>2</sub> (300nm)/Si wafer taken using 5 times objective with a modulation frequency of 12.6 MHz. (a) In-phase signal vs. time; (b)out-of-phase signal vs. time; (c) $-V_{in}/V_{out}$ signal vs. time . . . . .	27
2.5	Sensitivity plot of sample Al(83 nm)/SiO <sub>2</sub> (300 nm)/Si wafer with 12.6 MHz modulation frequency and 2 times objective . . . . .	29
2.6	In-phase TDTR data of Al(83 nm)/SiO <sub>2</sub> (300 nm)/Si wafer from 0 ps to 150 ps . . . . .	30
2.7	(a) The configuration of magnetron sputtering; (b) The magnetic field and electrical field near the sputtering source . . . . .	34
2.8	(a) X-ray diffraction of single crystal GaAs(100) wafer with Ni filter (red) and without Ni filter (black); (b) X-ray reflectivity of 50 nm TiN on MgO single crystal substrate . . . . .	36

3.1	(a) XRD results of CoSi <sub>2</sub> on intrinsic Si(100) and Si(111) wafer; (b) XRD results of NiSi on intrinsic Si(100) and Si(111) wafer; (c) XRD results of PtSi on intrinsic Si(100) and Si(111) wafer; (d) XRD results of CoSi <sub>2</sub> on intrinsic Si(100) and Si(111) wafer; (e) XRD phi scan of the in-plane diffraction for PtSi(020)/Si(111), NiSi(200)/Si(111) and CoSi <sub>2</sub> (111)/Si(111) samples. . . . .	42
3.2	HRTEM of an epitaxial CoSi <sub>2</sub> (111)-Si(111) interface. FFT of CoSi <sub>2</sub> and Si indicates a 180° with respect to [111] . . . . .	43
3.3	Room temperature sensitivity plots for CoSi <sub>2</sub> , TiSi <sub>2</sub> , NiSi, and PtSi vs time delay . . . . .	47
3.4	Schematic of the Si-CoSi <sub>2</sub> interface supercell with a 8B interfacial atomic configuration. The dashed rectangular boxes indicate the unit cells of bulk Si and bulk strained CoSi <sub>2</sub> . . . . .	51
3.5	The interfacial thermal conductance of CoSi <sub>2</sub> , TiSi <sub>2</sub> , NiSi and PtSi on intrinsic Si(100) and Si(111) wafer. CoSi <sub>2</sub> /Si-1, CoSi <sub>2</sub> /Si-2 and CoSi <sub>2</sub> /Si-3 represent samples made under different conditions. CoSi <sub>2</sub> /Si-1: HF treated wafer + films deposited by co-sputtering, CoSi <sub>2</sub> /Si-2: HF treated wafer + films made by reactive growth method, CoSi <sub>2</sub> /Si-3: RF bias treated wafer + films made by reactive growth method. For TiSi <sub>2</sub> , NiSi and PtSi films are made by reactive growth method on RF-bias cleaned substrates. The interfacial thermal conductance of Al/Si(100) is also attached as a reference. .	54
3.6	(a)Modeling results for CoSi <sub>2</sub> (111)-Si(111) interfaces using various models: the full-dispersion diffuse mismatch model (green), the atomistic Greens function method for interface of 8B(red) and 8A(orange) and the radiation limit (black). Experimental data at room temperature is shown for comparison (blue squares); (b)Comparison between experimental thermal interface conductance of TiSi <sub>2</sub> -Si(111) interface (blue squares), the full-dispersion DMM calculation of TiSi <sub>2</sub> (001), TiSi <sub>2</sub> (010), TiSi <sub>2</sub> (100), TiSi <sub>2</sub> (111)-Si(111) and the radiation limit (black); (c)Comparison between experimental thermal interface conductance of an epitaxial NiSi(200)-Si(111) interface (blue squares), the full-dispersion DMM calculation (green) and the radiation limit (black);(d)Comparison between experimental thermal interface conductance of an epitaxial PtSi(020)-Si(111) interface (blue squares), the full-dispersion DMM calculation (green) and the radiation limit (black). . . . .	56

3.7	Comparison of AGF simulation predictions with $\text{CoSi}_2(111)/\text{Si}(111)$ experimental results (blue squares with error bars). A (black solid curve) - Phonon-only simulation with elastic interface scattering. B (magenta circles) - Phonon-only simulation with anharmonic phonon scattering in both Si and $\text{CoSi}_2$ . C (red hexagrams) - Electrons and phonons considered in the simulation with electron-phonon energy transfer inside the metal region only. D (green diamonds) - Electrons and phonons considered in the simulation with electron-phonon energy transfer included in two (1.9 nm) unit cells of Si closest to the interface. Reprinted from our collaborator's paper[2]. . . . .	58
3.8	The substrate doping effects on the interfacial thermal conductance. The thermal conductance values are normalized with their correspondent undoped values. This includes the interfacial thermal conductance of $\text{CoSi}_2/\text{Si}(111)$ and $\text{CoSi}_2/\text{Si}(100)$ made by co-deposition, $\text{CoSi}_2/\text{Si}(111)$ , $\text{CoSi}_2/\text{Si}(100)$ , $\text{TiSi}_2/\text{Si}(111)$ , $\text{NiSi}/\text{Si}(111)$ and $\text{PtSi}/\text{Si}(111)$ made by reactive growth. * indicates that the interface is not epitaxial. (For original data please refer to Figure 3.9) . . . . .	60
3.9	Interfacial thermal conductance and wafer thermal conductivity vs. wafer doping concentration of (a) and (b) $\text{CoSi}_2$ films made by co-sputtering on HF treated Si(111) and Si(100) wafer; (c) and (d) $\text{CoSi}_2$ films made by reactive growth method on RF bias treated Si(111) and Si(100) wafers; (e), (f) and (g) $\text{TiSi}_2$ , $\text{NiSi}$ and $\text{PtSi}$ made by reactive growth method on RF treated Si(111) wafers. . . . .	62
4.1	XRD spectra of GaAs wafer (black), NiAl film (red), $\text{NiAl}_{0.5}\text{Ga}_{0.5}$ film (blue), $\text{NiAl}_{0.25}\text{Ga}_{0.75}$ film (dark cyan) and NiGa film (magenta). Curves are offset for clarity. NiX indicates the peaks from $\text{NiAl}_{1-x}\text{Ga}_x$ alloy. * indicates the contamination peaks from the single crystal substrate. . . . .	65
4.2	Sensitivity plots of NiAl (a) and NiGa (b) on GaAs at room temperature . . . . .	67
4.3	Room temperature electrical conductivity of $\text{NiAl}_{1-x}\text{Ga}_x$ alloys vs. composition . . . . .	67
4.4	Comparison of the density of states of $\text{NiAl}_{1-x}\text{Ga}_x$ alloy (red) and GaAs (black): (a) $x = 0$ ; (b) $x = 0.2$ ; (c) $x = 0.4$ ; (d) $x = 0.6$ ; (e) $x = 0.8$ ; (f) $x = 1$ . . . . .	69

4.5	G of $\text{NiAl}_{1-x}\text{Ga}_x$ alloys with different x compositions on GaAs: measured by TDTR at room temperature (black); calculated by DMM at room temperature (red). . . . .	70
4.6	(a) Comparison of DMM calculated G_spectrum of composition $x = 0$ (black) and $x = 0.3$ (red) at room temperature; (b) Comparison of DMM calculated G_spectrum of composition $x = 0.3$ (red) and $x = 0.6$ (blue) at room temperature; (c) Comparison of DMM calculated G_spectrum of composition $x = 0.6$ (blue) and $x = 1.0$ (violet) at room temperature . . . . .	71
4.7	G(T) measured by TDTR (squares) and calculated by DMM (lines), $x = 0$ (black); $x = 0.25$ (red); $x = 0.75$ (green); $x = 1$ (blue) . . . .	73
4.8	(a) Comparison of DMM calculated G_spectrum of composition $x = 0$ (black) and $x = 0.25$ (red) at 700 K temperature; (b) Comparison of DMM calculated G_spectrum of composition $x = 0.75$ (blue) and $x = 1.0$ (violet) at 700 K . . . . .	74
5.1	(a) XRD of TiN (black), ZrN (red) and HfN (blue) on MgO substrate; (b) XRD of TiN (black), ZrN (red) and HfN (blue) on ScN nitride film/MgO substrate . . . . .	77
5.2	XRR measurements of transducer thickness of epitaxial TiN/MgO, TiN/ScN/MgO, ZrN/MgO, ZrN/ScN/MgO, HfN/MgO, HfN/ScN/MgO. . . . .	79
5.3	Sensitivity plots of group IV metal nitrides on MgO and ScN at room temperature. (a)TiN/MgO sample; (b)ZrN/MgO; (c)HfN/Mgo; (d)TiN/ScN/MgO; (e)ZrN/ScN/MgO; (f)HfN/ScN/MgO . . . . .	80
5.4	Comparison of phonon density of states of the nitride transducer and the beneath dielectric material. Red and black lines are respectively referring to nitride transducer and dielectrics. (a) TiN-MgO; (b) ZrN-MgO; (c) HfN-MgO; (d) TiN-ScN; (e) ZrN-ScN; (f) HfN-ScN. .	82
5.5	Comparison of Experiment and calculated ITC of group IV metal nitrides on MgO. TiN on MgO interface (black); ZrN on MgO interface (red); HfN on MgO interface (blue); remeasured TiN on MgO interface (magenta); TiN/MgO reported by Costescu[3] (cyan). (a) Symbols represents experimental data, line represents DMM calculated results; (b) Symbols represents experimental data, line represents elastic phonon radiation limit. . . . .	84

5.6	Comparison of Experiment and calculated ITC of group IV metal nitrides on ScN. TiN on ScN (black); ZrN on ScN interface (red); HfN on ScN interface (blue). (a) Symbols represents experimental data, line represents DMM calculated results; (b) Symbols represents experimental data, line represents elastic phonon radiation limit. . . . .	86
5.7	Temperature dependent thermal conductivity of ScN; black, red and blue respectively represent thermal conductivity measured under TiN, ZrN and HfN; green represents the electronic portion thermal conductivity calculated from reference[4] . . . . .	88
6.1	Energy separation between $\Gamma$ -, $X$ - and $L$ - conduction band minima in $\text{Al}_x\text{Ga}_{1-x}\text{As}$ with composition of $x$ . Reprinted from Ref. [5] . . . . .	92
6.2	Circuit diagram and measurement schematic for the high temperature/vacuum integrated Seebeck measurement. . . . .	93
6.3	Left: 3D drawing of the Seebeck coefficient stage designed for the vacuum probe station; Right: The actual machined Seebeck coefficient stage assembled in the MMR vacuum chamber. . . . .	94
6.4	A typical Seebeck coefficient measurement data and fitting of the slope for $\text{Al}_{0.52}\text{Ga}_{0.48}\text{As}$ at 350 K . . . . .	95
6.5	(a) The electrical conductivity of $\text{Al}_x\text{Ga}_{1-x}\text{As}$ from room temperature to 300 °C for different alloy compositions; (b) The Seebeck coefficient of $\text{Al}_x\text{Ga}_{1-x}\text{As}$ from room temperature to 300 °C for different alloy compositions . . . . .	96
6.6	The power factor of $\text{Al}_x\text{Ga}_{1-x}\text{As}$ from room temperature to 300 °C for different alloy compositions . . . . .	97
6.7	The bulk concentration of $\text{Al}_x\text{Ga}_{1-x}\text{As}$ from 50 K temperature to 700 K for different alloy compositions measured by hall effect . . . . .	98
6.8	The electron mobility of $\text{Al}_x\text{Ga}_{1-x}\text{As}$ from 50 K temperature to 700 K for different alloy compositions measured by Hall effect . . . . .	99
7.1	X-ray diffraction patterns of (a) $\text{La}_2\text{Ni}_{1-x}\text{Mg}_x\text{O}_4$ and (b) $\text{La}_{1.85}\text{Ni}_{1-x}\text{Mg}_x\text{O}_4$ series powders after calcination. (c)JCPDS card #34-0314 refers to tetragonal $\text{La}_2\text{NiO}_4$ . Peaks marked with an * are indicative of $\text{La}_2\text{O}_3$ phase. . . . .	106

7.2	X-ray diffraction patterns of $\text{La}_{2-y}\text{Sr}_y\text{Ni}_{1-x}\text{Mg}_x\text{O}_4$ series powders after calcination, with (a) $y=0.2$ and (b) $y=0.5$ . (c) JCPDS card #87-0223 refers to $(\text{La}_{1.75}\text{Sr}_{0.25})(\text{NiO}_{2.212})$ . (d) JCPDS card #34-0314 refers to tetragonal $\text{La}_2\text{NiO}_4$ . Peaks marked with an asterisk are indicative of $\text{La}_2\text{O}_3$ phase; peaks marked with a circle are indicative of an orthorhombic $\text{La}_2\text{NiO}_4$ phase. . . . .	108
7.3	X-ray diffraction patterns of $\text{La}_{2-y}\text{Sr}_y\text{Al}_y\text{Ni}_{1-x}\text{Mg}_{x-y}\text{O}_4$ series powders after calcination, with (a) $y=0.2$ ; (b) $y=0.3$ ; (c) $y=0.4$ . (d) JCPDS card #87-0223 refers to $(\text{La}_{1.75}\text{Sr}_{0.25})(\text{NiO}_{2.212})$ . (e) JCPDS card #34-0314 refers to $\text{La}_2\text{NiO}_4$ . Peaks marked with * are indicative of $\text{La}_2\text{O}_3$ phase; peaks marked with a triangle are indicative of $\text{LaAlO}_3$ . . . . .	109
7.4	Quasi-ternary $\text{K}_2\text{NiF}_4$ phase diagram indicating the largest amount Ni that can be replaced while maintaining the $\text{K}_2\text{NiF}_4$ crystal structure. . . . .	110
7.5	(a) X-ray diffraction patterns of $\text{La}_{1.6+x}\text{Sr}_{0.4-x}\text{Al}_{0.4}\text{Mg}_{0.6}\text{O}_{4+x/2}$ series powders after calcinations; (b) JCPDS card #87-0223 refers to $(\text{La}_{1.75}\text{Sr}_{0.25})(\text{NiO}_{2.212})$ . (c) JCPDS card #34-0314 refers to $\text{La}_2\text{NiO}_4$ . Peaks marked with a square are indicative of $\text{La}_4\text{Al}_2\text{MgO}_{10}$ phase; peaks marked with a cross are indicative of an unidentified impurity phase. . . . .	111
7.6	(a) Arrhenius plots of the total electrical conductivities of $\text{La}_{1.6}\text{Sr}_{0.4}\text{Al}_{0.4}\text{Ni}_{1-x}\text{Mg}_{x-0.4}\text{O}_4$ samples, showing values for compositions with $x = 0.8, 0.9$ , and 1. Measurements made in differing oxygen partial pressures are indicated by color, though these values overlap strongly for the $x = 0.8$ and 0.9 compositions. The activation energies of the conductivity-temperature product are listed next to each sample (as detailed in the text, the activation energy increased with decreasing oxygen partial pressure for the $x = 1$ sample). (b) Total electrical conductivity of $\text{La}_{1.6}\text{Sr}_{0.4}\text{Al}_{0.4}\text{Mg}_{0.6}\text{O}_4$ vs. oxygen partial pressure at the three temperatures indicated. In both (a) and (b), error bars are smaller than the data points. . . . .	112
7.7	Arrhenius plot of total electrical conductivity of stoichiometric and nonstoichiometric samples measured in air. Error bars are smaller than the data points. . . . .	115

7.8	Comparison of defect mobilities from literature with the maximum possible mobility (as discussed in the text) in the materials measured here. Maximum defect mobility in $\blacksquare$ $\text{La}_{1.65}\text{Sr}_{0.35}\text{Al}_{0.4}\text{Mg}_{0.6}\text{O}_{4.025}$ and $\bullet$ $\text{La}_{1.5}\text{Sr}_{0.5}\text{Al}_{0.4}\text{Mg}_{0.6}\text{O}_{3.9}$ ; mobility calculated from reported diffusivity of $\square$ $\text{La}_2\text{NiO}_{4+\delta}$ [6], $\circ$ $\text{La}_{1.9}\text{Sr}_{0.1}\text{NiO}_{4+\delta}$ [7], $\blacktriangle$ $\text{La}_{1.8}\text{Sr}_{0.2}\text{NiO}_{4+\delta}$ [7], $\blacktriangledown$ $\text{La}_{1.9}\text{Sr}_{0.1}\text{NiO}_{4+\delta}$ [7] and $\blacklozenge$ $\text{La}_{1.8}\text{Sr}_{0.2}\text{NiO}_{4+\delta}$ [8]. Error bars are smaller than the data points. . . . .	116
7.9	XRD of Ga, Zn, and Ca substituted samples. Peaks marked by * indicate secondary phase of $\text{La}_2\text{O}_3$ . . . . .	117
7.10	Representative SEM micrographs of the polished and thermally etched surfaces of sintered pellets with composition (a) $\text{La}_{1.6}\text{Ca}_{0.4}\text{Al}_{0.4}\text{Mg}_{0.6}\text{O}_4$ , (b) $\text{La}_{1.6}\text{Ga}_{0.4}\text{Al}_{0.4}\text{Mg}_{0.6}\text{O}_4$ , and (c) $\text{La}_{1.6}\text{Sr}_{0.4}\text{Al}_{0.4}\text{Zn}_{0.6}\text{O}_4$ . . . . .	118
7.11	(a) XRD of $\text{La}_{1.6+x}\text{Sr}_{0.4-x}\text{Ga}_{0.4}\text{Mg}_{0.6}\text{O}_{4+x/2}$ ; (b) XRD of $\text{La}_{1.6+x}\text{Sr}_{0.4-x}\text{Ga}_{0.4}\text{Mg}_{0.6}\text{O}_{4+x/2}$ ; (c) XRD of $\text{La}_{1.6+x}\text{Ca}_{0.4-x}\text{Al}_{0.4}\text{Mg}_{0.6}\text{O}_{4+x/2}$ . Peaks marked by: * indicate $\text{La}_2\text{O}_3$ , $\blacktriangle$ indicate $\text{La}_4\text{Ga}_2\text{O}_9$ , $\bullet$ indicate $\text{LaSr}_2\text{GaO}_5$ , $\blacksquare$ indicate $\text{LaAlO}_3$ , and $\blacklozenge$ indicate $\text{CaO}$ . . . . .	120
7.12	Arrhenius plot of total electrical conductivity measured in air for A. $\text{La}_{1.6}\text{Sr}_{0.4}\text{Al}_{0.4}\text{Mg}_{0.6}\text{O}_4$ ; and the Ca substituted samples B. $\text{La}_{1.65}\text{Ca}_{0.35}\text{Al}_{0.4}\text{Mg}_{0.6}\text{O}_{4.025}$ ; C. $\text{La}_{1.6}\text{Ca}_{0.4}\text{Al}_{0.4}\text{Mg}_{0.6}\text{O}_4$ ; D. $\text{La}_{1.5}\text{Ca}_{0.5}\text{Al}_{0.4}\text{Mg}_{0.6}\text{O}_{3.95}$ ; E. $\text{La}_{1.4}\text{Ca}_{0.6}\text{Al}_{0.4}\text{Mg}_{0.6}\text{O}_{3.9}$ . The inset figure displays the conductivity at 650 °C vs. the oxygen stoichiometry. . . . .	121
7.13	Total electrical conductivity at 550 °C of $\text{La}_{1.6+x}\text{Ca}_{0.4-x}\text{Al}_{0.4}\text{Mg}_{0.6}\text{O}_{4+x/2}$ vs. oxygen partial pressure for compositions with $x = -0.2, -0.1, 0, \text{ and } +0.05$ . The near-zero slopes of the best fit lines are indicated next to each line. . . . .	121
7.14	Arrhenius plot of the total electrical conductivity measured in air for A. $\text{La}_{1.6}\text{Sr}_{0.4}\text{Al}_{0.4}\text{Mg}_{0.6}\text{O}_4$ ; and the B-site substituted samples B. $\text{La}_{1.6}\text{Sr}_{0.4}\text{Al}_{0.4}\text{Zn}_{0.6}\text{O}_4$ ; C. $\text{La}_{1.5}\text{Sr}_{0.5}\text{Al}_{0.4}\text{Zn}_{0.6}\text{O}_{3.95}$ ; D. $\text{La}_{1.4}\text{Sr}_{0.6}\text{Al}_{0.4}\text{Zn}_{0.6}\text{O}_{3.9}$ ; E. $\text{La}_{1.65}\text{Sr}_{0.35}\text{Al}_{0.4}\text{Zn}_{0.6}\text{O}_{4.025}$ ; F. $\text{La}_{1.6}\text{Ga}_{0.4}\text{Al}_{0.4}\text{Mg}_{0.6}\text{O}_4$ ; G. $\text{La}_{1.5}\text{Sr}_{0.5}\text{Ga}_{0.4}\text{Mg}_{0.6}\text{O}_{3.95}$ . In all cases, square symbols indicate compositions with stoichiometric oxygen content. . . . .	122

7.15	Total electrical conductivity at 550 °C of La <sub>1.6+x</sub> Sr <sub>0.4-x</sub> Ga <sub>0.4</sub> Mg <sub>0.6</sub> O <sub>4+x/2</sub> vs. oxygen partial pressure for compositions with $x = -0.1$ and 0. The slopes of the best-fit lines are indicated. . . . .	123
7.16	Total electrical conductivity at 550 °C of La <sub>1.6+x</sub> Sr <sub>0.4-x</sub> Ga <sub>0.4</sub> Mg <sub>0.6</sub> O <sub>4+x/2</sub> vs. oxygen partial pressure for compositions with $x = -0.2, -0.1, 0,$ and $+0.05$ . The slopes of the best fit lines are indicated. . . . .	124

## ABSTRACT

Understanding heat transport at nanometer and sub-nanometer lengthscales is critical to solving a wide range of technological challenges related to thermal management and energy conversion. In particular, finite Interfacial Thermal Conductance (ITC) often dominates transport whenever multiple interfaces are closely spaced together or when heat originates from sources that are highly confined by interfaces. Examples of the former include superlattices, thin films, quantum cascade lasers, and high density nanocomposites. Examples of the latter include FinFET transistors, phase-change memory, and the plasmonic transducer of a heat-assisted magnetic recording head. An understanding of the physics of such interfaces is still lacking, in part because experimental investigations to-date have not bothered to carefully control the structure of interfaces studied, and also because the most advanced theories have not been compared to the most robust experimental data.

This thesis aims to resolve this by investigating ITC between a range of clean and structurally well-characterized metal-semiconductor interfaces using the Time-Domain Thermoreflectance (TDTR) experimental technique, and by providing theoretical/computational comparisons to the experimental data where possible. By studying the interfaces between a variety of materials systems, each with unique aspects to their tunability, I have been able to answer a number of outstanding questions regarding the importance of interfacial quality (epitaxial/non-epitaxial interfaces), semiconductor doping, matching of acoustic and optical phonon band structure, and the role of phonon transport mechanisms apart from direct elastic transmission on ITC. In particular, we are able to comment on the suitability of the *diffuse* mismatch model (DMM) to describe the transport across *epitaxial* interfaces.

To accomplish this goal, I studied interfacial thermal transport across  $\text{CoSi}_2$ ,  $\text{TiSi}_2$ ,  $\text{NiSi}$  and  $\text{PtSi}$  -  $\text{Si}(100)$  and  $\text{Si}(111)$ , (silicides-silicon), interfaces with varying levels of disorder (epitaxial and non-epitaxial). The ITC values of silicides-silicon interfaces observed in this study are higher than those of other metallic interfaces to Si found in literature. Most surprisingly, it is experimentally found that ITC values are independent of interfacial quality and substrate orientation. Computationally, it is found that the non-equilibrium atomistic Green's Function technique (NEGF), which is specifically designed to simulate coherent elastic phonon transport across interfaces, significantly underpredicts ITC values for  $\text{CoSi}_2$ -Si interfaces, suggesting that energy transport does not occur purely by coherent transmission of phonons, even for epitaxial interfaces. In contrast, the Diffuse Mismatch Model closely mimics the experimentally observed ITC values for  $\text{CoSi}_2$ -Si,  $\text{NiSi}$ -Si and  $\text{TiSi}_2$ -Si interfaces, and only slightly overestimating the same for  $\text{PtSi}$ -Si interfaces. Furthermore, the results also show that ITC is independent of degenerate doping up to doping levels of  $\approx 1 \times 10^{19} \text{ cm}^{-3}$ , indicating there is no significant direct electronic transport or transport effects which depend on long-range metal-semiconductor band alignment.

Then, I study the effect of phonon band structure on ITC through measurements of epitaxial  $\text{NiAl}_{1-x}\text{Ga}_x$ -GaAs interfaces for varying levels of alloy composition, which independently tunes the mass of the metal's heavy atom without much affect on the lattice structure or interatomic force constants. The ITC values are found to linearly increase with increasing Ga content, consistent with the disappearance of a phonon band gap in  $\text{NiAl}_{1-x}\text{Ga}_x$  films with increasing Ga content, which enhances the phonon transmission coefficients due to a better density of states overlap between the two ( $\text{NiAl}_{1-x}\text{Ga}_x$ , GaAs) materials.

Finally, I study a unique subset of epitaxial rocksalt interfaces between the Group IV metal nitrides ( $\text{TiN}$ ,  $\text{ZrN}$ , and  $\text{HfN}$ ) to  $\text{MgO}$  substrates as well as  $\text{ScN}$  layers. Prior to the current study,  $\text{TiN}$ - $\text{MgO}$  was the only measured interface of this type, and maintained the record for the highest reported ITC for a metal-semiconductor

interface. By varying the Group IV metal, the mass of the metal's light atom was independently tuned, allowing the ability to tune the acoustic phonon frequencies in the metal without significant effect to optical phonon band structure. We find that the ITC of all the studied interfaces are quite high, significantly exceeding the DMM predictions, and in the case of XN-ScN interfaces even exceed the radiative limit for elastic phonon transport. The results imply that mechanisms such as anharmonic phonon transmission, strong cross-interfacial electron phonon coupling, or direct electric transmission are required to explain the transport. The TiN-ScN interface conductance is the highest room temperature metal-dielectric conductance ever reported.

# Chapter 1

## INTRODUCTION

### 1.1 Thermal conduction: a microscopic perspective

Heat transfer, regardless of the macroscopic type (conduction, convection, or radiation) is accomplished by the exchange of energy carriers between locations with different temperatures. In macroscopically large materials it is usually mediated by microscopic collisions of such energy carriers which bring the system toward thermal equilibrium. This process can take place across all phases of matter, like solids, liquids, gases, plasma where movement of nuclei, charge carriers, entire molecules, and sometimes more exotic means (e.g. magnons) serve as the energy carriers. Even vacuum can allow exchange via photons (i.e. radiative transport). Only the type of energy carrier differs between mediums. In the presence of random energy carrier scattering and in a sufficiently large medium, the governing constitutive equation for thermal conduction reduce to the familiar Fourier's law:

$$q'' = -k\nabla T \quad (1.1)$$

where  $q''$  is the heat flux ( $\text{W}/\text{m}^2$ ),  $k$  is the thermal conductivity tensor ( $\text{W}/\text{m}\cdot\text{K}$ ) and  $\nabla T$  is the temperature gradient ( $\text{K}/\text{m}$ ). For isotropic materials which occur for both polycrystalline materials and cubic single crystalline materials (i.e. most materials), the thermal conductivity tensor can be regarded as a scalar.

The microscopic origins of thermal conductivity in a crystalline solid can usually be broken in two independent parts,

$$k_{total} = k_{ph} + k_e \quad (1.2)$$

where  $k_{ph}$  and  $k_e$  respectively represent heat carried by phonons and free electronic carriers. For the heat carried by phonons, a simplified version of the kinetic theory defines the thermal conductivity as  $k = \frac{1}{3}Cv_s\Lambda_G$ , where  $C$  is the volumetric heat capacity,  $v_s$  is the speed of sound and  $\Lambda_G$  is the average scattering length of the phonons called the mean free path (MFP). The equation 1.1 of Fourier’s law works fine on a bulk homogenous material in the continuum limit.

It is also observed that heat flow across a solid-solid interface results in a finite temperature difference that occurs nearly abruptly (i.e. over just a few atoms). In the limit of small temperature differences the constitutive equation for interfacial transport is given by

$$q'' = G\Delta T \tag{1.3}$$

where,  $G$  is defined as the interfacial thermal conductance (ITC) with the unit of MW/m<sup>2</sup>-K. The reciprocal of  $G$  is also known as thermal boundary resistance  $R$ , sometimes also referred to as the ‘Kapitza’ resistance. As will be discussed in detail,  $G$  is a property related with the crystal structures and the chemical bonding of the materials at both sides which of the interface. It is important to point out that interfacial thermal resistance is different from the ‘contact resistance’ as often taught in undergraduate engineering courses, as it exists even at atomically conformal interfaces. Typical experimentally observed value of  $G$  values for phonon dominated solid-solid interfaces are in the range of 10-1000 MW/m<sup>2</sup>-K at room temperature with the overwhelming majority of material interfaces being in the middle of that range. Much less has been observed for electron-dominated interfaces, but  $G$  values as high as 4 GW/m<sup>2</sup>-K have been observed in at clean Al/Cu interfaces (i.e. pure metal interfaces)[9]. Currently, the physical mechanisms governing interfacial thermal transport remain poorly understood.

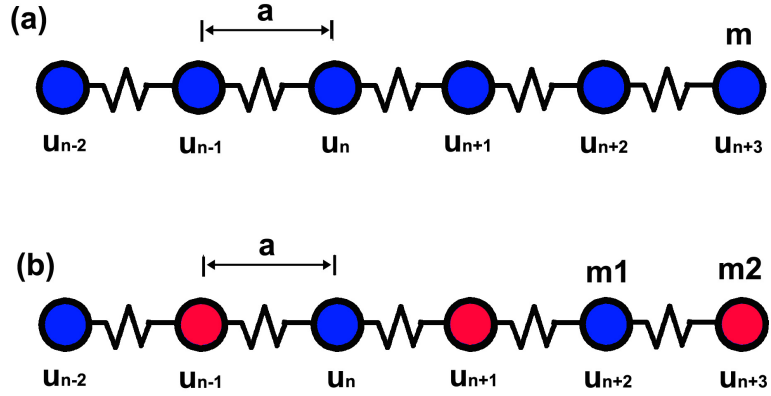


**Figure 1.1:** (a) Schematic of 1-d monoatomic chain connected with springs; (b) Schematic of 1-d diatomic chain connected with springs

## 1.2 Introduction to phonons and phonon transport theory

Understanding the work presented in this dissertation relies on the fact that the reader has basic understanding of thermal transport at nanoscale and phonons in particular. To this extent, I will summarize important concepts essential for the reader to effectively understand this work. Most significantly in this section I will focus on thermal transport at nanometer length scales. More elaborate descriptions of the concepts can be found in books on solid state/condensed matter physics [10, 11].

Primarily, let us focus on the smallest quanta of heat in periodic lattices, i.e. Phonons. In analogy to photons, which are the quantization of electromagnetic waves, phonons are the quantizations of lattice vibrational waves. Though the allowed vibrational states are truly quantum mechanical, much of the physics can be understood in terms of a mass-spring lattice. Consider a hypothetical case of a 1-D lattice chain of atoms as described in 1.1. Where the mass of every atom is given by  $m$  and the attraction between neighbouring atoms is modelled as an elastic spring with a spring constant given by  $C$  (we do not want to use  $k$ , because  $k$  is reserved in quantum mechanics for describing

wavevector). Applying Hooke's law and force balance across n-th atom we have

$$F_n = C(u_{n+1} - u_n) - C(u_n - u_{n-1}) = m \frac{d^2 u_n}{dt^2} \quad (1.4)$$

where  $u_n$  is the displacement of the n-th atom from its equilibrium position,  $u_n = x_n - x_n^0$ . The periodic nature of problem suggests that we seek periodic solutions i.e. sinusoidal functions given by  $u_n = U_0 \exp(kx_n - \omega t)i$ , where  $k$  is spacial frequency (wave-vector) and  $\omega$  is the temporal frequency. Substituting  $u_n$  in eqn 1.4 and solving for  $\omega$  we have,

$$\omega = \sqrt{\frac{4C}{m}} \left| \sin \frac{ka}{2} \right| \quad (1.5)$$

where  $a$  is the interatomic distance. Equation 1.5 which describes  $\omega(k)$  is called the phonon dispersion relationship. At this point it is important to discuss several properties of '1-D phonon dispersion' which qualitatively hold for more complicated systems in higher dimensions; firstly  $\omega(k) = \omega(k + 2\pi/a)$  which allow for translational symmetry operations using reciprocal lattice vectors where a reciprocal lattice vector is given by  $k = 2\pi/a$ , and the domain in the region  $-\pi/a < k \leq \pi/a$  is defined as the First-Brillouin Zone. Conversely we can calculate  $\omega(k \in \mathbb{R})$  by knowing  $\omega$  in the first Brillouin Zone(F-BZ). Secondly, let us define group velocity as  $V_g = \frac{\partial \omega}{\partial k}$ . It can be shown that group velocity is the rate that energy is carried within a wavepacket[10]. We see that a phonon has zero group velocity at the edges of BZ's  $k = (2n + 1)\pi/a$  where  $n$  is an integer. Hence phonons at the edge of BZ carry energy at a zero rate, and thus do not contribute to thermal transport.

We can use a similar method to consider the more advanced case of a one dimensional atomic chain with two non-equivalent atoms with different atomic masses  $m_1$  and  $m_2$  ( $m_2 > m_1$ ) as shown in Figure 1.1(b). Using a similar procedure as above

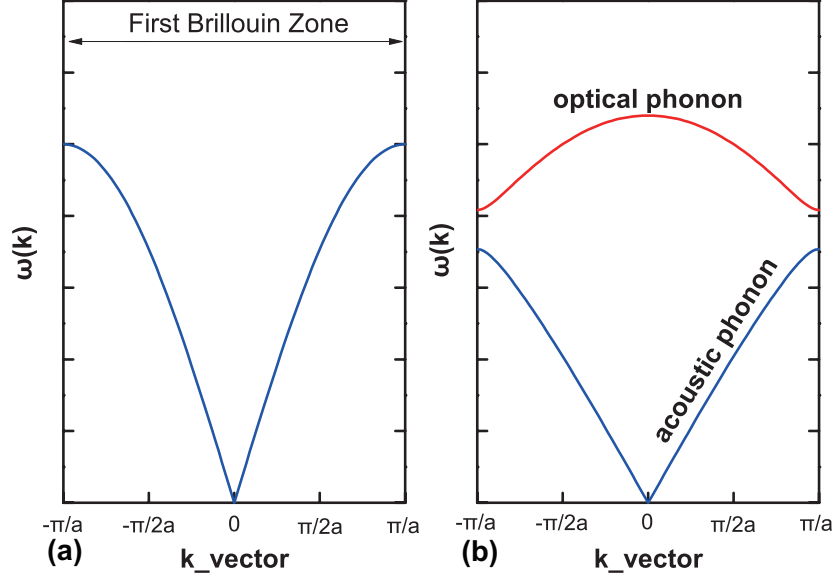


**Figure 1.2:** (a) Plot of phonon dispersion  $\omega(k)$  with  $k$  vector for 1-d monatomic chain; (b) Plot of phonon dispersion  $\omega(k)$  with  $k$  vector for 1-d diatomic chain

the governing equation can be written as,

$$\begin{cases} m_1 \frac{d^2 u_n}{dt^2} = C(u_{n+1} - u_n) - C(u_n - u_{n-1}) \\ m_2 \frac{d^2 u_{n+1}}{dt^2} = C(u_{n+2} - u_{n+1}) - C(u_{n+1} - u_n) \end{cases} \quad (1.6)$$

Assuming a periodic solution (spatial and temporal) the equation 1.6 can be solve to obtain dispersion relation given by,

$$\omega^2 = C \left( \frac{1}{m_1} + \frac{1}{m_2} \right) \pm C \sqrt{\left( \frac{1}{m_1} + \frac{1}{m_2} \right)^2 - \frac{4 \sin^2(ka/2)}{m_1 m_2}} \quad (1.7)$$

Depending on sign in this formula there are two different solutions corresponding to two different branches of the dispersion curve, as shown in Figure 1.2(b). The lower branch is called the acoustic branch, while the upper branch is the optical branch. From the solution, we can find that, there is a discontinuity in the  $\omega$  dispersion, sometimes called a phonon band gap. When  $k = 0$ ,  $\omega_{ac} = 0$ , and  $\omega_{op} = 2C \sqrt{1/m_1 + 1/m_2}$ . At the Brillouin zone edge ( $k=\pi/a$ ),  $\omega_{ac} = \sqrt{2C/m_2}$ , and  $\omega_{op} = \sqrt{2C/m_1}$ . If  $m_1 = m_2$ , optical

phonon and acoustic phonon will meet at the Brillouin zone edge, there will be no phonon band gap. Phonon band gap exists due to large difference of the atomic masses. Acoustic phonon frequency is more dependent on the heavy atom, while the optical phonon frequencies are more dependent on the light atom. While these characteristics are demonstrated in a hypothetical 1-D chain the results are qualitatively similar for 3-D periodic structures.

However one qualitative difference does arise; since a three dimensional atom has two more degrees of translational freedom, there are three phonon vibration modes for each atom in the unit cell. The detailed structure of the phonon dispersion for a 3D lattice is much more complicated than for 1d chain, but many of the basic features are similar, and the concepts discussed here will be helpful for understanding this work. In this thesis, 3D phonon dispersions will be obtained using density functional theory and that information will be used to model thermal transport. The details of that process will be given in Chapter 2.

### **1.3 The importance of interfacial thermal conductance**

As micro/nano technology continues to develop, the size of electronic features continues to decrease, with lateral feature dimensions often less than tens of nanometers for modern devices (an Intel silicon FinFET is now just 14nm wide). This ongoing trend of miniaturization has had a significant impact on the thermal transport properties of modern devices as well. In many cases, the thermal resistance across an interface is even larger than the thermal resistance of the bulk materials. For example a single interface with  $G=100 \text{ MW/m}^2\text{-K}$  (a typical value for a non-epitaxial interface with silicon), has roughly the same resistance as 1,000 nm of Si. This means that in these small-scaled devices, the interfacial thermal resistances are often expected to dominate the thermal transport.

ITC is thus important in many applications. In thermoelectric applications, the device efficiency is related to the material figure-of-merit  $ZT = \sigma S^2 T / k_{tot}$ , where  $\sigma$  and  $S$  are the electrical conductivity and Seebeck coefficient of the material. To achieve

higher  $ZT$ , materials with high electrical conductivity and low thermal conductivity are desired. Venkatasubramanian et al.[12, 13] deposited alternating epitaxial layers of 10 Å thick  $\text{BiTe}_2$  and 50 Å thick  $\text{Sb}_2\text{Te}_3$  by metal-organic chemical vapor deposition (MOCVD). Because the crystal structures of  $\text{BiTe}_2$  and  $\text{Sb}_2\text{Te}_3$  are matched with each other, charge carriers retain a high mobility and move between layers relatively unimpeded and the value of  $S$  remained the same as for the bulk material. However, phonons are strongly scattered by the interfaces leading to a smaller  $k_{ph}$ . This is an example of making use of interfacial thermal resistance by nano-engineering in thermoelectric applications. For next generation magnetic storage technology, heat-assisted magnetic recording hard drives are expected to increase the storage capacity by 10 times compared to traditional hard drive. This technology requires optical (actually plasmonic) heating of the storage media during the write process followed by rapid cooling so as to freeze the information stably in place. This presents a major challenge to the thermal design. Considering that the storage medium is grown as a many-layer stack and that layers are usually of only tens of nanometers thick, the thermal resistance of these interfaces is expected to dominate thermal transport and required extreme attention. Similar challenges exist in quantum cascade lasers which dissipate more heat than their rated optical power and are typically composed of thousands of semiconductor-semiconductor interfaces packed into a 10  $\mu\text{m}$  thick stack. In general, with the development of micro/nano technology and increasing demands of the optimal heat management in these devices, more effort is required to understand the thermal conductance of the interfaces.

#### 1.4 History of interfacial thermal resistance experiments

Interfacial thermal resistance, also known as Kapitza resistance, was first observed from the measurement of a temperature jump across copper and liquid helium ( $^4\text{He}$ ) interface by Kapitza[14]. In an effort to understand why the apparent thermal conductivity of Helium in capillaries is larger than that of bulk Helium, Kapitza measured the temperature distribution in the neighborhood of heated metal surfaces freely

suspended in Helium. He observed a temperature jump between the solid and the He of the order of 2 mK for each milliwatt/cm<sup>2</sup> of thermal flux crossing the interface. This thermal boundary resistance decreased with increasing temperature approximately as  $T^{-3}$ . From the study of this temperature discontinuity when decorated the surface with emery powder, Kapitza deduced that this temperature discontinuity was from the interface instead of the bulk helium.

In the 1960s and 1970s, the interfacial thermal resistances between copper and liquid <sup>3</sup>He and even to solid helium were also observed [15, 16]. In 1976, Reynolds and Anderson measured the interfacial thermal resistance between copper and solid helium, hydrogen, deuterium and neon. [17, 18] Meanwhile, Kapitza resistance between liquid helium and other metals, like mercury, lead, tin, indium and nickel, were also studied by the researchers [19]. As these measurements involved with liquid/solid helium, these experiments were taken at extremely low temperatures (0.1 K to 2 K).

In 1964, Neepor measured the thermal resistance at indium-single crystal sapphire boundaries between 1.1 K and 2.1 K, which was the first measurement of a solid-solid metal-dielectric interface[20]. In the experiment, single crystal sapphire was chosen because of its high thermal conductivity at low temperature, and indium was selected was due to it has a tendency to wet the dielectric surface. In 1974, Schmidt measured the thermal boundary resistance between sapphire and epoxy from 1 to 3 K, which extended the thermal boundary resistance experiment to two dielectric interfaces[21].

It isn't hard to notice that the thermal boundary resistance experiments were all taken at extremely low temperature (a few K). One of the apparent reasons is the fact that the effect was only *observable* at very low temperature. The scale of the interfacial thermal resistance is large enough at low temperature that a noticeable temperature drop across the interface could be observed with the experimental techniques available at that time.

It wasn't until 1979 that a transient hot strip method based on thin film metal strip was developed to measure the thermal conductivity and thermal diffusivity of

solids and liquids[22, 23]. The basic idea of this method is to use a metal strip as both a heater and temperature sensor so as to get precise information of thermal transport properties of the material surrounding the heat source. This is realized by applying constant current in the metal strip which acts as a constant power heat source. At the same time, the subsequent voltage increase over a short period of time after the start of the experiment was monitored. The origin of this voltage increase is the increase of temperature which causes an increase of resistance in the metal strip. As long as the temperature increase is sufficiently small, the temperature coefficient of resistance can be treated as a constant, and this temperature coefficient can be independently calibrated. The monitored voltage increase can be converted into a measured temperature increase in the metal strip. With proper experiment conditions and modeling of the results, the thermal conductivity and thermal diffusivity of the material surrounded the metal strip can be calculated. Thin film metal is applied for its robust thermal contacts and concentrated heat flux, and large signal. This method became widely used to measure the thermal properties of dielectric liquids and solids.

In 1987, Swartz made a modification of the transient hot strip method and measured the thermal boundary resistance on a wide range temperature, from 1 to 300 K[24]. In the experiment, two hot strips were used instead of one, and the two hot strips were made by photolithography with a space of only  $2\ \mu\text{m}$ . On one of the strips a relatively large current was applied as the heat source, and the voltage was monitored to back out the temperature of the first metal strip. In the other strip, a much smaller current were applied just to monitor the temperature. Because the current was small, self-heating in the second strip could be negligible. The substrate temperature beneath the first strip could be determined by the temperature in the second strip. By studying this steady state heat transport process, the thermal boundary resistance could be easily obtained by its definition 1.3. This wide temperature measurement greatly expanded the range of available experimental data concerning thermal boundary resistance. However, the method only worked for studying boundaries between metals and dielectrics.

A more modern form of the hot strip method is called the 3-omega method. This technique is widely used for measuring thermal properties of thin films. In 3-omega method (Figure 1.3(a)), instead of using a constant current or step function of current, an AC current with angular frequency  $\omega$  is applied in the metal strip. The current with frequency  $\omega$  causes a small voltage signal across the strip at a frequency  $3\omega$ . This characteristic  $3\omega$  frequency signal is picked out by lock-in amplifier, which performs the measurement in the frequency domain with extremely high signal-to-noise ratio ( $> 1000 : 1$  typical). One of the advantages of the 3-omega method is that the size scale of the temperature field can be changed by changing the applied current frequency. By varying the temperature field or heat penetration depth, the thermal resistances contribution from interface, film and substrate could be adjusted in some extent. Heat penetration depth can be calculated as  $\lambda_s = \sqrt{D_s/\omega}$ ,  $D_s$  is thermal diffusivity of the substrate. As we can see, higher frequency leads to lower penetration depth, which means that the relative sensitivity to thermal resistance near the surface is increased. Nonetheless, due to the limit of the highest frequency of the electrical signal could achieve (100 kHz typical). The total thermal resistance was measured by this method is still much higher than the thermal resistance of the interface, which usually makes this method unsuitable to measure the thermal boundary resistance of a single interface, though extrapolation of ITC from superlattice thermal performance is quite routine.

In 1986, Paddock and Eesley [1] reported measuring thermal diffusivity with picosecond transient thermoreflectance. In their experiment (Figure 1.3(b)), the authors applied a modulated pulse laser (wavelength 633 nm) to heat the nickel crystal on the surface, and another pulse laser (wavelength 595 nm), which passed through a delay stage, was aligned to the same spot on the surface of the nickel crystal to collect the change of thermoreflectance signal vs. delay time. The first laser beam was called pump beam and the second laser beam was called probe beam. The delay time was controlled by moving the delay stage to change the travelled distance of the probe beam. Since the thermoreflectance signal is related with the temperature of the metal

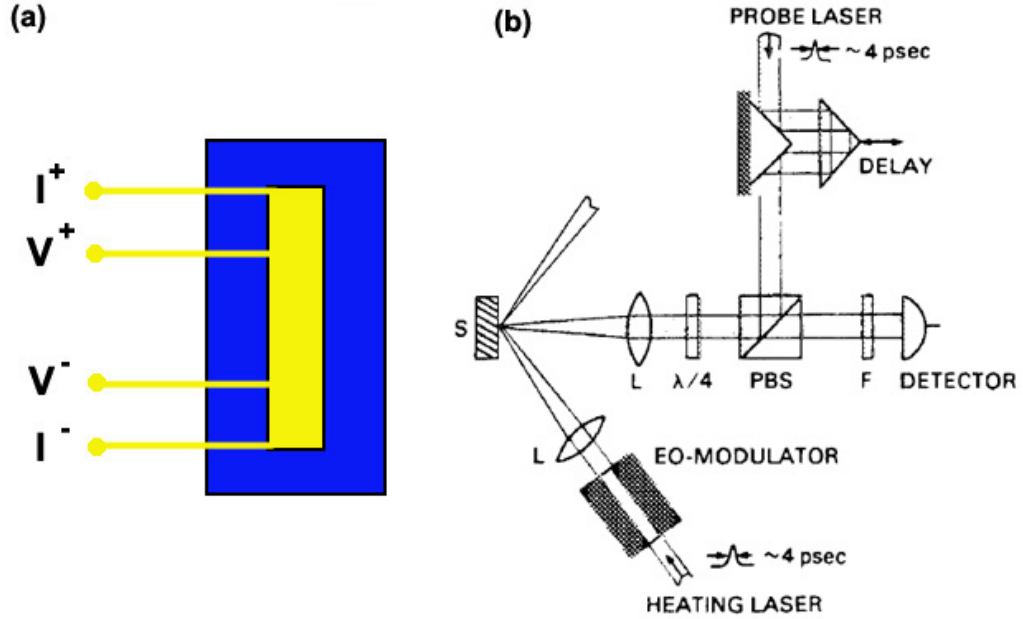


**Figure 1.3:** (a) Top view of 3-omega method sample setup; (b) pump-probe method optical setup, reprinted from reference[1]

surface, the thermal diffusivities of the sample were obtained by fitting the thermoreflectance data vs. delay time. The advantage of this pump-probe method was that it is non-contacting and non-destructive to the sample. Moreover, the determined thermal penetration depth was on order of hundreds of nanometers. This feature makes this technique capable of measuring the thermal boundary resistance. The disadvantage of this method is that, it requires coating a metal film as the transducer on the sample unless the sample surface is formed by a proper metal with moderate thickness. The transducer on the sample surface is used to both absorb light/act as the ‘heat source’ and to reflect the laser, wherein the signal acts as the ‘temperature sensor’. In 1993, Stoner et al.[25] measured thermal resistances of some metal-dielectric interfaces with this method. They reported the thermal interface conductance of single crystal Au grown perpendicular to [2110]  $\text{Al}_2\text{O}_3$ , and found it to be more than 3 times higher than for similar non-epitaxial samples. Compared to theory, epitaxial Au/ $\text{Al}_2\text{O}_3$  interfacial conductance greatly exceeded lattice dynamics calculations and some measurements

were in excess of the phonon radiation limit[25].

In 2003, Costescu et al [3] measured TiN thin films grown on MgO and Al<sub>2</sub>O<sub>3</sub> substrates using time-domain thermoreflectance (TDTR). They compared thermal interface conductance of epitaxial TiN/MgO(001) to TiN/MgO(111) growth and found no difference in their values, in spite of the large number of stacking faults in the latter case. Their data neither fit a coherent lattice dynamics model (which overestimated conductance by  $\approx 70\%$ ), nor a Debye-based diffuse mismatch model (which overestimated by  $\approx 300\%$ ), though if optical modes were excluded from mode-conversion better agreement was found ( $\approx 50\%$ ). The two possible reasons they attributed to the high ITC of TiN/MgO that were insensitive to interface structure were that: either high transmission coefficient because of the perfect interface or full phonon scattering at the hetero-interface (which are quite contradictory conclusions!).

The chemical bonding at the interface is also thought to be important. Wilson[26] has studied the thermal interface conductance of epitaxial SrRuO<sub>3</sub> grown on SrTiO<sub>3</sub> and estimated a lower bound of  $G_{\text{SrRuO}_3/\text{SrTiO}_3} \approx 800 \text{ MW/m}^2\text{-K}$ . The authors ascribe the high ITC of epitaxial SrRuO<sub>3</sub> - SrTiO<sub>3</sub> interface to strong interfacial bonding. Collins et al.[27] has measured the ITC of Al-diamond interfaces while varying the surface termination of diamond. They find that ITC of Al and oxygen-terminated diamonds interface is four times higher than that of Al and hydrogen-terminated diamond. None-the-less, because it is hard to characterize the strength of the interfacial bond or to sort the bond strength out of other factors, like chemicals composition and so on, the exact phonon conversion mechanisms occurring at variably bonded interfaces are unclear. Weakly bonded interface processed by transfer printing thin films have also been studied[28, 29], with the ITC of these weakly bonded interfaces being reportedly lower than  $100 \text{ MW/m}^2\text{-K}$ . Losego et al.[28] varies the end-group functionalities of self-assembled monolayer to tune the bonding between Au and quartz. They have found that the ITC of strong covalent bonded interface is higher than that of weak van der Waals attracted interface. In these transfer printed interfaces, the bonding at the interface are expected to be weak but it could be also contacts at the interface is not

uniform.

For some of the measurements taken on metal-diamond interfaces, phonon transmission across interface with three phonons are expected to be important. Lyeo[30] has studied Pb-diamond and Bi-diamond interfaces. Since the Debye temperatures of Pb and Bi are very low (108 K and 119 K) but Debye temperature of diamond is very high (2200 K), the spectra of lattice vibrations between Pb (or Bi) and diamond are very dissimilar. Therefore, the ITC of Pb-diamond and Bi-diamond are expected to be unusually low, measured with  $8 \leq G \leq 30$  MW/m<sup>2</sup>-K. However, these small values still greatly exceed the two-phonon transmission limit. The authors suggests that the phonon transmission across the interface might involves three or more phonon process while the electron-phonon coupling is not important (though other authors disagree about the latter conclusion). Similarly, Hohensee[31] studied the thermal conductance of metal-diamond interfaces at high pressure in diamond anvil cells. The ITC of metal-diamond interfaces increase weakly or saturate at high pressure. In their work, they also find that ITC of some of metal-diamond interfaces are much higher than the radiation limit. Their calculation reveals multi-phonon transmission process is important.

In the case of interfaces with silicon, Hopkins studied the effects of roughness and chemical bonding on Al/Si interfacial thermal conductance by controlling the oxide layer[32], chemical etching [33], introducing quantum dots [34], and using ion radiation of the native oxide/silicon surface [35]. In their studies, they found that the ITC decreases while the interface roughness is increasing. However, the way they treated the interface could be severely damaging the structure of the interface or leading to contamination of the interface besides changing the interfacial roughness. Thus, the detailed lattice structure of the interface is typically unclear, and the presence of native oxide is virtually assured. A couple reports[36, 37] of thermal interface conductance measurements of polycrystalline Al(111) growth on HF dipped Si(100) substrates exist and show that clean interfaces have substantially higher thermal interface conductance than untreated surfaces. However, epitaxial Al does not readily form on Si, and thus

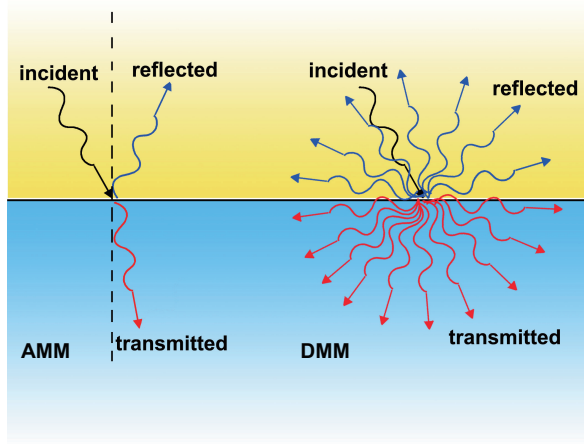


**Figure 1.4:** Schematic of specular and diffuse scattering assumptions in the acoustic and diffuse mismatch models respectively. In the AMM, the reflected and transmitted waves have a definite angle determined from Snells law. In the DMM, phonon is scattered into a state with equal probability to all existing states of the same frequency as the incident phonon in either side of the interface

comparisons between experiment and theories considering interface structure are still lacking.

## 1.5 Theory of interfacial thermal resistance

In 1952, acoustic impedance theory [38], which is now known as acoustic mismatch model (AMM), was first proposed to explain the thermal boundary resistance that occurs between solids and liquid helium. Full details of the model are available in a review by Swartz and Pohl[39]. The general idea for the model is that in a solid the velocity is typically an order of magnitude higher than that in liquid helium; therefore, the phonon momenta in the solid are very different than that in the helium at the same temperature. Since phonon energy and momentum cannot be conserved at arbitrary incident angle, the phonons will be partially reflected when it comes across the interface as determined by the acoustic impedance,  $Z = \rho c$ , where  $\rho$  is the material density and  $c$  is the sound speed (equal to the phonon group velocity at long wavelength).

This impedance of the phonon energy transportation is manifested as a temperature jump across the interface. The resistance estimated by the AMM was higher than the experimental results[14] by more than one order of magnitude. Later, Eisenmenger [40] found that AMM loses its validity to predict the experiemntal ITC results for phonons with frequency larger than 300 GHz (or thermal phonons with  $T > 3K$ ). As soon as more high temperature experimental data become available, the AMM's failure to work became apparent and more advanced models were sought.

In the late 1980s, Swartz and Pohl [24, 39] proposed a diffuse mismatch model (DMM) to explain the phonon scattering behavior across solid-Helium and solid-solid interfaces. This model assumes the opposite extreme: that all the phonons get scattered after reaching the interface in such a way that after scattering, phonons lose memory of their original state and are transmitted into a phonon state with the same energy in either medium. The probability of transmission to either side of the interface for a phonon with a certain frequency depends only on the ratio of density states of phonons with that specific frequency. Therefore, phonon dispersions in either side of materials are needed for applying DMM to calculate interfacial thermal conductance. Initially, the phonon dispersion relationship was approximated by a linear relationship (Debye approximation)[39]. The Debye approximation is limited in that it is accurate for wave vectors close to the zone center but deviates at the zone edge. Reddy[41] has shown that full phonon dispersion relationship over entire Brillouin zone (obtained in his case using Born-von Karman lattice dynamic model) is required in the DMM for accurate determination of the interfacial thermal conductance at high temperature, where zone edge and optical phonons participate in transport. We will carefully describe this full-dispersion DMM in the next chapter as it is used extensively throughout this thesis.

As the calculation capabilities of modern computers developed, atomistic techniques, like molecular dynamics (MD)[42], lattice dynamics (LD)[43] and non-equilibrium atomistic Green's function (NEGF or AGF)[44], have also become common methods to calculate the thermal boundary resistance. An important feature of MD is that anharmonic phonon scattering is included in a very natural manner, which makes MD a very

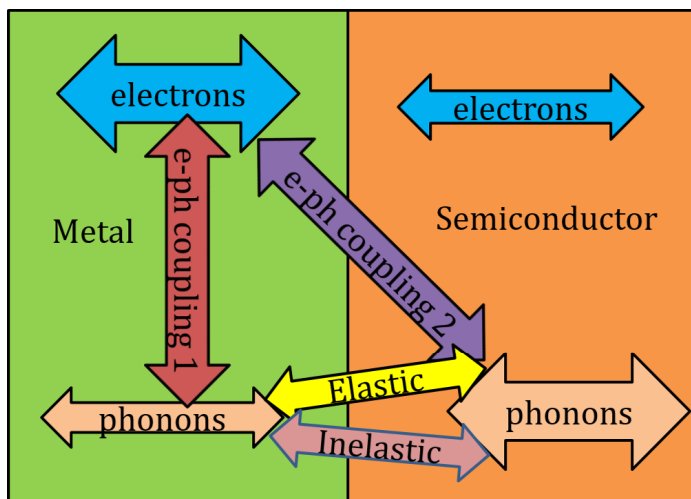


**Figure 1.5:** Schematic of various mechanisms involved in heat transfer between the dominant energy carriers, i.e., electrons in the metal and phonons in the semiconductor. Phonon-phonon energy transfer across the interface could involve elastic and inelastic interfacial scattering processes. Electron-phonon coupling could involve coupling between electrons in the metal with phonons in the metal and with phonons in the semiconductor. Reprinted from reference [2]

useful tool for simulation at high temperature when anharmonic processes are potentially important. Nonetheless, in order to get precise and satisfactory calculation, MD requires large simulation structure which increases computational requirements as well as accurate interatomic potentials. For LD and AGF, because harmonic force constant is usually the only ones involved, these simulations are appropriate at temperatures much lower than Debye temperature. The advantages of these atomistic models are that they could provide spectrally resolved transport information about the interface. However, until very recently neither approach could treat interfaces with non-epitaxial structure.

As indicated in the Figure 1.5, various mechanisms involved in heat transfer between the dominant energy carriers, i.e., electrons in the metal and phonons in the semiconductor. Phonon-phonon energy transfer across the interface could involve elastic and inelastic interfacial scattering processes. Electron-phonon coupling could

involve coupling between electrons in the metal with phonons in the metal and with phonons in the semiconductor.

Though controversial, it has been hypothesized that electron-phonon coupling can influence ITC near metal-dielectric interfaces. Piyush et al.[45] calculated the ITC directly from the Bloch-Boltzmann-Peierls formula. Their calculations indicate that the thermal resistance of electron-phonon coupling 1 process (see Figure 1.5) is not a major contributor to the thermal resistance across metal-dielectric interfaces up to 500 K. The thermal resistance of electron-phonon coupling process is small and the total thermal resistance between metal-dielectrics is from the phonon-phonon transport process. Sridhar[46] calculated the interfacial thermal conductance of  $\text{TiSi}_2$  with C49 structure on Si interface by atomistic Green's function. In their study, they found that the ITC contributed from electron-phonon coupling 2 process is almost the same as that of phonon-phonon transport process. However, since the C49 structure of  $\text{TiSi}_2$  is with low electrical conductivity and less stable phase, it is hard to conduct the thermal interfacial thermal conductance measurement by TDTR. Their calculation has no support of experimental data, which is part of the motivation for this dissertation.

Some of the modelling works also consider the electron-phonon coupling across the interface.

## 1.6 Outline of thesis

The primary objective of this thesis is to provide a set of highly controlled experimental measurements of thermal interface conductance for metal-dielectric interfaces, which can serve as benchmark comparisons for modern computational theory; where possible, we have attempted to make comparison to computational theory ourselves, but we have also engaged a number of collaborators as necessary (namely Anderson Janotti's group at UD, and Tim Fisher's group at Purdue University, both of which are experts in density functional perturbation theory). Comparison to such theory is aimed at developing an understanding of the importance of various potential effects including elastic and inelastic phonon transmission, electron-phonon coupling, structural

disorder, and phonon band engineering. Experimentally, my approach has been to study ‘clean’ metal-dielectric interfaces with controllable structures and compositions (usually this means ‘epitaxial’), and compare the experimental data with modeling results. The influences of epitaxial structure, cross-interface electron-phonon coupling, phonon band structures on the ITC are studied extensively in this thesis and improves the understanding of ITC in the thermal community. Chapters 3, 4, and 5 describe experimental work in three different materials systems, each allowing epitaxial control over the growth, and each allowing different types of tunability that enable a variety of physically phenomena to be examined. Additionally, I have included two chapters (Chapter 6 and 7) with loosely related projects that I have done during my graduate research.

In Chapter 2, I describe the primary experimental and theoretical techniques used for this thesis. First, I introduce the time-domain thermoreflectance(TDTR) setup in our lab, how the TDTR works, and how to interpret the data. Second, I explain how we do the theoretical modeling of interface conductance, and in particular how we perform diffuse mismatch modeling (DMM). Then I describe the tools that I have applied to fabricate and characterize the samples for this thesis.

Chapter 3 presents my experimental study of ITC on epitaxial and non-epitaxial silicide-silicon interfaces. For the first time, we find that the ITCs of epitaxial and clean non-epitaxial interfaces are identical, indicating that transport is insensitive to the details of interfacial structure. Moreover, the ITCs are found to be independent of substrate doping levels, suggesting that electron-electron transport does not contribute to interfacial transport and that electron-phonon coupling, if it exists, is not sensitive to the relative band alignment with the semiconducting phase. Diffuse mismatch modeling gives a surprisingly accurate description of transport in most cases, which is consistent with the observation that ITC is independent of interface structure. However, in the case of  $\text{CoSi}_2$  comparison to a coherent (i.e. non-diffuse) model can also explain the experimental data, but only when anharmonic and near-interface electron-phonon coupling are accurately considered.

In Chapter 4, I experimentally study thermal transport across epitaxial  $\text{NiAl}_{1-x}\text{-Ga}_x\text{-GaAs}$  interfaces in the range  $0 < x < 1$  across a wide temperature range ( $T = 77\text{K} - 700\text{K}$ ), wherein it becomes possible to modify the phonon band structure of the metallic alloy by isovalent substitution of Al for Ga. The DMM model predicts a 100% increase of the ITC of  $\text{NiAl}_{1-x}\text{-Ga}_x\text{-GaAs}$  interfaces for increasing  $x$ , the experiment ITC only shows only a 30% improvement.

Chapter 5, I study the ITC of some group IV transition metal nitrides-MgO and -ScN interfaces. With different group IV metal nitrides (ie. Ti, Zr, and Hf), the acoustic phonon band can be tuned without significant change to the optical phonon frequencies and, for a given substrate, without changing the chemical/ionic nature of the bonding. The results show that ITC is tuned substantially via changes to the acoustic phonon dispersion in the metal. We find that the ITC of all the studied interfaces are quite high, significantly exceeding the DMM predictions, and in the case of XN-ScN interfaces even exceed the radiative limit for elastic phonon transport. The results imply that mechanisms such as anharmonic phonon transmission, strong cross-interfacial electron phonon coupling, or direct electric transmission are required to explain the transport. The TiN-ScN interface conductance is the highest room temperature metal-dielectric conductance ever reported.

Chapter 6 and 7 does not relate directly to interface conductance, but because of my significant contributions in these topics, we include them here as a written record.

Chapter 6 explores the band engineering of a new class of materials for thermoelectric applications:  $\text{Al}_x\text{Ga}_{1-x}\text{As}$ . At a particular alloy composition, these materials have simultaneous band crossings of the  $X-$ ,  $L-$ , and  $\Gamma$ -conduction bands, which is hypothesized to greatly increase the thermoelectric power factor. However, we have experimentally grown and thermoelectrically characterized these materials, and have found that the Si doping efficiency in  $\text{Al}_x\text{Ga}_{1-x}\text{As}$  is very low. This results in relatively low thermoelectric performance in these materials despite their favorable band structure.

Chapter 7 is based on two published manuscripts that I completed in the area

of fuel cell's with Dr. Hertz at the start of my graduate study at the University of Delaware. The project is focused on the search for  $K_2NiF_4$  type electrolyte materials for solid oxide fuel cells. Such materials normally exhibit bipolar charge transport, but by removing Ni from  $K_2NiF_4$  oxides, the large electronic contribution was mitigated. The results indicate that electrolytic conduction is possible in transition-metal-free  $K_2NiF_4$  oxides, but ionic mobility high enough to enable applications was not found.

## Chapter 2

### EXPERIMENTAL AND THEORETICAL METHODS

#### 2.1 Time-domain thermorefectance

Time-domain thermorefectance (TDTR) is an optical pump-probe method used to study the thermal properties of materials. Briefly, a modulated pulse laser (pump beam) is applied to heat the sample on the surface. Then, another pulse laser (probe beam) is applied on the same spot of the sample surface to detect the temperature-dependent reflectivity (i.e. thermorefectance signal). A delay stage is set in the path of the pump or probe beam. Since the speed of light fixed, by moving the position of delay stage and thus lengthening the path length of the one of the beams, the relative arrival time of pump beam and probe beam is adjusted. Finally, fitting the thermal reflectance signal decay curve to an accurate thermal model provides us the thermal diffusivity properties of the sample.

Pump-probe methods for thermal application were first constructed by Paddock and Eesley with two synchronously pump and probe laser in 1986[1]. In 2003, Cahill's group[3] developed a major advance in pump-probe systems using Ti:Sapphire oscillator to produce pump and probe pulses 150 fs long with a central wavelength of 790 nm and a repetition rate of 80 MHz. Cahills system had several novel features, such as CCD camera for investigating the sample surface and aligning beam spots, inductive resonators in series with the photodetector to increase signal and noise ratio, and the mechanical chopper place in the probe beam path to ensure true reflected probe beam signals were picked out. Our TDTR system, which was constructed in our lab located in SPL314 incorporates all the features mentioned above. Its detailed layout will now be explained.

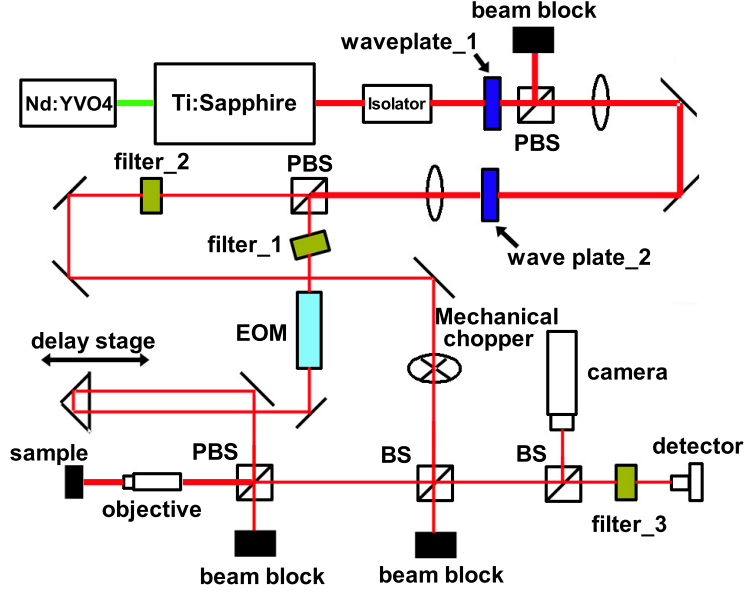


**Figure 2.1:** The optical setup of our time domain thermorefectance system

The optical setup for our TDTR system is shown in Figure 2.1. A frequency-doubled continuous wave Nd:YVO<sub>4</sub> laser (532 nm) is used to pump a Ti:Sapphire crystal to generate a high repetition rate (76 MHz) mode-locked ultrashort pulses (< 200fs) of red or near infrared laser light (650 - 1100 nm). The Ti:Sapphire laser has two outstanding features: the wavelength is tunable and the pulse duration is ultrashort (less than 200 femtoseconds). Ultrashort lasers allow us to probe physical processes over short time and length scales. In our case, the central wavelength of our laser beam is tuned at 785 nm. Right after the laser comes out, the laser beam passes through an isolator, which only allows the beam to travel in the forward direction, and protects the laser source from being destabilized by back reflected laser light. Then the laser beam goes across a  $\lambda/2$  waveplate<sub>1</sub> and polarizing beam splitter (PBS).  $\lambda/2$  waveplates allow tuning of the polarization of the laser. The PBS behind it then splits the polarized beam into its two orthogonal, linearly polarized components. P-polarized light is transmitted and s-polarized light is reflected at 90 degrees. P-polarized light

refers the light with electric field parallel with the incident plane, while s-polarized light represents light with electric field perpendicular with the incident plane. Since the light after the waveplate\_1 is linear polarized, PBS will let the parallel component transmit and perpendicular component reflected and absorbed by the beam block. By adjusting the laser polarization through waveplate\_1, we can tune the total amount power of the laser beam transmitted, or the total power of the laser finally reached on the sample surface. Similarly, by adjusting the light polarization via  $\lambda/2$  waveplate\_2, we can tune pump beam power and the probe beam power ratio, since the s-polarized light and p-polarized light respectively split as pump beam and probe beam at the second PBS. The pump beam (s-polarized light) then goes through filter\_1, an electro-optic modulator (EOM), delay stage, PBS, a microscope objective and then arrive on the sample. Because the pump beam is s-polarized light, most of the pump beam reflected from the sample surface is reflected when it crosses the PBS, but a fraction ( $\sim 1:200$ ) of pump beam is still transmitted. The transmitted part of pump beam would be absorbed by the filter\_3. The probe beam (p-polarized light) goes through filter\_2, mechanical chopper, BS (beam splitter, which lets half of laser beam transmitted and the other half reflected), PBS, a microscope objective and then arrives on the sample surface. The probe beam reflected from the sample surface will transmit through PBS, BS, filter\_3 and arrives on the detector. During experiment, the delay stage moves from left to right (see Figure 2.1), which causes the travelling length of the pump beam becomes shorter and shorter, makes the arrival time of pump beam earlier and earlier. Because the probe beam path keeps the same, the length moving of the delay stage will causes the relative arrival time change during the experiment. By recording the position of the delay stage, the Labview program can calculate and provide the relatively arrival time between pump beam and probe beam.

Since the change of thermorefectance with temperature is small (on orders of  $10^{-4}$  /K or less for a typical transducer), filtering of noise and amplification of signal are important to achieve high sinal-to-noise ratio. Several techniques in the optical path are applied in order to increase the signal to noise (S/N) ratio. First, the most

straight forward way to improve S/N ratio is using the lock-in amplifier. Lock-in amplifiers are used to extract signal at a known carrier frequency from an extremely noisy environment. The operation of a lock-in amplifier relies ultranarrow bandwidth electronic filtering, made possible by frequency mixing of the signal with a reference signal of equal frequency, followed by a long time-constant low-pass filter. The details working principles could be found in the user manual of our lock-in amplifier (Stanford Research Systems Lock-in amplifier model SR844).

In our TDTR system, a square wave with specific frequency controlled by a synthesized function generator (Stanford Research Systems, Model DS345) is sent to electro-optical modulator (EOM) to modulate the pump beam intensity at typical frequency of 12.6 MHz (this can be varied by the user if desired, but the best combination of low electronic/laser noise and small thermal diffusion length is typically here). At the same time, this generated wave was also sent to lock-in amplifier as a reference. An EOM is an optical device whose refractive index changes with the electrical field applied to it; by using it to rotate the polarization of light and then passing it through a polarizing beam splitting the EOM can modulate the laser’s output amplitude. Through the EOM, we can thus modulate the pump beams intensity at a frequency of our choosing. Figure 2.2 shows the pump beam with repetition pulse frequency of 76 MHz before and after modulation with a square wave of 12.6 MHz. Each of the modulated pump laser pulse will serve as a heating source on the surface of the sample and generate a temperature response on the sample. For the probe beam pulses, they arrive on the sample with a time difference  $\tau$  after the pump beam. As shown in Figure 2.2, although the probe beam is not directly modulated by EOM, the thermorefectance signal detected by the probe beam becomes modulated at the reference frequency which is then extracted by lock-in amplifier. This technique rejects laser intensity noise for all frequencies outside  $f_{mod} \pm 1/\tau_{filter}$ .

In order to prevent leaked modulated pump light from reaching the probe intensity detector, which would falsely be detected as ‘signal’, two methods are applied. The first way is using optical filters to prevent reflected pump laser reaching on the

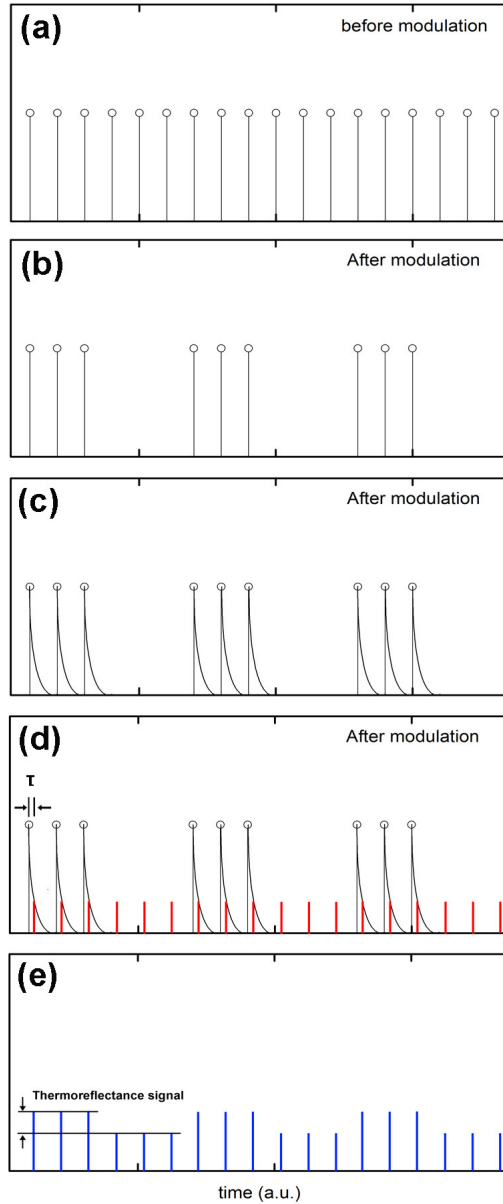


**Figure 2.2:** (a) Mode-locked pump laser with pulses before modulation; (b) Pump laser pulse after electro-optic modulation; (c) Modulated pump laser arrives on the sample surface and generates a heat response on the surface of the sample; (d) Probe pulses arrive on the sample with a time difference of  $\tau$  and pick up reflectance; (e) half of the probe pulses pick up unheated reflectance signal and the other half pick up heated reflectance signal, the difference of the reflectance signal due to heating is the thermoreflectance signal, which has a characteristic frequency of the modulation frequency

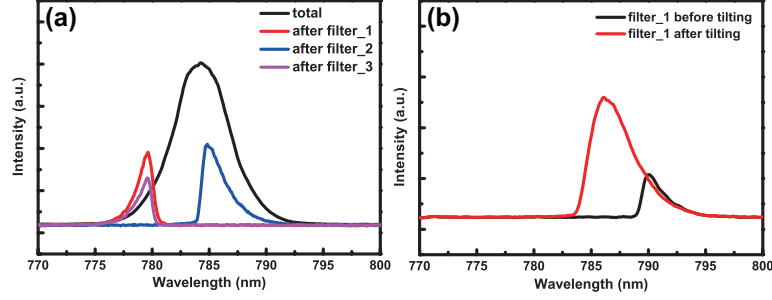


**Figure 2.3:** (a) Total spectrum of the laser before all the filters (black), pump beam spectrum after the tilting filter\_1 (red), probe beam spectrum after filter\_2 (blue), probe beam spectrum after filter\_3 (magenta). Due to the high power density of laser beam and low limit of spectrum detector, the spectrum is collected with scattered lights. Because it is hard to keep the same scattering rate of the lights, the real ratio of intensity between different spectrum is not as shown in this figure. This figure could only represent the wavelength distribution; (b) pump beam spectrum after filter\_1 before tilting (black) and after tilting (red)

photodiode. The other way is using a mechanical chopper with frequency of  $\sim 200$  Hz to ‘double’ modulate the probe beam using a second audio frequency lock-in amplifier.

As shown in Figure 2.1, a long wave-pass filter is placed in the path of pump beam. Two short-wave pass filters with cutoff wavelength of 780 nm are respectively placed in the path of probe beam (filter\_2) and right before photo diode (filter\_3). This is a modification of the original two-tint pump-probe method described by Kang[47]. The filter\_1 is tilted with a small angle to tune the edge wavelength and thus tune maximum available pump beam power before any pump beam could transmitted through filter\_3. Figure 2.3(b) shows the pump beam spectral after filter\_1 with no-tilting and  $\sim 10^\circ$  tilting. Pump beam power increases from 24 mW to 140 mW after tilting. Figure 2.3(a) represents the beam spectrum before any filters, pump beam spectral after filter\_1, probe beam spectral after filter\_2 and reflected beam after filter\_3. The mechanical chopper placed in the probe beam path is spinning at a rate of  $\sim 200$  Hz. This spinning frequency is sent to a Labview control 24-bit A/D converter which implements a digital audio frequency lock-in amplifier in the software. This probe

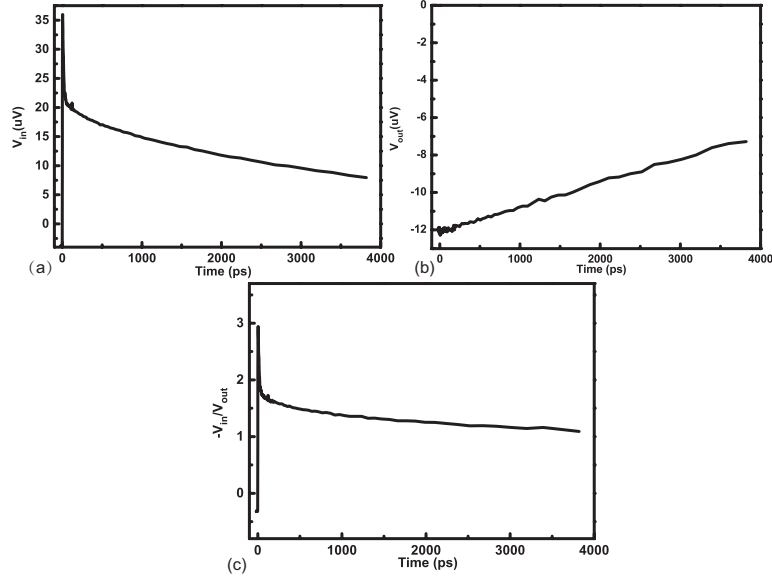


**Figure 2.4:** Typical TDTR data of Al(83nm)/SiO<sub>2</sub>(300nm)/Si wafer taken using 5 times objective with a modulation frequency of 12.6 MHz. (a) In-phase signal vs. time; (b) out-of-phase signal vs. time; (c)  $-V_{in}/V_{out}$  signal vs. time

modulation frequency is very small compared to the pump beam modulated frequency (200 Hz vs 12,600,000 Hz) and the time scale of pump beam and probe beam delay time ( $1-4000 \times 10^{-12}$  s). Therefore, this slow probe modulation does not change the thermal analysis and only helps to pick out the authentic probe beam signal from any leak pump light.

Figure 2.4 shows a typical TDTR data of sample Al(83 nm)/SiO<sub>2</sub>(300 nm)/Si wafer taken with a modulation frequency of 12.6 MHz. The mathematics of the TDTR data reduction model is based on Cahill's original analysis[48], which we've implemented in a set of MATLAB scripts. Briefly, the model is based on superposition of frequency-domain (both time and in-plane spatial) analytic solutions of the n-layer transient diffusion equation, superposed according to the Nyquist-Shannon sampling theorem. According to the paper, the in-phase signal ( $V_{in}$ , real part) and out-of-phase signal ( $V_{out}$ , imaginary part) picked out by lock in amplifier are written in terms of the frequency components of the frequency-domain thermal response evaluated at  $f$  and

$-f$ ,

$$\begin{cases} \text{Re}[\Delta R_M(t)] = \frac{dR}{dT} \sum_{m=-M}^M (\Delta T(m/\tau + f) + \Delta T(m/\tau - f)) \exp(i2\pi mt/\tau) \\ \text{Im}[\Delta R_M(t)] = -i \frac{dR}{dT} \sum_{m=-M}^M (\Delta T(m/\tau + f) - \Delta T(m/\tau - f)) \exp(i2\pi mt/\tau) \end{cases} \quad (2.1)$$

$dR/dT$  is the change of the thermorefectance due to temperature,  $\tau$  is the repetition rate of the laser pulses,  $f$  is pump beam modulation frequency,  $t$  is the delay time between pump beam and probe beam, and  $\Delta T$  is the frequency domain solution to the surface temperature heated by periodic point source[48]. The upper and lower limit of the sum are in principle  $M \rightarrow \infty$  but Cahill has shown that the summation can be truncated according to the shortest timescale of experimental interest and convergence can be accelerated through use of a mathematical roll-off filter. Usually, the thermal properties of the sample are analyzed by fitting long time range (100 ps - 4 ns),  $V_{in}/V_{out}$  data, where we have the most sensitivity to thermal properties. By taking the ratio of in-phase and out-of-phase signal,  $dR/dT$  is removed from the equation. Therefore, we do not need to measure the actual  $dR/dT$  of the metal to analyze the data. Normalizing the two signals by one another also has the very advantageous effect of removing noise due to laser intensity fluctuations.

The thermal fitting model requires that every geometric and thermal property of every layer be provided as inputs to simulation except the ones being fit. While this might appear to be a large number of inputs (a 3-layer/2-interface model has 11 input parameters, for example), the thermal model is typically not sensitive to all the inputs; in addition, the thermal model cannot necessarily distinguish between different thermal parameters; for example, the model is often sensitive to substrate effusivity ( $kC$ ) such that one can never independently determine  $k$  and  $C$  through a multivariate fit. To aid in determining which parameters the model is sensitive to, we formally define the Sensitivity of our experiment to an input parameter as the derivative of the

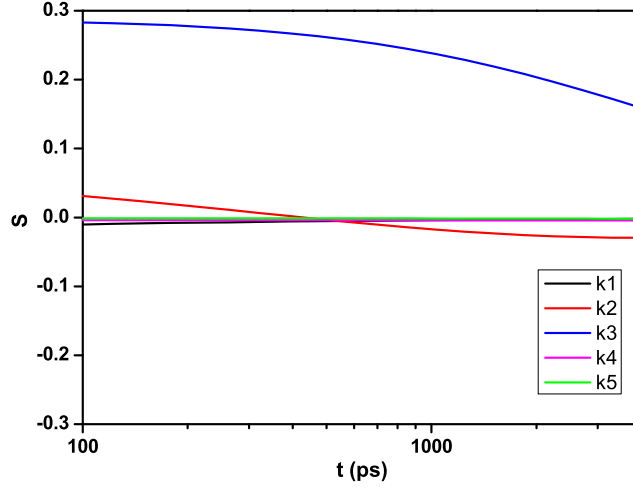


**Figure 2.5:** Sensitivity plot of sample Al(83 nm)/SiO<sub>2</sub>(300 nm)/Si wafer with 12.6 MHz modulation frequency and 2 times objective

logarithm of the experimental signal,  $\text{Signal} = [-V_{in}(t)/V_{out}(t)]$ , with respect to the logarithm of the parameter itself,  $\alpha_n$  such that

$$S_{\alpha_n} = \frac{\partial \ln(\text{Signal})}{\partial \ln(\alpha_n)} \quad (2.2)$$

Conveniently this can be interpreted as

$$S_{\alpha_n} = \frac{\delta(\text{Signal})/(\text{Signal})}{\delta\alpha_n/\alpha_n} \quad (2.3)$$

For  $n_{th}$  layer, if  $S_{k_n}$  is large at time  $t$ , it means that a fractional change in its thermal conductivity,  $f$ , leads a fractional change in the TDTR signal of  $S_{k_n} \times f$ . Figure 2.5 shows the sensitivity plot of sample Al(83 nm)/SiO<sub>2</sub>(300 nm)/Si wafer with 12.6 MHz modulation frequency and 2 times objective. The thermal conductance from top to bottom considered in our model are thermal conductivity of Al ( $k1$ ), thermal conductance of Al and SiO<sub>2</sub> interface ( $k2$ ), thermal conductivity of SiO<sub>2</sub>, thermal conductance of SiO<sub>2</sub> and Si interface ( $k4$ ) and thermal conductivity of Si wafer ( $k5$ ). As indicated in

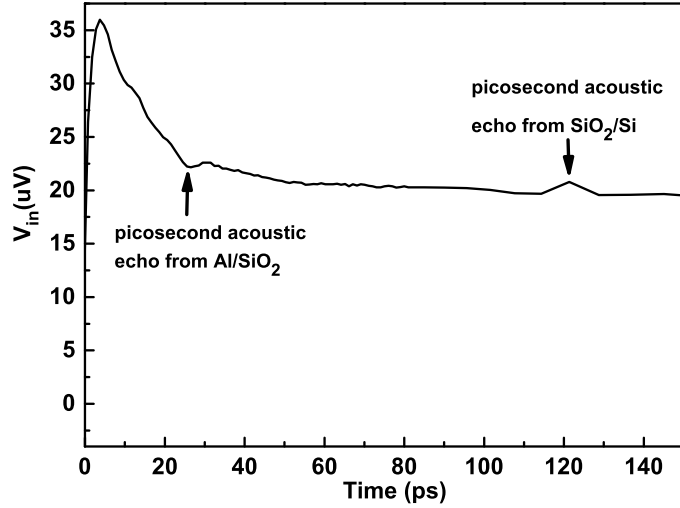


**Figure 2.6:** In-phase TDTR data of Al(83 nm)/SiO<sub>2</sub>(300 nm)/Si wafer from 0 ps to 150 ps

the figure, the TDTR measurement for this sample stack is most sensitive to thermal conductivity of SiO<sub>2</sub>  $k_3$ , and the sensitivity decreases with time delay, and also have some (though very little) sensitivity to Al/SiO<sub>2</sub> interface. Due to the high thermal conductivity of Al and the thermal penetration depth is smaller than the thickness of SiO<sub>2</sub>, the measurement has negligible sensitivity to  $k_1$ ,  $k_4$  and  $k_5$ . Our TDTR fitting software automatically calculates the sensitivity to every input parameter and plots it for the user to interpret before each fit.

Figure 2.6 shows the short time range (0 ps to 150 ps) TDTR in-phase data of Al(83 nm)/SiO<sub>2</sub>(300 nm)/Si. Because the light absorption in the metal does not actually happen at the surface, and because the transient and spatially nonlocal absorption process is challenging to model, very short time TDTR data (0-30 ps) is not ideal for thermal properties fitting within our usual framework[48]. Nonetheless, there is useful information in the form of picosecond acoustic echoes in short time scale data, caused by strain waves formed nearly instantaneously by the laser absorption process.

As we can see in the figure, there is a ‘dent’ in the data at around 26 ps in Figure 2.6. This ‘dent’ originates from a reflectance change of the surface due to acoustic waves reflected at Al/SiO<sub>2</sub> interface of the transducer. When the surface of layered sample is heated by the pump laser, a strain pulse will be generated in the transducer. This strain pulse travels into the film until reflected back from any interfaces. Then this strain field returns to the surface and is detected by the probe beam as a reflectance change. These acoustic echoes sometimes show as a ‘peak’ instead of ‘dent’ depending on relative acoustic impedance of materials at the reflecting interface. For example, the peak at about 121 ps is the picosecond acoustic echo corresponding to reflection from the SiO<sub>2</sub>/Si interface. The return time and the shapes of the acoustic echoes depend on the thickness/acoustic velocity of the layer and impedance mismatch between the materials forming the interface. Therefore, the acoustic echoes are useful for measuring the thickness of the transducer or the elastic constant information. For example, the acoustic velocity in Al is 6420 m/s, the acoustic wave traveled distance is  $2 \times h$  (from Al surface and reflects at the Al-SiO<sub>2</sub> back to the surface,  $h$  is the thickness of Al film), the thickness of Al film is estimated by  $h = 6420m/s * 26e - 12s/2 = 83e - 9m$ .

## 2.2 Data modeling by full phonon dispersion DMM

### 2.2.1 Full phonon dispersion calculation

It is well-known that high frequency phonons dominate thermal interface conductance [41] in all but the highest Debye temperature materials (e.g. diamond), and thus accurate consideration of the full phonon dispersion is required including that of optical phonons. Throughout this thesis, phonon dispersions are calculated ab-initio using Quantum ESPRESSO[49] density functional theory software, an open source package available online which we have compiled with MPI parallizations for use on UD’s Farber community cluster. In Chapter 3, we enlisted the help of collaborators (Janotti (UD) and Fisher (Purdue)) for the more difficult calculation found there, but in the other chapters (4 and 5), we have performed the calculations ourselves. Unless

otherwise specified, density functional theory was first applied to self-consistently obtain the the ground state electron density and total energy. Next, dynamical matrices are calculated on a uniform mesh across the irreducible points in the first Brillouin zone of the primitive lattice. Then the real-space Interatomic Force Constants (IFCs) are obtained by Fast Fourier Transform of the reciprocal space dynamical matrices. Lastly, the IFCs are used as input to determine the phonon frequencies (i.e. dispersion) for any desired modes[50]. Phonon dispersions generated in this way were used for interfacial transport modeling as well as determining the volumetric heat capacity required for interpretation of experiments, typically on a  $50 \times 50 \times 50$  q-grid. For the primitive unit cells with a two-atom basis found throughout this thesis (e.g. Si, GaAs, NiGa, NiAl, TiN, ZrN, HfN, ScN, MgO), this corresponds to about 1.3 million considered modes.

### 2.2.2 Phonon thermal interface conductance modeling

As it is defined in equation 1.3, the thermal boundary conductance  $G$  is the ratio of heat current density ( $q_{A \rightarrow B}$ ) and the temperature difference ( $\Delta T$ ). The heat current density can be expressed as integral of the energy carried by phonon across the interface for each the phonon mode  $i$  at the  $k$  wavevector over the whole Brillouin zone[41],

$$q_{A \rightarrow B} = \frac{1}{2(2\pi)^3} \sum_i \int_{k_z=-k_{max}}^{k_{max}} \int_{k_y=-k_{max}}^{k_{max}} \int_{k_x=-k_{max}}^{k_{max}} \alpha_{A \rightarrow B}(k, i) \cdot \hbar\omega(k, i) |V(k, i) \cdot n| f(\omega(k, i), T) dk_x dk_y dk_z \quad (2.4)$$

where  $\hbar$  is planck constant,  $\hbar\omega$  is phonon energy,  $n$  is unit vector normal the interface. For each  $k$  and  $i$ ,  $\alpha_{A \rightarrow B}(k, i)$  represents the probability of transmission from A to B,  $\omega(k, i)$  is phonon angular frequency,  $V(k, i)$  is the phonon group velocity,  $f(\omega(k, i), T)$  is Bose-Einstein distribution for phonons ( $\omega(k, i)$ ) at temperature  $T$ . Bose-Einstein distribution is written as  $f(\omega(k, i), T) = \frac{1}{\exp(\frac{\hbar\omega(k, i)}{k_B T}) - 1}$ . Taken derivative of equation 2.4

with respect to T, G is expressed as,

$$G = \frac{1}{2(2\pi)^3} \sum_i \int_{k_z=-k_{max}}^{k_{max}} \int_{k_y=-k_{max}}^{k_{max}} \int_{k_x=-k_{max}}^{k_{max}} \frac{1}{k_B T^2} \alpha_{A \rightarrow B}(k, i) \cdot (\hbar\omega(k, i))^2 |V(k, i) \cdot n| \frac{\exp(\frac{\hbar\omega(k, i)}{k_B T})}{\exp(\frac{\hbar\omega(k, i)}{k_B T}) - 1} dk_x dk_y dk_z \quad (2.5)$$

Note that, with the exception of transmission coefficient,  $\alpha(k, i)$ , the integral is completely defined by the phonon dispersion  $\omega(k, i)$  since  $V(k, i) \equiv \nabla_k(\omega)$ . The phonon dispersion can be easily obtained by DFT in most cases. Obtaining an accurate model of phonon transmission is the most challenging and controversial part of understanding interfacial thermal conductance.

### 2.2.3 Diffuse mismatch modeling of transmission coefficient

One method of modeling phonon transmission coefficient that we apply throughout this thesis is called the diffuse mismatch model. The DMMs basic physical assumption are that (1) all incident phonons are scattered at the interface, (2) all interactions are elastic and (2) modes lose memory of their original state. This implies that the transmission probabilities are the same for phonons with the same frequency[39]. The transmission probability for phonon with specific frequency,  $\omega$ , is dependent on the available phonon density of states with frequency  $\omega$  in either medium and the group velocity normal to interface of each phonon. Reddy has shown that under these assumptions, the transmission coefficient for an arbitrary pair of phonon dispersions can be written as[41]

$$\alpha_{A \rightarrow B}(\omega') = \frac{\Delta K_B [\sum_{j, k'} |V(k', j) \cdot n|] \delta_{\omega(k', j), \omega'}}{\Delta K_A [\sum_{i, k} |V(k, i) \cdot n|] \delta_{\omega(k, i), \omega'} + \Delta K_B [\sum_{j, k'} |V(k', j) \cdot n|] \delta_{\omega(k', j), \omega'}} \quad (2.6)$$

where  $j$  and  $k'$  are the phonon mode and wave vector in medium B.  $\delta_{\omega(k, i), \omega'}$  is Kronecker delta function which is unity when  $\omega(k, i) = \omega'$  and zero otherwise. Plugging equation 2.6 into equation 2.5, all the variables in the final expression are known from the full phonon dispersion. The integration of  $G$  is numerically performed by summing over all the modes over the first Brillouin zone.

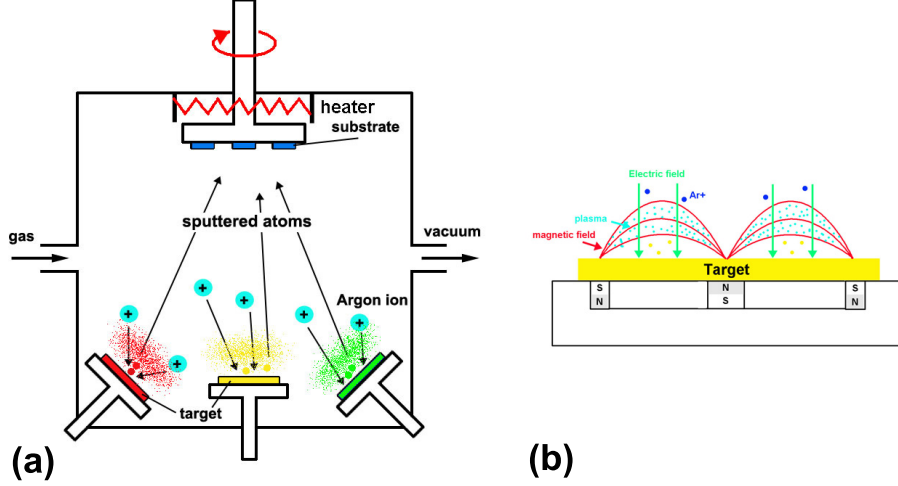


**Figure 2.7:** (a) The configuration of magnetron sputtering; (b) The magnetic field and electrical field near the sputtering source

### 2.2.4 The radiative limit for interfacial heat transport

It is occasionally useful to compare measured ITC to the maximum possible value consistent with detailed balance. Simply put, the principle of detailed balance states that when the two sides of an interface are in thermal equilibrium (i.e.  $\Delta T = 0$ ) the net heat flux must be zero. This places constraints on the maximum possible heat flux (and maximum spectral transmission coefficient), since the interface conductance must be the same regardless of which side is considered the ‘incident’ material in Eq. 2.5 and yet transmission coefficients cannot exceed unity for any mode (and is often, in fact lower). Detailed balance implies that the upper limit of interface conductance corresponds to setting

$$\alpha = \begin{cases} 1, & D(A) \leq D(B) \\ \frac{D(B)}{D(A)}, & D(A) > D(B) \end{cases} \quad (2.7)$$

where  $D(A) = \Delta K_A [\sum_{i,k} |V(k,i) \cdot n|] \delta_{\omega(k,i),\omega'}$  and  $D(B) = \Delta K_B [\sum_{j,k'} |V(k',j) \cdot n|]$ .

### 2.3 Magnetron sputtering

Unless otherwise noted, the thin films in this dissertation are deposited in a multi-target, custom-built reactive magnetron sputtering machine (PVD products, Wilmington, MA). The Figure 2.7(a) shows the schematic diagram of the magnetron sputtering system. Magnetron sputtering is a physical vapor deposition (PVD) process in which plasma is created near the surface of the target materials and positively charged ions (usually an inert gas ion like  $\text{Ar}^+$ ) from the plasma are accelerated by an electrical field superimposed on the negatively charged target material. The accelerated  $\text{Ar}^+$  ions strike on the target material with high kinetic energy and eject atoms from the target. These ejected ions from the target will condense on the surface of the substrates and form quality films. The schematic of electric field and magnetic field near the surface of the target is shown in Figure 2.7(b). The magnetic field applied on near target is used to trap the movement of low speed ions to form high density plasma near the surface target in order to improve the deposition rate. For deposition of ferromagnetic materials like Ni and Co, in order to get reasonable magnetic field on the ferromagnetic target surface, the magnets behind the target are replaced with stronger magnets and a target with reduced thickness is used for deposition. For example, the thickness of our Ni target is 0.0625 inch, 1/4 of the thickness of non-magnetic target.

In order to deposit compounds or alloys, at least three techniques are used within this thesis. Often it is possible to use targets whose stoichiometry matches the desired film stoichiometry. In Chapter 4 for example, NiAl and NiGa are deposited from stoichiometric targets purchased commercially. One can also use co-deposition, whereby two targets are simultaneously sputtered at rates calibrated to give the correct stoichiometry. While it is more difficult to achieve perfect stoichiometry in deposited films, with consistent chamber performance and accurate calibration, it can work well. In Chapter 3 for example, we deposit  $\text{CoSi}_2$  by co-sputtering from elemental Co and Si targets and achieve epitaxial growth. In Chapter 4, we also use the co-sputtering approach to obtain epitaxial  $\text{NiAl}_{1-x}\text{Ga}_x$  intermetallic alloy thin films from targets of NiAl and NiGa. Lastly, reactive sputtering can be used to create compounds containing

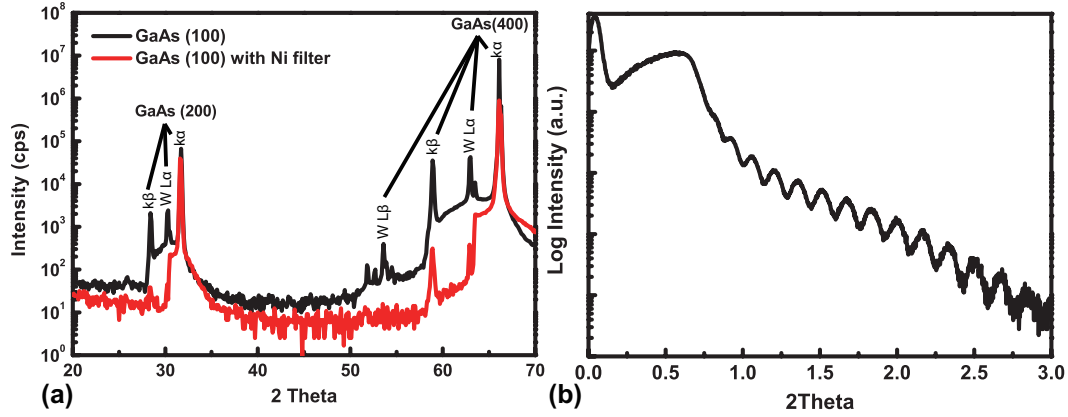


**Figure 2.8:** (a) X-ray diffraction of single crystal GaAs(100) wafer with Ni filter (red) and without Ni filter (black); (b) X-ray reflectivity of 50 nm TiN on MgO single crystal substrate

normally gaseous elements. For example, when a small amount of O or N is added to the base Ar plasma, the O/N will react with most elemental materials to form oxides/nitrides. In Chapter 5, the TiN, ZrN, HfN, and ScN are formed by reactive sputtering of Ti, Zr, Hf, and Sc in the presence of a N/Ar plasma mixture.

## 2.4 X-ray diffraction (XRD) and X-ray reflectivity (XRR)

One of the major advances of this thesis is the study of structure characterized and controlled interfaces. As such, XRD and other characterization techniques play a central role. XRD and XRR were performed to determine the crystal structure and thickness of the films on Rigaku Ultima IV X-ray diffractometer with Cu  $K\alpha$  radiation located in University of Delaware's Advanced Materials Characterization Lab. The growth orientations of the films were investigated by  $\omega$ - $2\theta$  geometry scanning and when possible the epitaxial thin films were also verified using phi scans to check the in-plane diffraction plane symmetry. Since several wavelengths of X-rays are generated by our X-ray tube but only Cu  $K\alpha$  is preferred, removing contamination spectrum from other wavelength X-rays is important. Figure 2.8(a) shows the XRD results of single crystal GaAs(100) wafer with Ni filter (red) and without Ni filter (black). As the Ni filter is

applied, the contaminated spectrum from tungsten filament  $L\alpha$  (or  $W L\alpha$ ),  $K\beta$  and  $W L\beta$  are greatly suppressed. However, because the diffraction of X-rays from single crystal GaAs(100) wafer is so strong that the these contamination spectrum peaks cannot be totally removed. Throughout the thesis, these contamination peaks in XRD results are marked as ‘\*’ if not specified.

Specular X-ray Reflectivity (XRR) is applied to measured thickness of the films with thickness less than 100 nm with very high accuracy via observation of spacing of interference fringes. In particular, refractive index contrast between layers occurs due to differences in electron density, making interference patterns quite sharp for metal-semiconductor materials. An XRR pattern for a 50 nm TiN film on MgO single crystal substrate is shown in Figure 2.8(b). The films thickness was obtained by fitting the oscillation periods in the XRR data. Moreover, the film material density and roughness information could be also provided by the XRR data. The XRR data were analyzed by Globalfit X-ray Reflectivity Analysis software in the computer with the equipment.

## 2.5 Electronic thermal conductivity measurement

This dissertation studies many metal-semiconductor interfaces. For data reduction, it is typically necessary to have at least an independent estimate of the metal-layer thermal conductivity. The electronic portion thermal conductivity of the metal film is estimated by Wiedemann Franz Law. First, the electrical conductivity is measured using an inline four point probe with regression to an  $I - V$  curve by Keithley 2401. The electrical conductivity and thermal conductivity by electron are related via the Wiedemann Franz Law,

$$\frac{k_e}{\sigma} = LT \quad (2.8)$$

where  $k_e$  is electronic portion thermal conductivity,  $\sigma$  is electrical conductivity.  $L$  is Lorenz number, a universal factor with  $2.44 \times 10^8 \text{ W}\Omega/\text{K}^2$ ,  $T$  is the absolute temperature. In metals, the thermal conductivity from electron is almost equal to the total thermal conductivity, since the high electron-phonon scattering rate suppresses lattice thermal conductivity.

## 2.6 Transmission electron microscopy (TEM)

The interface structures of some epitaxial interfaces were investigated by Transmission Electron Microscopy (FEI Titan 80-300 keV Field Emission Environmental Transmission Electron Microscope, HRTEM). The crystal structure and growth direction were also analyzed by Fast Fourier Transform of the HRTEM images. The cross-section TEM samples were prepared by lift-out technique with a Forced Ion Beam system (FEI Novalab Focused Ion Beam, FIB). The TEM images of the  $\text{CoSi}_2$  in this dissertation were taken by our collaborators at Birck Nanotechnology Center in Purdue University.

## Chapter 3

### THERMAL TRANSPORT ACROSS METAL SILICIDE-SILICON INTERFACES: AN EXPERIMENTAL COMPARISON BETWEEN EPITAXIAL AND NON-EPITAXIAL INTERFACES

#### 3.1 Motivation

Metal silicide thin films are present in nearly all modern silicon microelectronic devices. In particular, the silicides PtSi, WSi<sub>2</sub>, TiSi<sub>2</sub>, CoSi<sub>2</sub>, NiSi are used extensively due to their low electrical contact resistance to Si, low resistivity, and chemical process compatibility, as well as the low thermal budget associated with their formation[51, 52]. They can serve a wide range of roles including ohmic contacts, Schottky barrier contacts, gate electrodes, local interconnects, and diffusion barriers. While many silicides are excellent thermal conductors due to their low electronic resistivity, they are generally applied as thin films with nanoscale thicknesses, such that interfacial properties are expected to dominate thermal transport locally[53, 54, 55]. This work reports the experimental measurements of thermal interface conductance on a wide range of technologically relevant metallic silicide-silicon interfaces, and shows that they are the highest thermal interface conductances ever measured for a metal-silicon interface on silicon, and are comparable to the highest metal-dielectric thermal interface conductances ever measured.

In addition to the practical implications to thermal management in microelectronics, silicide interfaces represent a unique opportunity for studying the fundamental physics of thermal transport across interfaces. In general, a lack of experimental data exists regarding the role of disorder on thermal interface conductance, and in particular data for which the interfacial structure is known is scarce. Despite a large number of investigations of thermal interface conductance in literature, there are just

a few which directly measure the thermal conductance of epitaxial metals on crystalline substrates. Liu [56] recently reported the first thermal conductance measurement of an epitaxial metal with silicon: a NiSi<sub>2</sub>/Si interface within a Si nanowire created by a reactive method using an in-situ electron beam heating technique. The thermal interface conductance reported was unusually high:  $G = 500 \text{ MW/m}^2\text{-K}$  at 300K. Taken together, these measurements show that epitaxial interfaces can produce record-breaking phonon-dominated thermal interface conductances. References [25, 3, 56, 26] also serve as the only metal-dielectric interface thermal conductance measurements performed where the interfaces were simultaneously structurally and thermally characterized. Thus, to date they are the only experiments with which direct theoretical comparisons can be made. Despite this, it would appear that no such comparisons have been made using modern computational tools. Consequently, there are substantial open questions about the physics of transport across epitaxial as well as disordered interfaces.

Silicide-silicon interfaces are a great testing platform for the effect of disorder on thermal interface conductance because many metal silicide interfaces can be grown either as epitaxial or non-epitaxial interfaces depending on the synthetic process and substrate orientation. Also, many silicides are metallic and optically opaque, which enables their direct use in modern optical thermal interface conductance characterization methods such as time-domain thermoreflectance (TDTR). Epitaxial growth of metal silicides on silicon has been previously demonstrated for most known silicides including PtSi[57], CoSi<sub>2</sub>[58, 59], NiSi[60], C54 TiSi<sub>2</sub>[61], C49 TiSi<sub>2</sub>[62], VSi<sub>2</sub>[63], CrSi<sub>2</sub>[64],  $\gamma$ - &  $\beta$ -FeSi<sub>2</sub>[65], YSi<sub>2</sub>[66], YSi<sub>2</sub>[67], GdSi<sub>2</sub>[67], TbSi<sub>2</sub>[67], DySi<sub>2</sub>[67], HoSi<sub>2</sub>[67], ErSi<sub>2</sub>[67], TmSi<sub>2</sub>[67], YbSi<sub>2</sub>[67], LuSi<sub>2</sub>[67], MoSi<sub>2</sub>[68], Pd<sub>2</sub>Si[69], TaSi<sub>2</sub>[70], WSi<sub>2</sub>[71], OsSi<sub>2</sub>[72], and IrSi<sub>2</sub>[73]. For many silicide compounds including PtSi (orthorhombic), NiSi (orthorhombic), and CoSi<sub>2</sub> (fluorite), epitaxy occurs most readily on  $\langle 111 \rangle$  substrates, though for lattice-matched fluorite structure compounds, epitaxy on  $\langle 100 \rangle$  substrates is still possible under some preparation conditions. For example, CoSi<sub>2</sub> and Si are both cubic with similar lattice parameters  $5.3\text{\AA}$  and  $5.43\text{\AA}$  respectively, and CoSi<sub>2</sub> can be

grown epitaxially using high-temperature codeposition onto  $\langle 100 \rangle$  substrates.

In this chapter, we systematically study the thermal interface conductance of epitaxial and non-epitaxial interfaces of the metal-silicide  $\text{TiSi}_2$ ,  $\text{CoSi}_2$ ,  $\text{NiSi}$  and  $\text{PtSi}$  with silicon using time-domain thermoreflectance (TDTR) and compare the results to the most advanced available theories.

## 3.2 Experimental

### 3.2.1 Epitaxial silicide growth

$\text{TiSi}_2$ ,  $\text{CoSi}_2$ ,  $\text{NiSi}$  and  $\text{PtSi}$  were fabricated under a wide range of conditions. We studied films: (i) on both  $\text{Si}(100)$  and  $\text{Si}(111)$  substrates, (ii) using a wide range of Si substrate doping concentrations, (iii) using different surface cleaning methods, and (iv) two different growth techniques. The two different substrates orientations were used in order to generate different interfacial structures, since it is known that the rhombohedral compounds  $\text{PtSi}$ [74, 75, 76, 77] and  $\text{NiSi}$ [78, 79] films grow epitaxially on  $\text{Si}(111)$  surfaces, while these form polycrystalline structures on  $\text{Si}(100)$  surfaces. All the silicides studied here were grown by thermally induced reactions of the pure metal: Ti, Co, Ni, or Pt were deposited by RF-sputtering onto a Si substrate at 300K. Samples were then annealed at high temperature ( $\text{PtSi}$ : 400 °C;  $\text{NiSi}$ : 400 °C;  $\text{TiSi}_2$ : 750 °C;  $\text{CoSi}_2$ : 750 °C for 30 minutes) within the sputtering chamber to induce the reactive growth of the appropriate silicide layer ( $\sim 110\text{nm}$  thick). With the exception of  $\text{TiSi}_2$  (C54 phase), the silicides here form epitaxial interfaces on  $\text{Si}(111)$  when grown by the thermal method. None of the silicides form epitaxial interfaces when grown on  $\text{Si}(100)$  by this method. In the case of  $\text{CoSi}_2$  we also grew samples by co-sputtering of elemental Si and Co at 750 °C, which allowed the formation of epitaxial interfaces on  $\text{Si}(100)$  substrates, unlike the thermal method. We pre-cleaned all Si wafers using acid piranha followed by either (1) an in-situ RF sputtering substrate bias cleaning, followed by a 750 °C substrate anneal or (2) an HF dip performed  $\sim 30$  sec prior to loadlocking the samples into the sputtering chamber. The latter approach produced smoother final surfaces according XRR characterization. Samples with substrate doping levels ranging

from  $n = 1 \times 10^{19} \text{ cm}^{-3}$  to  $p = 1 \times 10^{19} \text{ cm}^{-3}$  were also created to explore electronic effects on the thermal interface conductance of metal-semiconductor junctions.

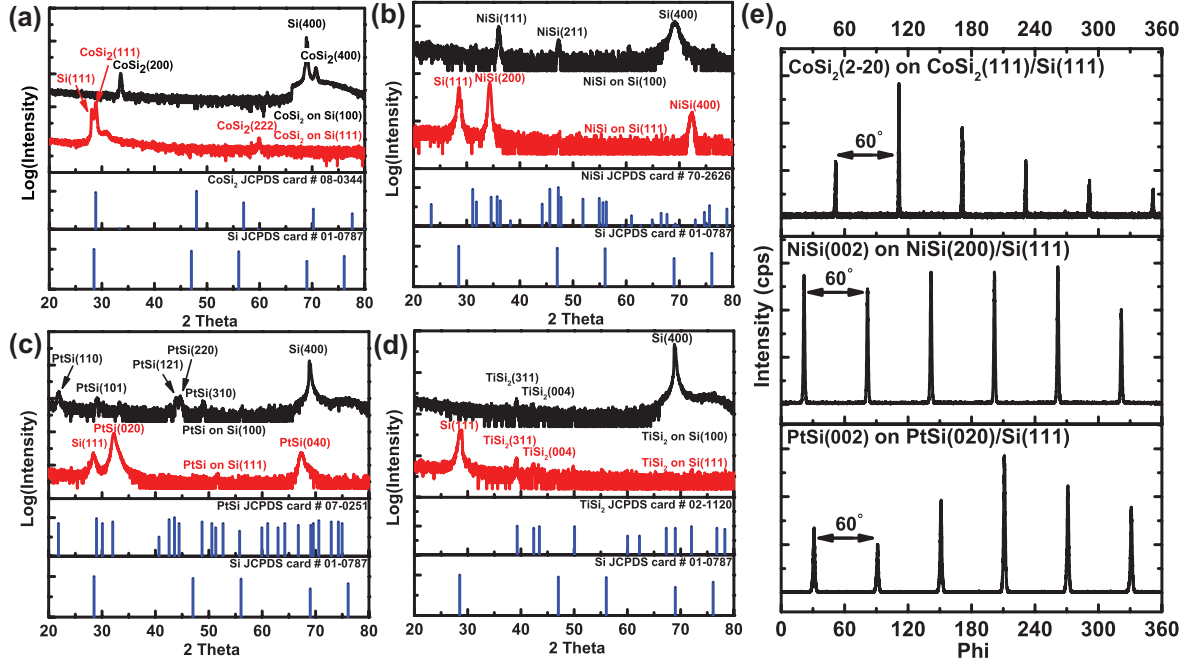


**Figure 3.1:** (a) XRD results of CoSi<sub>2</sub> on intrinsic Si(100) and Si(111) wafer; (b) XRD results of NiSi on intrinsic Si(100) and Si(111) wafer; (c) XRD results of PtSi on intrinsic Si(100) and Si(111) wafer; (d) XRD results of TiSi<sub>2</sub> on intrinsic Si(100) and Si(111) wafer; (e) XRD phi scan of the in-plane diffraction for PtSi(020)/Si(111), NiSi(200)/Si(111) and CoSi<sub>2</sub>(111)/Si(111) samples.

X-ray diffraction (XRD) was used to characterize the structure of the films, and confirmed epitaxial growth in the cases of NiSi, PtSi and CoSi<sub>2</sub> on Si(111) substrates (regardless of which surface preparation was used) and also in the case of co-sputtered CoSi<sub>2</sub> on Si(100). Figure 3.1 shows XRD  $\omega$ - $2\theta$  scans of different silicides grown on intrinsic Si(100) and Si(111) wafers, and the JCPDS index cards of the corresponding materials are given for comparison. No peaks from elemental Ti, Co, Ni or Pt are observed, indicating there is no unreacted metal detected in the films. Scans for co-sputtered CoSi<sub>2</sub> on HF-pretreated Si(111) and Si(100) show peaks at CoSi<sub>2</sub>(111)/(222) and CoSi<sub>2</sub>(200)/(400) respectively (Figure 3.1a). For NiSi on

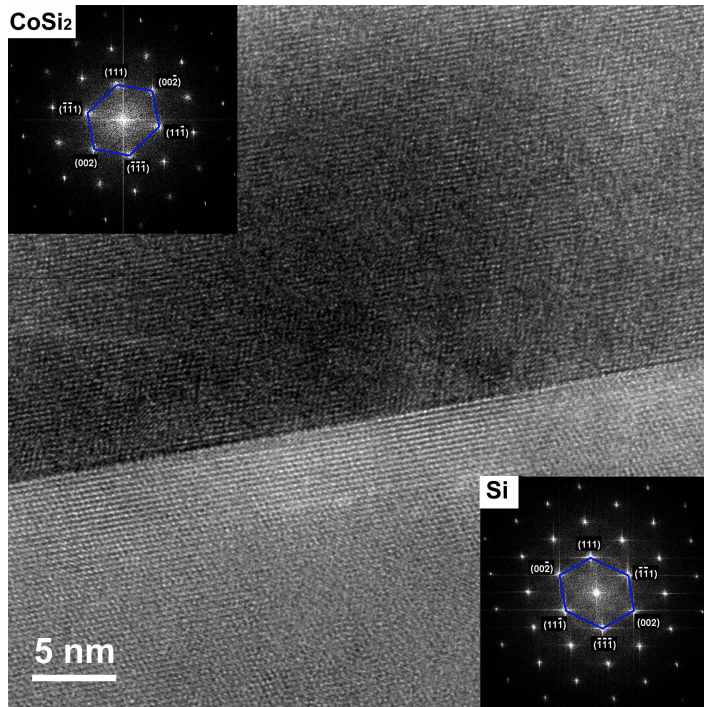


**Figure 3.2:** HRTEM of an epitaxial CoSi<sub>2</sub>(111)-Si(111) interface. FFT of CoSi<sub>2</sub> and Si indicates a 180° with respect to [111]

Si(111) only NiSi(200)/(400) peaks at  $34.4^\circ$  and  $72.5^\circ$  respectively are observed (Figure 3.1b). In contrast, the NiSi on Si(100) shows primary peaks from NiSi(210) and Ni(211) diffraction planes ( $36.1^\circ$  and  $47.5^\circ$ ), indicating oriented polycrystalline growth. The XRD patterns of PtSi/Si(111) and PtSi/Si(100) show similar behavior: PtSi films formed on Si(111) shows only PtSi(020)/PtSi(040) planes and the PtSi film grown on Si(100) exhibits a polycrystalline structure with almost random orientations. For TiSi<sub>2</sub> on Si(111) and Si(100), both substrate orientations yield the same characteristic peaks corresponding to the C54 face-centered orthorhombic phase of TiSi<sub>2</sub> (the strongest of which are TiSi<sub>2</sub>(311) and TiSi<sub>2</sub>(004)), which is the same phase used in many microelectronics applications. We found no preferential growth direction in the case of TiSi<sub>2</sub> on Si(111) or Si(100). The growth of silicides on doped Si wafers was found to be identical to that on the intrinsic wafers.

XRD  $\phi$ -scans of the diffraction planes perpendicular to the sample surface (in-plane diffraction planes) were performed to confirm epitaxy of the silicides. Figure 3.1(e) shows the in-plane XRD  $\phi$  scans of sample PtSi(020)/Si(111), NiSi(200)/Si(111) and CoSi<sub>2</sub>(111)/Si(111). For PtSi(020)/Si(111), the in-plane diffraction peak of PtSi(200) plane, corresponding to  $2\theta=30.06^\circ$ , was taken while rotating the sample  $360^\circ$  with its out-of-plane axis. The pattern shows six-fold symmetry. While the crystal structure of PtSi is orthorhombic, the in-plane XRD  $\phi$  scan shows a six-fold symmetry rather than two fold because there are 3 equivalent PtSi epitaxies conforming to the pseudo-hexagonal structure of the Si(111) surface[75]. The same is expected to occur on orthorhombic NiSi on Si(111)[80]. The XRD  $\phi$  scan of the in-plane diffraction peak of NiSi(020) plane with  $2\theta=54.94^\circ$  on the NiSi(200)/Si(111) sample shows a six-fold symmetry, which confirms a pseudo-hexagonal epitaxial growth of NiSi on Si(111). The XRD  $\phi$  scan of CoSi<sub>2</sub>(111)/Si(111) sample also indicates a six-fold symmetry of the in-plane diffraction peak of CoSi<sub>2</sub>(2-20) plane with  $2\theta=48.15^\circ$ . This result suggests the epitaxial growth of the CoSi<sub>2</sub>(111) on Si(111). The in-plane lattice mismatch between the epitaxial silicide films and Si wafer are calculated to be  $\approx 11\%$  for PtSi(020)/Si(111),

$\approx 5\%$  for NiSi(200)/Si(111) and  $\approx 1\%$  for CoSi<sub>2</sub>(111)/Si(111). Despite the large mismatch in the case of PtSi, the interface is known to form epitaxially by relieving strain using a undulating interface[76].

### 3.2.2 Transport characterization

Thermal interface conductance and substrate thermal conductivity measurements were performed using time-domain thermoreflectance (TDTR). Our system is based on the two-tint approach described by Kang and Cahill[47]. The measurement system and methods of data reduction have been described in detail previously[47, 48]. The time evolution of surface temperature is measured through temperature-dependent changes in the reflectivity, i.e., the thermoreflectance. We analyze the ratio of in-phase  $V_{in}$ , and out-of-phase  $V_{out}$  variations in the intensity of the reflected probe beam at the modulation frequency (12.6 MHz unless otherwise specified) of the pump beam as a function of delay time between pump and probe. The wavelength of the mode-locked Ti:sapphire laser is  $\lambda = 785$  nm and the  $1/e^2$  radius of both focused beams is  $25 \mu\text{m}$  with a repetition rate of 76 MHz.

One unique aspect of this work is that we use the metal silicide itself as the metal transducer. Unless otherwise noted, TDTR data reduction consisted of simultaneous non-linear least square extraction of the substrate thermal conductivity and thermal interface conductance between the silicide and silicon substrate. In order to perform data reduction, it is necessary to know the thickness of the silicide films, the heat capacity of all the layers, and the thermal conductivity of any layers for which data reduction is not being performed. The thickness of the silicides was determined by calibrating the thickness of pure metal deposited under the same conditions, measured by X-ray reflectivity, and using knowledge of the silicide lattice constant and stoichiometry. The characteristic light absorption coefficient  $\alpha = 4\pi k/\lambda$  can be calculated using the imaginary component of the refractive index,  $k$ , which is known if either the complex permittivity or complex refractive index is known,  $\sqrt{\tilde{\epsilon}} = n + ik$ . The optical absorption depth is defined as  $\delta = 1/\alpha$ . For the silicides studied here, the

optical constants are available in literature and the results are given in the following table (Al is also given for reference, though in fact Al experiences hot electron diffusion which makes its effective heat absorption depth several-fold larger than the optical absorption depth). As indicated in table 3.1, the characteristic light absorption length of

**Table 3.1:** Calculated Optical Absorption Depth of Silicides

Material	$n$	$k$	$\delta$ @ $\lambda=785\text{nm}$
Al	2.58	8.40	7.4nm
TiSi <sub>2</sub>	2.89	2.92	21.4nm
NiSi	2.96	2.63	23.8nm
PtSi	3.56	2.37	26.4nm
CoSi <sub>2</sub>	2.39	1.72	36.3nm

the silicides ranged from 21-36nm, which is  $\approx 3$ -fold larger compared to a traditional Al transducer. Therefore the silicide transducer layers were grown to be  $\sim 110\text{nm}$  to ensure full absorption of the laser and to avoid anomalous signals at short time delays due to electron-hole pair modulations of the reflectivity. The absorption process was approximated using the bilayer technique described by Cahill[48], though the particular model used was not found to affect the experimental regression because the fit was performed at long time delays (300ps-3700ps) where details of the initial heat deposition profile no longer matter. Most of the sensitivity to interface conductance occurs at the largest time delays where this is especially unimportant. Room temperature sensitivity plots showing the interface thermal conductance, substrate thermal conductivity, and thermal conductivity of the silicide for all of the interfaces are given in Fig 3.3 as a function of time delay. Here we define sensitivity as the fractional change in the experimental signal (the ratio,  $-V_{in}/V_{out}$ ) per fractional change in the parameter. The most important things to note are that: (1) the magnitude of the interface thermal conductances sensitivity are  $\sim 0.2-0.4$  over most of the measurement range. The signal to noise ratio for TDTR was better than 100:1 (as estimated from the standard deviation of the out-of-phase signal divided by its average value) for each of the 64 data

points used for fitting, so that the primary source of error becomes uncertainty in the values of “known” model parameters (heat capacity of the silicide and its thermal conductivity for example) rather than the accuracy of the raw data. (2) the shape of the sensitivity curves are different for the substrate and interface at different time delays. This allows one to simultaneously extract substrate thermal conductivity and interface thermal conductance. In principle it is possible to measure the thermal conductivity of the transducer using the short-time delay behavior as well (though modeling optical absorption accurately then becomes important), but we instead obtain it independently using electrical resistivity measurements/Weidemann-Franz law.

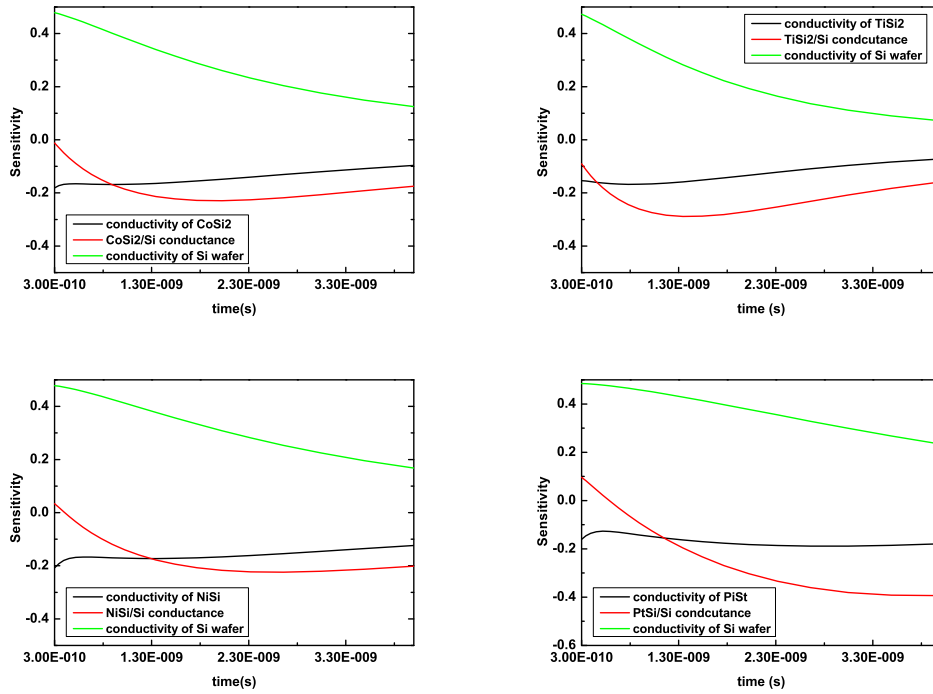


**Figure 3.3:** Room temperature sensitivity plots for  $\text{CoSi}_2$ ,  $\text{TiSi}_2$ ,  $\text{NiSi}$ , and  $\text{PtSi}$  vs time delay

Heat capacities of all the films were determined by density functional perturbation theory (DFPT) through our own DFPT calculations. Results from the heat capacity calculations for  $\text{CoSi}_2$ ,  $\text{TiSi}_2$ ,  $\text{NiSi}$  and  $\text{PtSi}$  can be found in the Supporting

**Table 3.2:** Silicide properties at 300K

Silicide	$\rho$ ( $\mu\Omega$ -cm)	$\kappa_e$ (W/m-K)	$C_V$ ( $10^6$ J/m <sup>3</sup> -K)
CoSi <sub>2</sub>	16	44 (calc)	2.74
TiSi <sub>2</sub>	19	38 (calc)	2.52
NiSi	20	36 (calc)	2.99
PtSi	40	18 (calc)	2.49

Information[81]. The sheet resistance/electrical conductivity of the silicide films were measured at room temperature using an inline four point probe with regression to an I-V curve. The resulting electrical resistivities were used to estimate the electronic component to thermal conductivity using the Wiedemann-Franz law, assuming the degenerate Lorenz number  $L_0=2.44 \times 10^{-8}$  W $\Omega$ /K<sup>2</sup>. The results are given in Table 3.2. The thermal conductivity of silicides was high enough to yield good sensitivity to thermal interface conductance, and the electronic thermal conductivity was verified to be a good approximation of the total thermal conductivity with TDTR using observations at time-scales below 400 ps, where sensitivity of the signal to the metal transducers thermal conductivity is strongest and most independent.

The temperature dependent electrical resistivity of CoSi<sub>2</sub>, TiSi<sub>2</sub> and NiSi used in this work were estimated by using the literature-reported temperature coefficient of resistance combined with our measured room temperature electrical resistivity values. The temperature dependent electrical resistivity, we used our measured room temperature resistivity combined with the literatures reported temperature coefficient of resistivity of CoSi<sub>2</sub>[82], TiSi<sub>2</sub>[83] and NiSi[84]. The electrical resistivities (units in are respectively calculated by ( $\rho$  units:  $\mu\Omega$ -cm,  $T$  units: K):

$$\rho_{CoSi_2}(T) = 0.0503 * (T - 293) + 16 \quad (3.1)$$

$$\rho_{TiSi_2}(T) = 0.062 * (T - 293) + 19 \quad (3.2)$$

$$\rho_{NiSi}(T) = 0.038 * (T - 293) + 20 \quad (3.3)$$

Note that errorbars associated with the extracted thermal interface conductance are found to be much less sensitive to the transducer thermal conductivity than the extracted substrate thermal conductivity. For example, for CoSi<sub>2</sub> at 300K a 10% uncertainty in silicide thermal conductivity corresponds to an errorbar of 4.6% in the extracted interface conductance and 13.6% in substrate thermal conductivity. For the case of PtSi, there are no previously reported temperature coefficients of resistance. The PtSi/Si temperature dependent TDTR data were therefore analyzed by including PtSi silicide thermal conductivity as a third fitting parameter. At room temperature, the thermal interface conductance value of PtSi/Si obtained this way was within 5% of that obtained in Fig. 3.5 using the measured thermal conductivity.

In the cases of PtSi, NiSi, CoSi<sub>2</sub>, TiSi<sub>2</sub> (C54), we found that the temperature dependence of reflectivity at 300K is comparable to the best previously reported materials[85] at  $\lambda=785$  nm. The thermoreflectance coefficients of CoSi<sub>2</sub> films had a positive value, while TiSi<sub>2</sub>, NiSi and PtSi exhibited negative values. In the case of CoSi<sub>2</sub>, the thermoreflectance coefficient was found to switch signs near 600K, allowing substrate thermoreflectance effects to become experimentally visible and thus complicating the data analysis. For this reason we restrict our experimental results for CoSi<sub>2</sub> to room temperature and below. This effect was not observed in PtSi, NiSi and TiSi<sub>2</sub>, which allowed measurements from 77K-700K for these materials.

### 3.3 Modeling

Two forms of phonon transport modeling have been used, here: (1) interface thermal conductance calculations from full-phonon-dispersion diffuse mismatch modeling[41], using phonon dispersions obtained from DFPT, and (2) atomistic Green's function simulations employing density functional theory (DFT) to calculate interatomic force constants, including the effect of bonding changes near the interface. First-principles calculations for phonon dispersion were performed in the case of CoSi<sub>2</sub> and

Si under the density functional theory (DFT) framework using Quantum Espresso[49], with a planewave basis set. The exchange correlation energy was approximated under the generalized gradient approximation (GGA) using the Perdew-Burke-Ernzerhof (PBE) functional form. Rappe-Rabe-Kaxiras-Joannopoulos (RRKJ) ultrasoft pseudopotentials were used for both Si and Co atoms. The relaxed bulk lattice constant of Si and CoSi<sub>2</sub> were found to be 5.46 Å and 5.36 Å which compares well with the experimental lattice constants of 5.43 Å (Si) and 5.36 Å (CoSi<sub>2</sub>). While the density functional perturbation theory (DFPT) calculations on bulk Si and bulk CoSi<sub>2</sub> provide the bulk inter-atomic force constants (IFCs), the AGF method also requires as input the interfacial force constants at the Si-CoSi<sub>2</sub> interface. We perform DFT/DFPT calculations on a Si(111)-CoSi<sub>2</sub>(111) interface supercell shown in Figure 3.4. This interface supercell corresponds to the 8B interfacial atomic configuration that has been identified to have the lowest interfacial energy in prior first-principles calculations of the Si-CoSi<sub>2</sub> interface,[86] and was also experimentally observed using TEM (Fig. 3.2). A tensile strain of 1.8% is imposed on CoSi<sub>2</sub> to match its lattice with Si. All the atomic positions and the lattice constant along the c-direction (heat transport direction) are relaxed for the interface supercell while the in-plane lattice constants of the interface supercell are fixed to that of bulk Si. Because the AGF simulations are performed on an interface between Si and strained CoSi<sub>2</sub>, the bulk phonon dispersion and IFCs of strained CoSi<sub>2</sub> are also determined using a separate DFT/DFPT calculation. The unit cell in DFT calculations of bulk strained CoSi<sub>2</sub> corresponds to a 9 atom unit cell as shown the dashed box in Figure 3.4. We also use a 6 atom unit cell for calculations on bulk Si with one of the lattice vectors aligned along the [111] direction (see Figure 3.4). Table 3.3 shows the k-point grids and the cutoff energies used in DFT calculations of the bulk and interface structures. The phonon dynamical matrices are computed using DFPT on a Monkhorst-Pack q-point grid, and the phonon dispersion at arbitrary q-points are obtained using Fourier interpolation.

The bulk phonon dispersions of Si and CoSi<sub>2</sub> are used to obtain predictions for the thermal interface conductance using the diffuse mismatch model, and an upper

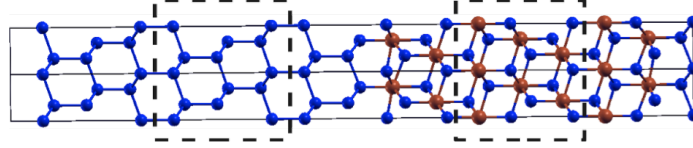


**Figure 3.4:** Schematic of the Si-CoSi<sub>2</sub> interface supercell with a 8B interfacial atomic configuration. The dashed rectangular boxes indicate the unit cells of bulk Si and bulk strained CoSi<sub>2</sub>.

**Table 3.3:** DFPT Details for CoSi<sub>2</sub> / Si interface modeling

Parameter	Bulk Si	Bulk unstrained CoSi <sub>2</sub>	Bulk strained CoSi <sub>2</sub>	Si-CoSi <sub>2</sub> supercell
Kinetic energy cutoff	680	820	820	820
Charge density cutoff	6800	8200	8200	8200
Electron k-point grid	12×12×9	14×14×14	16×16×12	16×16×1
Phonon q-point grid	4×4×3	4×4×4	4×4×3	4×4×1

limit for the elastic interface conductance is obtained from the radiation limit. Our DMM predictions use the exact phonon dispersion of bulk Si and bulk CoSi<sub>2</sub> as opposed to a Debye approximation that is commonly used in the literature. The procedure for full-dispersion DMM is described in Ref. [41], and the details of the radiation limit are provided in Ref. [25]. The AGF method uses harmonic inter-atomic force constants (IFCs) to determine the phonon transmission function that is then used in the Landauer approach to determine the thermal interface conductance.

An important development in the present work is the prediction of cross-interface force constants directly from DFPT calculations on a Si (111)-CoSi<sub>2</sub> (111) interface supercell. Our approach is a significant improvement in comparison with common heuristic approximations such as averaging of bulk force constants to obtain interface force constants. Such rigorous predictions of interface bonding strength is important since the phonon transmission function is strongly sensitive to the strength and nature of interfacial bonding. Since the AGF simulations consider strained CoSi<sub>2</sub>, we also perform DMM calculations using the bulk phonon dispersion of strained CoSi<sub>2</sub>. AGF simulations model specular reflection and transmission of phonons at the interface while the DMM assumes that the interface destroys all phase and direction information for the phonons incident on the interface. Hence, the AGF and DMM approaches are expected to represent perfectly smooth and rough interfaces respectively.

In the case of PtSi, the interatomic force constants (IFC) and phonon frequencies were calculated using DFT and PBE revised for solids (PBEsol) [87] as implemented in the Vienna *Ab initio* simulation package (VASP) [88, 89]. Projector augmented wave (PAW) potentials [90] are used to describe the interaction between the valence electrons and the ion cores, and an energy cutoff of 500 eV was used for plane wave expansion. We first determined the lattice parameter of PtSi by using a primitive cell with 8 atoms, in the orthorhombic structure, and a 888 Monkhorst-Pack mesh for integrations over the Brillouin zone. The calculated lattice parameters of  $a=3.60$ ,  $b=5.59$  and  $c=5.92\text{\AA}$  are in good agreement with experimental values of 3.59, 5.57, and 5.91\AA [91]. The second order IFCs were calculated using the Phonopy code [92] with a

supercell of 64 atoms, which is a  $2 \times 2 \times 2$  repetition of the 8-atom primitive cell, and a  $2 \times 2 \times 2$  mesh of special  $k$ -points were used in these calculations. The IFCs matrix in real space was converted to dynamic matrix in reciprocal space by Fourier transforms. The phonon frequencies were then obtained by solving the eigenvalue problem of the dynamic matrix for phonon  $q$  vectors in the Brillouin zone sampled by a  $50 \times 50 \times 50$  mesh in ShengBTE code [93]. DMM modeling for NiSi and TiSi<sub>2</sub> were done in an analogous way, but using their corresponding lattice structures.

### 3.4 Results and discussion

#### 3.4.1 ITC of epitaxial and non-epitaxial silicide-silicon interfaces

The results for room temperature thermal interface conductance of the silicide/Si interfaces on intrinsic silicon substrates are given in Figure 3.5. The thermal conductance of the CoSi<sub>2</sub>/Si and TiSi<sub>2</sub>/Si were both near 480 MW/m<sup>2</sup>-K, similar to a recent report for an epitaxial NiSi<sub>2</sub>/Si interface,[56] but greatly exceeding the highest interfacial thermal conductance for all other previously measured interfaces on silicon, including HF dipped Al/Si interfaces. To within the experimental uncertainty, there was no difference between the measured values of interfacial conductance formed on Si(100) vs Si(111). In other words, the epitaxial interfaces show nearly the same thermal interface conductance as the non-epitaxial interfaces in all cases. However, it appears that if the sources of error in TDTR are systematic (as they are usually are), the non-epitaxial interfaces may even have marginally larger thermal interface conductance than the epitaxial interfaces. Furthermore, in the case of CoSi<sub>2</sub>/Si interfaces, we found no dependence of the thermal interface conductance on the surface preparation method (in situ RF-bias cleaning vs. HF dipped) or the method of silicide formation (reactive method vs. co-sputtering). The interfacial thermal conductance of silicide interfaces is thus found to be quite robust and high so long as the wafer surface is cleaned before the silicide formation. NiSi/Si interfacial thermal conductance is also relatively high,  $G_{\text{NiSi/Si}} \approx 400$  MW/m<sup>2</sup>-K. PtSi has much larger acoustic and phonon density of states contrast with Si compared to the other materials, and as expected its

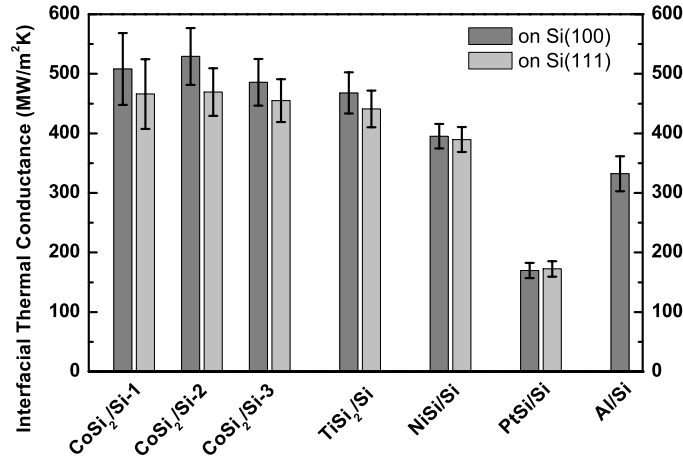


**Figure 3.5:** The interfacial thermal conductance of CoSi<sub>2</sub>, TiSi<sub>2</sub>, NiSi and PtSi on intrinsic Si(100) and Si(111) wafer. CoSi<sub>2</sub>/Si-1, CoSi<sub>2</sub>/Si-2 and CoSi<sub>2</sub>/Si-3 represent samples made under different conditions. CoSi<sub>2</sub>/Si-1: HF treated wafer + films deposited by co-sputtering, CoSi<sub>2</sub>/Si-2: HF treated wafer + films made by reactive growth method, CoSi<sub>2</sub>/Si-3: RF bias treated wafer + films made by reactive growth method. For TiSi<sub>2</sub>, NiSi and PtSi films are made by reactive growth method on RF-bias cleaned substrates. The interfacial thermal conductance of Al/Si(100) is also attached as a reference.

thermal interface conductance is substantially smaller than the other silicides studied, with  $G_{\text{PtSi/Si}} \approx 170 \text{ MW/m}^2\text{-K}$ .

While the observation may seem surprising that the thermal interface conductance of epitaxial silicides is essentially identical to those of non-epitaxial silicides, it is not without precedent. Similar results were reported for epitaxial TiN(001)/MgO(001), TiN(111)/MgO(111) and TiN(111)/Al<sub>2</sub>O<sub>3</sub>(0001) interfaces,<sup>[3]</sup> where it was found that, despite significant differences in lattice mismatch (8% when comparing O-O and N-N distances in the case of TiN/Al<sub>2</sub>O<sub>3</sub>(0001)) and the presence of stacking faults in the case of both TiN(111)/Al<sub>2</sub>O<sub>3</sub>(0001) and TiN(111)/MgO(111), all the interfaces showed the same interface thermal conductance. In that work the authors cite two possible reasons why this might be the case: (1) all samples undergo strong phonon scattering at the interface (including the seemingly perfectly structured ones) and therefore, all

samples satisfy the assumptions of the diffuse mismatch model or (2) the interface disorder in all samples (including the more disordered ones) are weak and the transmission coefficient is always close to unity. We should note that the authors explicitly calculated the DMM for these cases and did not find good agreement. However, they implemented a relatively crude approach to perform the diffuse mismatch model calculations (Debye model). It is well established now that using full phonon dispersions produces substantially different DMM predictions under most circumstances. In addition, the authors utilized lattice dynamics (LD) calculations to predict the results for a perfect epitaxial interface. However, they did not consider local changes in bonding characteristics near the interface, which may also have been important. The DMM and AGF calculations here take these into account. Also, by comparing the experimental data to the calculated radiation limit (the maximum interface conductance consistent with detailed balance in the elastic limit) using full-dispersion relations, we are able to test the hypothesis (2) directly. In all cases, we find that silicide-silicon interfaces are not close to the radiation limit and thus the transmission coefficients are not close to unity (or rather the maximum allowable) for all modes.

Figure 3.6(a) shows a comparison between temperature-dependent  $\text{CoSi}_2$  experiments and our DMM and AGF calculations[2]. Since the experimental Si(111)- $\text{CoSi}_2$ (111) interfaces considered here are epitaxial with submonolayer interfacial roughness it would be reasonable to expect the AGF method to be applicable. We observe, however, that the experimental value of thermal interface conductance ( $\approx 500 \text{ MW/m}^2\text{-K}$ ) exceeds the AGF prediction by more than 50%. At room temperature a full dispersion DMM not accounting for interfacial strain nearly accounts for the data at high temperature. However, employing a modified DMM that incorporates the effect of strain yields slightly worse agreement ( $\approx 10\%$ ).

Given the lack of dependence of the interface conductance upon interface structure (i.e. epitaxial vs. not in Figure 3.5) and the reasonable agreement between experiments and the DMM model in Figure 3.6, it may be tempting to assume that interfaces really act as diffusely to phonons, even for epitaxial interfaces. However, we

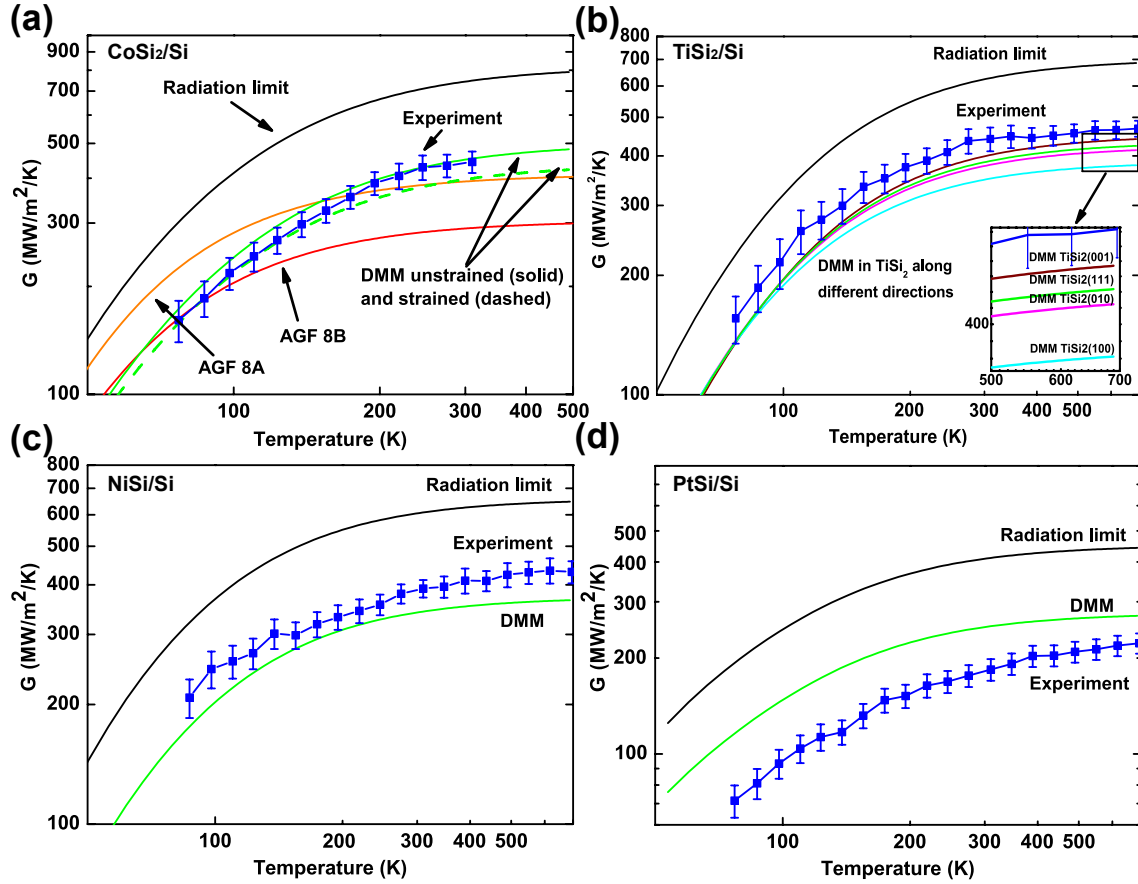


**Figure 3.6:** (a) Modeling results for  $\text{CoSi}_2(111)\text{-Si}(111)$  interfaces using various models: the full-dispersion diffuse mismatch model (green), the atomistic Greens function method for interface of 8B (red) and 8A (orange) and the radiation limit (black). Experimental data at room temperature is shown for comparison (blue squares); (b) Comparison between experimental thermal interface conductance of  $\text{TiSi}_2\text{-Si}(111)$  interface (blue squares), the full-dispersion DMM calculation of  $\text{TiSi}_2(001)$ ,  $\text{TiSi}_2(010)$ ,  $\text{TiSi}_2(100)$ ,  $\text{TiSi}_2(111)\text{-Si}(111)$  and the radiation limit (black); (c) Comparison between experimental thermal interface conductance of an epitaxial  $\text{NiSi}(200)\text{-Si}(111)$  interface (blue squares), the full-dispersion DMM calculation (green) and the radiation limit (black); (d) Comparison between experimental thermal interface conductance of an epitaxial  $\text{PtSi}(020)\text{-Si}(111)$  interface (blue squares), the full-dispersion DMM calculation (green) and the radiation limit (black).

would caution that the observed high temperature discrepancies could also arise without the diffuse assumption, through a combination of inelastic interfacial processes and inter- and intra-material electron-phonon coupling. Neither these processes is included current the model. Electron-phonon coupling within the metal provides a series resistance to the phonon-phonon interface resistance, while cross-interface electron-phonon coupling provides a parallel pathway for coupling between the primary energy carriers of metal and the semiconductor. Sadasivam et al.[46] performed first-principles calculations of electron-phonon coupling near a C49 TiSi<sub>2</sub>-Si interface and found that the coupling of electrons with joint or interfacial phonon modes can potentially produce a conductance similar to the phonon-phonon interfacial conductance (note: in the present paper, we obtained the C54 phase of TiSi<sub>2</sub> which is the lower resistivity phase and is more commonly used for semiconductor applications). Inelastic phonon scattering has been identified as an important transport mechanism for material combinations with a large acoustic mismatch such as Pb and diamond [94, 31]. In the case of CoSi<sub>2</sub> of Si(111), we show in a forthcoming publication that the high temperature behavior of interface conductance can be matched quite well by invoking these mechanisms[2]. It remains unclear, however, whether these mechanisms are insensitive to interfacial structure.

To evaluate if cross-interface electron-phonon with coherence phonon can explain our CoSi<sub>2</sub>(111)/Si(111) data, our collaborators from Purdue University help us do the AGF with considering other phonon transport mechanisms. With the assumption that cross-interface electron-phonon coupling is responsible for the difference between experimental data and the simulation results represented by the red curve in Figure 3.7, we use the coupling coefficient on the Si side of the interface to model energy transfer between electrons in metal and the semiconductor lattice. Curve 'D' in Figure 3.7 represents the thermal interface conductance obtained by coupling electrons in metal with two unit cells of Si closest to the interface along the transport direction. Direct coupling with two unitcells of Si, which represents a length of approximately 1.9 nm, is found to be sufficient to obtain a close match with experimental data at various

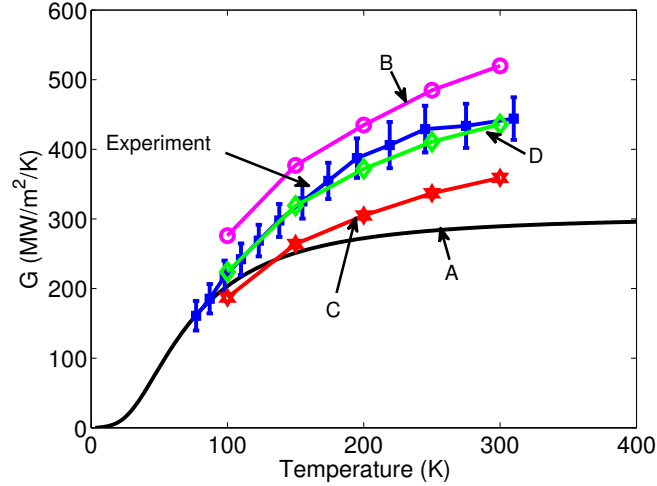


**Figure 3.7:** Comparison of AGF simulation predictions with  $\text{CoSi}_2(111)/\text{Si}(111)$  experimental results (blue squares with error bars). A (black solid curve) - Phonon-only simulation with elastic interface scattering. B (magenta circles) - Phonon-only simulation with anharmonic phonon scattering in both Si and  $\text{CoSi}_2$ . C (red hexagrams) - Electrons and phonons considered in the simulation with electron-phonon energy transfer inside the metal region only. D (green diamonds) - Electrons and phonons considered in the simulation with electron-phonon energy transfer included in two (1.9 nm) unit cells of Si closest to the interface. Reprinted from our collaborator’s paper[2].

temperatures. The close match to experimental data suggests that the extent of joint interface modes in Si is much smaller than the bulk mean free path of Si. The small spatial extent of joint modes is likely due to the increased anharmonicity of interfacial phonon modes as compared to the bulk phonon modes. Similar conclusions regarding increased anharmonicity of the interfacial region are discussed in ref. [95] by computing the anharmonic contribution to the potential energy of interfacial atoms in Si/Ge interfaces.

### 3.4.2 The effect of substrate carrier concentration

While we are not aware of any experimental methods capable of isolating the cross-interface electron-phonon coupling component of thermal conductance from phonon-phonon transport across the interface, we have studied the effect of doping the silicon wafer on the interfacial thermal conductance at room temperature (Figure 3.8). To our knowledge, there are no previous reports of the substrate carrier concentration dependence of thermal interface conductance for any metal-semiconductor interface. If the thermal interface conductance is phonon-dominated, the doping level of the substrate would not be expected to have any effect on the thermal interface conductance, perhaps justifying the lack of existing experiments. On the other hand, if cross-interface electron-phonon coupling is dependent on either band-bending, through Schottky barrier height and depth, or electronic screening, which depends on carrier concentration through the screening length, then we reason that substantial changes to the substrate carrier concentration could affect the electron-phonon coupling component of the thermal interface conductance.

We have studied a wide range of carrier concentrations from degenerate n- to degenerate p-type doping and have found that the thermal interface conductance of the silicides do not show any carrier concentration dependence. In fact, the interface conductance is remarkably consistent and stable against changes to both doping level/type and substrate/film orientation as shown in Figure 3.8. As has been previously reported, however, we do find that the substrate thermal conductivity is appreciably reduced for degenerate levels of either p- or n- type dopants (red squares in Figure 3.8). Note that the extracted substrate conductivities were consistent across the various silicides, which gives additional confidence in the values of heat capacity for the silicides used to extract TDTR data. The decrease in the thermal conductivity of the silicon wafer with increase of the doping concentration (Figure 3.9) is due to the phonon scattering by the impurity atoms and electrons (or holes)[96]. The measured thermal conductivity of the silicon wafer is consistent with past measurements of intrinsic/doped Si performed by TDTR[37].

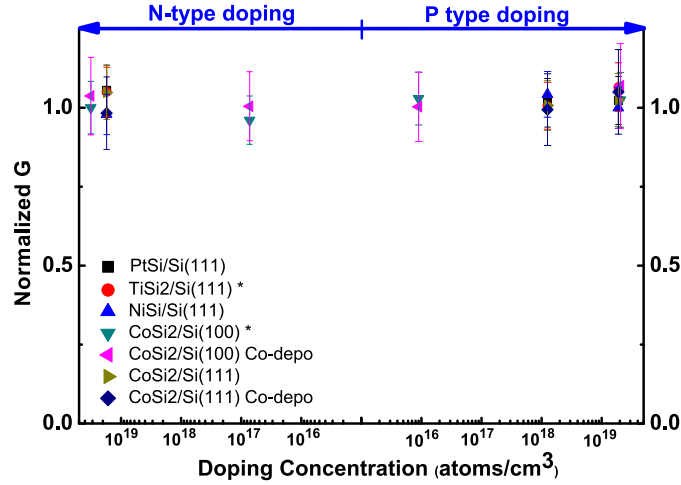


**Figure 3.8:** The substrate doping effects on the interfacial thermal conductance. The thermal conductance values are normalized with their correspondent undoped values. This includes the interfacial thermal conductance of CoSi<sub>2</sub>/Si(111) and CoSi<sub>2</sub>/Si(100) made by co-deposition, CoSi<sub>2</sub>/Si(111), CoSi<sub>2</sub>/Si(100), TiSi<sub>2</sub>/Si(111), NiSi/Si(111) and PtSi/Si(111) made by reactive growth. \* indicates that the interface is not epitaxial. (For original data please refer to Figure 3.9)

### 3.5 Summary

In summary, the thermal interface conductance of CoSi<sub>2</sub>, NiSi and PtSi, TiSi<sub>2</sub>, and Al films with silicon were measured using a series of clean and well-characterized interfaces using TDTR. A few of these (CoSi<sub>2</sub>, TiSi<sub>2</sub> and NiSi) are demonstrated to be extremely good thermal interface conductance materials for Si, and are some of the highest ever measured for a metal-semiconductor interface. Interestingly, we find

that the interfacial thermal conductance is not dependent on whether the interface is epitaxially grown or what the substrate orientation is. A full-dispersion diffuse mismatch model closely predicts the experimentally observed interface conductances for  $\text{CoSi}_2$ ,  $\text{NiSi}$ , and  $\text{TiSi}_2$  interfaces, while it remains an open question whether inelastic scattering, cross-interfacial electron-phonon coupling, or other mechanisms could also account for the high temperature behavior[2]. Above 100K a coherent AGF approach significantly underpredicts interface conductance in the case of  $\text{CoSi}_2$  suggesting that energy transport does not occur purely by coherent transmission of phonons, even for epitaxial interfaces. AGF with considering the cross interface electron phonon coupling could also explain the experimental data. The effect of degenerate semiconductor dopant concentration on metal-semiconductor thermal interface conductance was also investigated with the result that we have found no dependencies of the thermal interface conductances up to (n-type or p-type)  $\approx 1 \times 10^{19} \text{ cm}^{-3}$ , indicating that there is no significant direct electronic transport and no transport effects which depend on long-range metal-semiconductor band alignment.

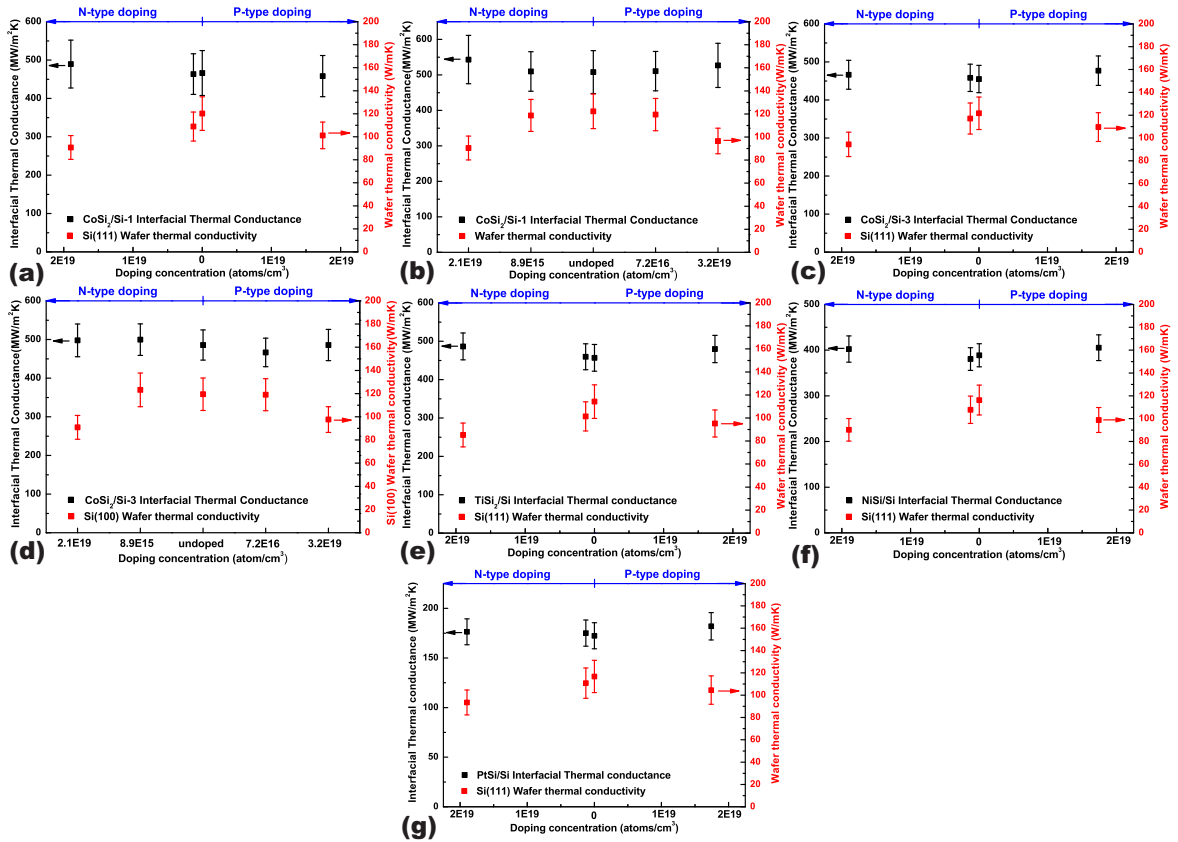


**Figure 3.9:** Interfacial thermal conductance and wafer thermal conductivity vs. wafer doping concentration of (a) and (b) CoSi<sub>2</sub> films made by co-sputtering on HF treated Si(111) and Si(100) wafer; (c) and (d) CoSi<sub>2</sub> films made by reactive growth method on RF bias treated Si(111) and Si(100) wafers; (e), (f) and (g) TiSi<sub>2</sub>, NiSi and PtSi made by reactive growth method on RF treated Si(111) wafers.

## Chapter 4

### THERMAL CONDUCTANCE OF EPITAXIAL $\text{NiAl}_{1-x}\text{Ga}_x$ -GAAS INTERFACES: A STUDY OF PHONON BAND ENGINEERING

#### 4.1 Motivation

Intermetallic compounds like NiAl and FeAl are widely utilized in applications where high operating temperature and high mechanical strength are simultaneously required, such as the turbine blades of aircraft and other advanced aerospace structures[97, 98]. These compounds have high melting points for a structural material (1911 K), excellent corrosion resistance and good thermal conductivity[99].

In the magnetic recording industry, NiAl is also widely used as underlayers for longitudinal magnetic recording medium. Li-Lien Lee et. al[100] found that NiAl was in the highly ordered B2 structure with similar lattice parameter to Cr, and thus NiAl was an idea substitute for Cr as the underlayer of longitudinal magnetic recording mediums. CoCrTa medium grown on NiAl were found with heteroepitaxially texture structure and higher in-plane coercivity than that grown on Cr. NiAl was also used as the seed layers for other longitudinal magnetic recording mediums, such as CoCrPt and CoCrPtTa[101].

As a model system for understanding thermal transport across interfaces, there are a few interesting aspects about  $\text{NiAl}_{1-x}\text{Ga}_x$  alloy/GaAs substrate. First, NiAl and NiGa both have simple cubic primitive unit cells with similar lattice parameters of 2.88 Å and 2.886 Å respectively. The lattice mismatch of NiAl and NiGa is less than 0.2%. Second, because Al and Ga are both XIII group in the periodic table, the outer electronic orbitals of these two elements are the same, which makes the chemical bonding or the force constant of Ni-Al and Ni-Ga quite similar. That means if Al is randomly swapped for Ga in the alloy, the change in lattice parameter and force

constant of the bonding are negligible and what we are changing is only the atomic mass. Third, GaAs is zinc blende cubic crystal structure with lattice constant 5.65 Å, which is almost exactly twice as that of any  $\text{NiAl}_{1-x}\text{Ga}_x$  alloy. The lattice mismatch between  $\text{NiAl}_{1-x}\text{Ga}_x$  alloy and GaAs is less than 2%, which makes GaAs a perfect substrate for epitaxial growth of  $\text{NiAl}_{1-x}\text{Ga}_x$  alloy. Lastly, NiAl and NiGa are both metallic, and have high thermoreflectance coefficient, making them and their alloys naturally good transducers for direct TDTR measurements.

In this chapter, we explore how modifications of the phonon dispersion in  $\text{NiAl}_{1-x}\text{Ga}_x$  alloys effect thermal transport across epitaxial interfaces to GaAs. Epitaxial  $\text{NiAl}_{1-x}\text{Ga}_x$  - GaAs interfaces are fabricated across a wide range of alloy compositions from  $0 < x < 1$ , and the thermal conductance of these interfaces is studied by time-domain thermoreflectance (TDTR) from 77-700K. Phonon dispersion is modeled using a density functional perturbation theory via the virtual crystal approximation, and the dispersion is used to predict the transport using the diffuse mismatch model.

## 4.2 Experiment and modeling

The  $\text{NiAl}_{1-x}\text{Ga}_x$  alloy was deposited by co-sputtering of NiAl (Kurt J. Lesker Company, 99.99%) and NiGa targets (Kurt J. Lesker Company, 99.9%) with two RF magnetron sputtering sources in the PVD chamber (PVD products, Wilmington, MA). Before deposition, GaAs(100) single crystal substrate (Universal wafer) was raised up to 400 °C for 5 min to allow the substrate temperature to stabilize. The alloy composition was controlled by varying the power of each sputtering gun separately while the total sputtering rate of the alloy and sputtering time were fixed. The thickness of all the alloy films was controlled to be 90 nm to make sure the laser fully absorbed in  $\text{NiAl}_{1-x}\text{Ga}_x$  film. Then, substrate temperature was lowered and samples were held in the chamber for 2 hours to fully cool down before taken out. The crystal structure and epitaxial nature of the films was confirmed using X-ray diffraction (XRD) and the thicknesses of the films were verified with X-ray reflectivity (XRR). XRD and XRR were performed on Rigaku Ultima IV X-ray diffractometer. XRD results of selected epitaxial  $\text{NiAl}_{1-x}\text{Ga}_x$

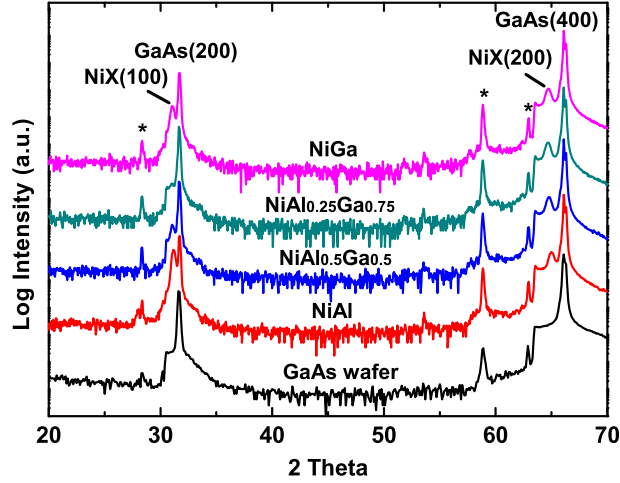


**Figure 4.1:** XRD spectra of GaAs wafer (black), NiAl film (red), NiAl<sub>0.5</sub>Ga<sub>0.5</sub> film (blue), NiAl<sub>0.25</sub>Ga<sub>0.75</sub> film (dark cyan) and NiGa film (magenta). Curves are offset for clarity. NiX indicates the peaks from NiAl<sub>1-x</sub>Ga<sub>x</sub> alloy. \* indicates the contamination peaks from the single crystal substrate.

alloy films on GaAs are shown in Figure 4.1. Only peaks from diffraction planes of NiAl(100), NiAl(200), GaAs(200) and GaAs(400) are found in the XRD patterns. No other peaks are found, indicating that NiAl<sub>1-x</sub>Ga<sub>x</sub> alloy grow epitaxially along the [100] direction of the GaAs(100) wafer. It is noticed that NiAl<sub>1-x</sub>Ga<sub>x</sub>(200) peaks have similar intensities in the XRD for the four alloy compositions shown. However, NiAl<sub>1-x</sub>Ga<sub>x</sub>(100) do have different intensities. Specifically, as the alloy composition is increasing from  $x = 0$  to  $x = 1$ , the intensity of (100) peak decreases until totally disappears at composition  $x = 0.75$ , and then the intensity of (100) increases. One likely explanation for this is that when the NiAl<sub>1-x</sub>Ga<sub>x</sub> composition is close to  $x = 0.75$ , the atomic mass of Ni site becomes the same as the average atomic mass of (Al<sub>0.25</sub>Ga<sub>0.75</sub>) site, which increases the apparent symmetry of the lattice and make the (100) a forbidden reflection.

The thermal conductance of NiAl<sub>1-x</sub>Ga<sub>x</sub> alloy GaAs interface and thermal conductivity of the substrate were measured by TDTR with a modulation frequency of 12.6 MHz. NiAl<sub>1-x</sub>Ga<sub>x</sub> alloy was used as the transducer in the TDTR measurement. Room temperature electrical conductivity of the NiAl<sub>1-x</sub>Ga<sub>x</sub> alloys was measured using an inline four point probe with regression to an I-V curve. Wiedemann-Franz Law was used to take advantage of the known electrical results to estimate the thermal conductivity. The room temperature electrical conductivity and corresponding electrical portion of thermal conductivity are shown in Figure 4.3. The temperature dependent thermal conductivity of NiAl and NiGa are estimated using the measured room temperature electric resistivity combined with literature reported temperature coefficient of resistivity[99]. The temperature coefficients of resistivity for the NiAl<sub>1-x</sub>Ga<sub>x</sub> alloy composition are estimated from those of NiAl and NiGa by composition-weighted linear interpolation. The thermal conductivity of NiAl<sub>1-x</sub>Ga<sub>x</sub> alloy was high enough to yield good sensitivity to thermal interface conductance. The room temperature sensitivities of NiAl and NiGa on GaAs is shown in Figure 4.2. The analysis of the TDTR data for the ITC and thermal conductivity of the substrate were done in the time range of 500ps - 3700ps, where the sensitivity of the signal is weak to the thermal conductivity of the transducer and strong to the ITC and the thermal conductivity of substrate. By doing this, we minimize error due to uncertainties in the transducer's thermal conductivity.

Diffuse mismatch modeling (DMM) predictions using full phonon dispersion[41] were calculated and compared to the experimental results. The phonon dispersions in the NiAl<sub>1-x</sub>Ga<sub>x</sub> alloy and GaAs were calculated by density function perturbation theory (DFPT) with quantum-espresso version 5.0.2[49]. The exchange correlation energy was approximated under the generalized gradient approximation (GGA) using the Perdew-Burke-Ernzerhof (PBE) functional form. Rappe-Rabe-Kaxiras-Joannopoulos (RRKJ) ultrasoft pseudopotentials were used for the atoms in NiAl, NiGa and GaAs phonon dispersion calculations in the project. Force constants of stoichiometric NiAl and NiGa compounds were obtained from DFPT. IFCs and Al/Ga-site mass of alloys were obtained by compositionally-weighted average. The 'virtual crystal' IFC's and

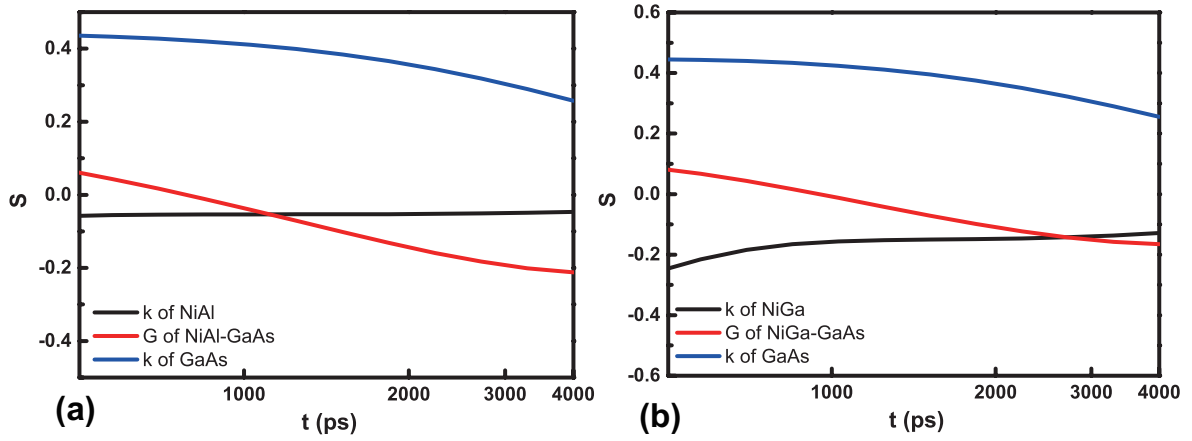


Figure 4.2: Sensitivity plots of NiAl (a) and NiGa (b) on GaAs at room temperature

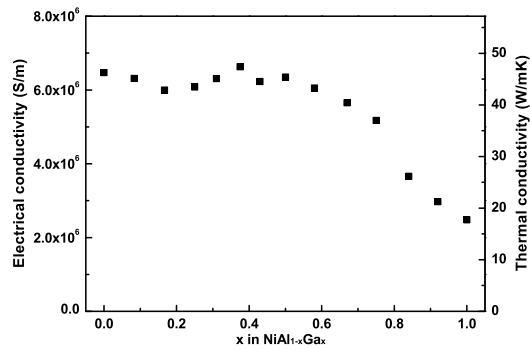


Figure 4.3: Room temperature electrical conductivity of NiAl<sub>1-x</sub>Ga<sub>x</sub> alloys vs. composition

masses were used to generate the phonon dispersions of the alloys.

### 4.3 Results and discussion

The phonon density of states of  $\text{NiAl}_{1-x}\text{Ga}_x$  alloy and GaAs calculated by DFPT is shown in Figure 4.4. For each graph, the red line and black line respectively represent the phonon density of states of  $\text{NiAl}_{1-x}\text{Ga}_x$  with different composition and GaAs. Since the ITC of a metal-semiconductor interface is expected to be dominated by phonon transport, the degree of matching between phonon density-of-states in the two interfaced materials should give an indication of the relative ease of transport (overlap in the density-of-states is associated with high phonon transmission). As it is shown in Figure 4.4(a), the maximum optical phonon frequency of NiAl is around 11 THz, which is much larger than that of GaAs, 8.8 THz. Moreover, there is a phonon band gap between 6 to 7.6 THz in the phonon density of states of the NiAl spectrum. That indicates that the thermal energy carried by GaAs phonons with frequency of 6 to 7.6 THz cannot transport across the interface. This will result a low thermal conductance of NiAl-GaAs interface. While the Ga content,  $x$ , increases, the maximum optical phonon frequency decreases and the phonon band gap becomes smaller until it eventually vanishes altogether. At  $x=0.6$ , the optical phonons of the  $\text{NiAl}_{1-x}\text{Ga}_x$  alloy and GaAs match best and the phonon band gap in  $\text{NiAl}_{1-x}\text{Ga}_x$  alloy disappears. Further increase of  $x$  will lead the maximum optical phonon frequency of  $\text{NiAl}_{1-x}\text{Ga}_x$  alloy to be smaller than that of GaAs, but do serve to make the acoustic phonon match better. For NiGa/GaAs interfaces, the maximum optical phonon frequency of NiGa is 7.6 THz, just a little lower than that of the optical phonons in GaAs. The acoustic phonons of NiGa are aligned much better with that of GaAs than that of NiAl. From the phonon density of states, we thus expect to see an increase of ITC for  $\text{NiAl}_{1-x}\text{Ga}_x$  - GaAs while  $x$  increases from 0 to 0.6. After  $x = 0.6$ , because of misalignment in the optical phonon density of states and the optical phonons with high energy, we might expect to see a decrease of ITC.

Figure 4.5 shows the ITC measured by TDTR and as well as that calculated

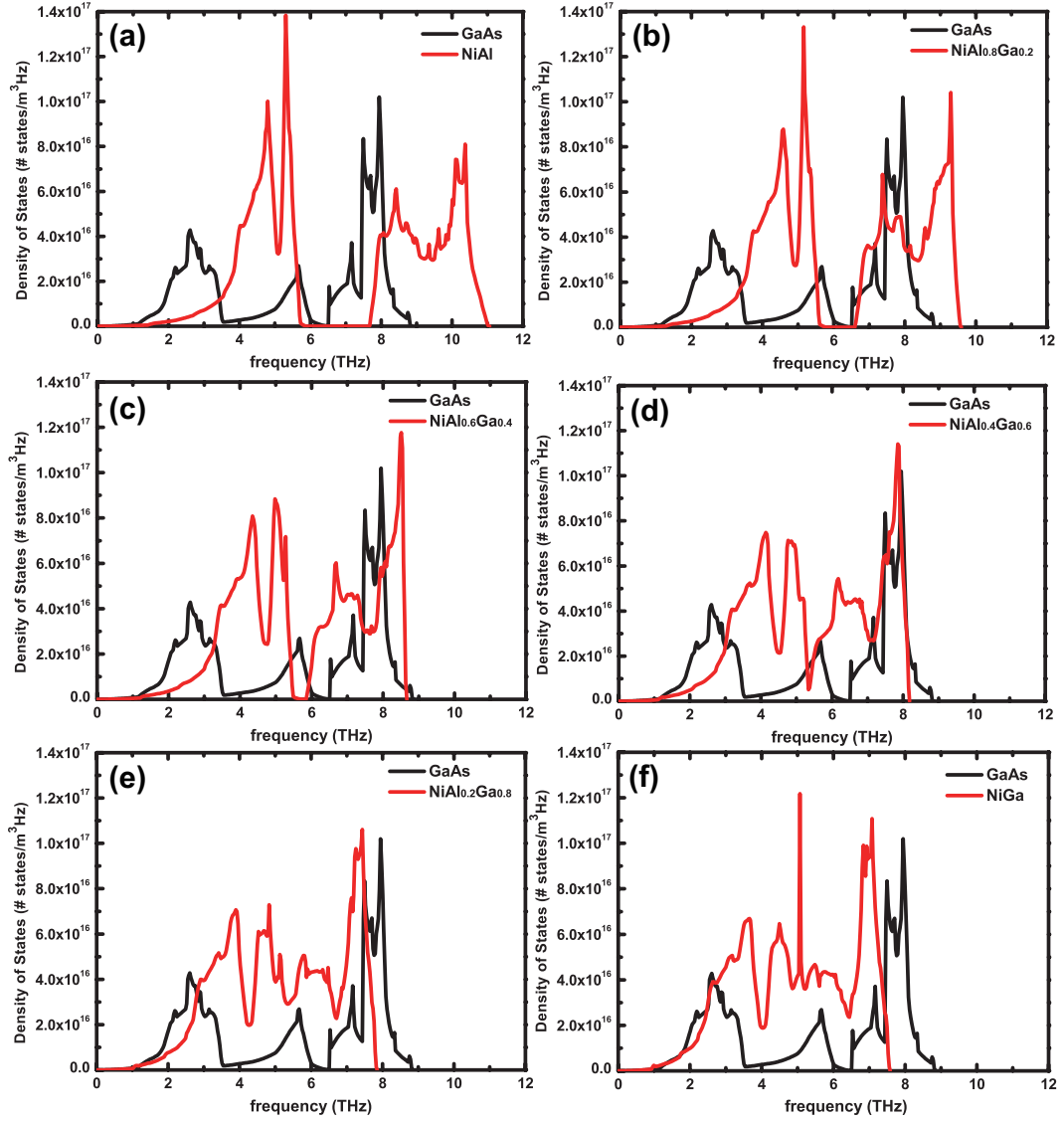


**Figure 4.4:** Comparison of the density of states of NiAl<sub>1-x</sub>Ga<sub>x</sub> alloy (red) and GaAs (black): (a)  $x = 0$ ; (b)  $x = 0.2$ ; (c)  $x = 0.4$ ; (d)  $x = 0.6$ ; (e)  $x = 0.8$ ; (f)  $x = 1$ .

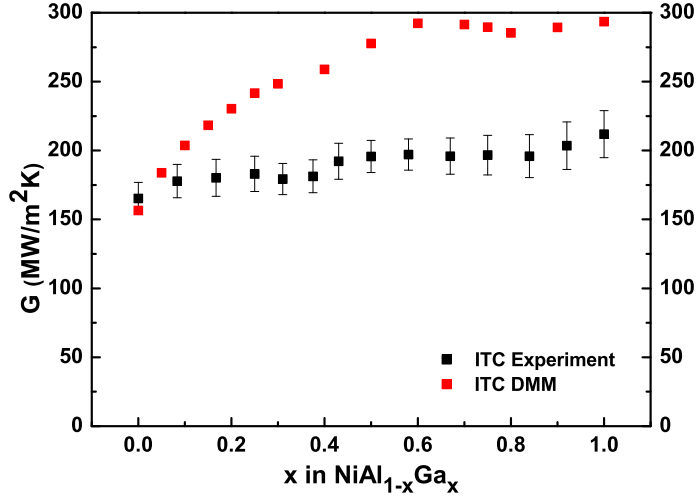


**Figure 4.5:**  $G$  of  $\text{NiAl}_{1-x}\text{Ga}_x$  alloys with different  $x$  compositions on GaAs: measured by TDTR at room temperature (black); calculated by DMM at room temperature (red).

by full phonon dispersion DMM at fixed temperature (300K). At  $\text{NiAl}_{1-x}\text{Ga}_x$  - GaAs interfaces, as  $x$  increases from 0 to 1, the measured ITC almost linearly increases from 160  $\text{MW}/\text{m}^2\text{-K}$  to 210  $\text{MW}/\text{m}^2\text{-K}$ , an increase of 30%. On the other hand, the DMM-predicted ITC increases quickly with composition  $x$  in the range between  $x = 0$  and  $x = 0.6$  due to rapid rearrangement (overlapping) of optical phonons. Predictions calculate a near-doubling of conductance from 150  $\text{MW}/\text{m}^2\text{-K}$  to 300  $\text{MW}/\text{m}^2\text{-K}$ . After  $x = 0.6$ , the ITC predicted by DMM almost remains a constant, consistent with a tradeoff between better matching of acoustic modes vs worse matching of optical modes with increasing  $x$ . In general, the DMM predicts the ITC of NiAl well but is quite unsatisfactory for most other compositions.

Figure 4.6 shows the spectral contributions to ITC vs. the phonon frequency at room temperature (293 K) calculated by the DMM. The spectral contributions to ITC,  $G_{\text{spectrum}}$ , is also calculated from DMM equation 2.5. However, instead of summing over all phonon modes and wave vectors over whole Brillouin zone to get

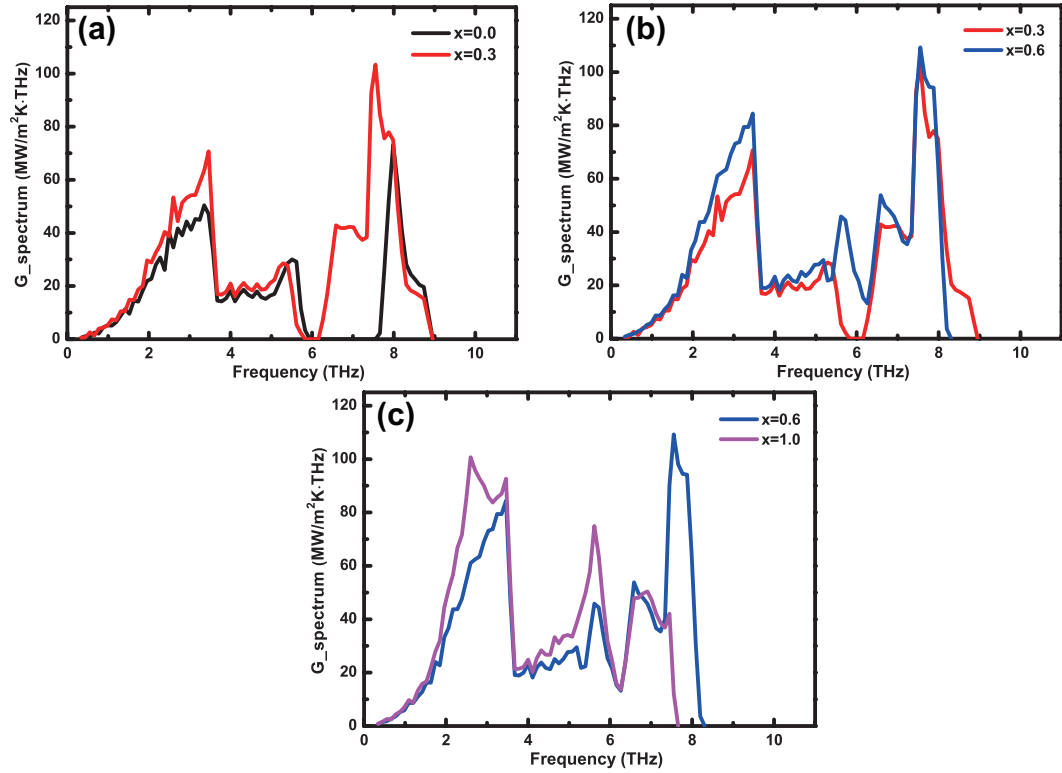


**Figure 4.6:** (a) Comparison of DMM calculated G\_spectrum of composition  $x = 0$  (black) and  $x = 0.3$  (red) at room temperature; (b) Comparison of DMM calculated G\_spectrum of composition  $x = 0.3$  (red) and  $x = 0.6$  (blue) at room temperature; (c) Comparison of DMM calculated G\_spectrum of composition  $x = 0.6$  (blue) and  $x = 1.0$  (violet) at room temperature

total  $G$  at specific  $T$ , only the phonons with specific frequency over the whole Brillouin zone are summed. In this way,  $G(\omega)$  is calculated for all possible frequencies. In order to make the area of the  $G$ -spectrum in the graph represent the total ITC of a specific composition,  $G(\omega)$  is then normalized with frequency to get  $G$ -spectrum, in units of  $\text{MW}/\text{m}^2\text{-K}$  per  $\text{THz}$ . This plot aids in the mechanistic interpretation of how transport changes with alloy composition. From  $x = 0$  to  $x = 0.3$ ,  $G(\omega)$  is the same since the maximum optical frequency of  $\text{NiAl}_{0.7}\text{Ga}_{0.3}$  alloy is still larger than that of  $\text{GaAs}$ . Most of the increase in ITC is from the heat carried by the acoustic phonons and the phonons with frequency at the  $\text{NiAl}$  phonon band gap region. From  $x = 0.3$  to  $x = 0.6$ , although there is some decrease in the  $G(\omega)$  near the upper frequencies, the increase from the acoustic phonons and the phonons with frequency at the  $\text{NiAl}$  phonon band gap region still dominate the increase in the total ITC. When the composition is higher than  $x = 0.6$ , the decrease of  $G(\omega)$  at the maximum frequency becomes important and the increase in the acoustic phonons and  $\text{NiAl}$  phonon band gap region is comparable to the decrease, which will result in a constant ITC at composition range of  $x = 0.6$  to  $x = 1.0$ .

The temperature dependent ITC of  $\text{NiAl}_{1-x}\text{Ga}_x\text{-GaAs}$  measured by TDTR are shown in Figure 4.7, as well as the corresponding DMM calculations. Overall, the ITC from DMM matches the experiment results for  $\text{NiAl}$  very well, but fails to predict the experiment results for the alloy and  $\text{NiGa}$ . The model over-predicts the  $\text{NiAl}$  experiment results at low temperature and under-predicts the experiment at high temperature. This is similar to our results with silicides-silicon interfaces[81]. The experimentally measured ITC always increases quicker than the DMM values. This could be because DMM does not consider anharmonic phonon effects. For alloys and  $\text{NiGa}$ , DMM severely over predicts the experimental results. However, if we overlook the absolute ITC value provided by DMM, actually the DMM successfully predicts the relative trends of the experiment ITC vs. temperature among compositions. For example, both of the ITC from DMM and experiment show an increasing difference as we increase temperature between composition  $x = 0$  and  $x = 0.25$ . This could be

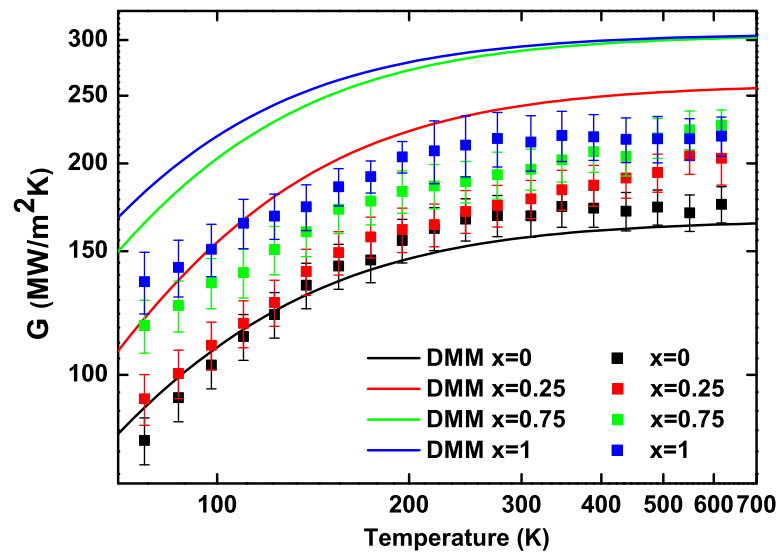


**Figure 4.7:**  $G(T)$  measured by TDTR (squares) and calculated by DMM (lines),  $x = 0$  (black);  $x = 0.25$  (red);  $x = 0.75$  (green);  $x = 1$  (blue)

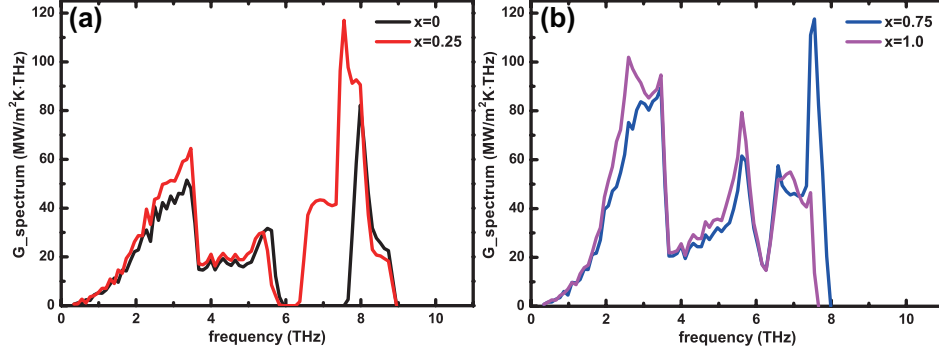


**Figure 4.8:** (a) Comparison of DMM calculated  $G_{\text{spectrum}}$  of composition  $x = 0$  (black) and  $x = 0.25$  (red) at 700 K temperature; (b) Comparison of DMM calculated  $G_{\text{spectrum}}$  of composition  $x = 0.75$  (blue) and  $x = 1.0$  (violet) at 700 K

explained from the  $G_{\text{spectrum}}$  vs.  $f$  of DMM calculated at 700 K in Figure 4.8(a). In spectrum, we can see that most of the increase in ITC from  $x = 0$  to  $x = 0.25$  is at the optical phonon region, with frequency of 6.5 THz to 8 THz. These high energy phonons require high temperature to excite. On the contrary, both of the ITC from DMM and experiment are showing an decreasing difference as we increase temperature between composition  $x = 0.75$  and  $x = 1$ . The reason is that, compared to composition  $x = 0.75$ , total ITC at  $x = 1$  has more contribution from the acoustic phonon instead of optical phonon. However, these are offsetting effects, since loss in optical phonon contribution result in gain of acoustic transmission.

#### 4.4 Summary

Full phonon dispersion DMM is used to calculate the ITC of  $\text{NiAl}_{1-x}\text{Ga}_x\text{-GaAs}$  interfaces. DMM predicts that ITC could increase by 100% as the alloy composition increased from  $x = 0$  to  $x = 1$  by optimized the phonon bandstructure. The experiment results do confirm a increasing behavior, but the magnitude is not as large, indicating that other physics may contribute. For temperature dependent ITC, DMM indicates a slower increasing behavior than ITC measured by TDTR.

## Chapter 5

### GROUP IV EPITAXIAL METAL NITRIDES SYSTEMS WITH ULTRAHIGH INTERFACIAL THERMAL CONDUCTANCE

#### 5.1 Motivation

Transition metal nitrides are widely used industrially due to their outstanding properties including high hardness and mechanical strength, stability with respect to chemicals, and electronic properties which range from metallic (TiN) to semiconducting (ScN) to insulating (AlN). These make the nitrides widely used for different purposes, such as coatings for hard wear-resistant surface[102], diffusion barriers[103], thermoelectric devices[104] and underlayers for magnetic storage applications[105]. The group IV metal nitrides in particular have excellent electrical conductivities ( $\sigma > 2 \times 10^6$  S/m), which thus also yield high electrical portion of thermal conductivity. TiN, for example, has a thermal conductivity exceeding that of even pure Ti.

In one of the only previous studies of epitaxial interfaces to date, Costescu[3] reported ultra high interfacial thermal conductance of TiN-MgO and TiN-Al<sub>2</sub>O<sub>3</sub> interfaces. The reasons attributed to the high thermal conductance at the interface were unclear. One of the possible reasons the authors suggest is that TiN forms high quality epitaxial structures on single crystal MgO and Al<sub>2</sub>O<sub>3</sub> substrates, resulting in a full transmission of the phonons without scattering across the interfaces. At the time of this study, advanced computational methods were not readily available. Costescu was only able to compare against a crude FCC lattice dynamics model considering only nearest neighbor interactions and only one atom per unit cell (i.e. neglecting optical phonons completely, as well as acoustic phonon anomalies (softening) known to occur in the group IV nitrides). This model overestimated conductance by  $\approx 70\%$ . They

also compared against a crude version of the DMM, considering only a Debye dispersion of acoustic phonons and ignoring transmission into optical modes. Neither model matched the data well, but the DMM came the closest ( $\approx 50\%$  overpredicted data). We contend that neither of the theoretical models considered by Costescu should be used as a basis for comparison, thought, since neither model properly accounts for even the phonon dispersion of zone edge and optical phonons. In particular, the lattice dynamics model over attributes the heat capacity due to acoustic phonons and treats them as propagating. This should greatly overpredict their potential to contribute to transport. In this chapter, we perform the analogous calculation correctly, using the full phonon dispersions on both sides of the interface.

Recently, Bivas Saha et al. formed epitaxial TiN/(AlSc)N metal/semiconductor superlattices and studied the thermal conductivity of superlattices with different period thicknesses[106]. In their results, they found that when the period thickness was less than 4 nm, phonon scattering from individual interfaces weakens due to coherent effects (formation of minibands), but when the period thickness is larger than 4 nm phonon scattering from individual interfaces became the dominant effect. Interpreting their reported thermal conductivity as a stacked series of interface resistances yields an ITC for TiN/(AlSc)N interface of  $1.2 \pm 0.12$  GW/m<sup>2</sup>-K at room temperature, a very large value. However, the distinction between coherent and incoherent transport in a superlattice is unclear and separating reduced material thermal conductivity from interface resistance is also challenging. Thus it is unclear whether superlattice thermal conductivity should be interpreted in this way.

To elucidate the effects behind high TiN/MgO interface conductance and to broaden the scope of studied nitride interfaces, this chapter focuses on the preparation and study of a variety of group IV metal nitride transducers (TiN, ZrN, and HfN) epitaxially grown on MgO substrates and as well as on thick layers of ScN semiconductor. In all cases, the materials have rocksalt crystal structure with similar lattice constant. By varying the Group IV metal, the mass of the metal's light atom is able to be independently tuned, allowing the ability to modify the acoustic phonon frequencies

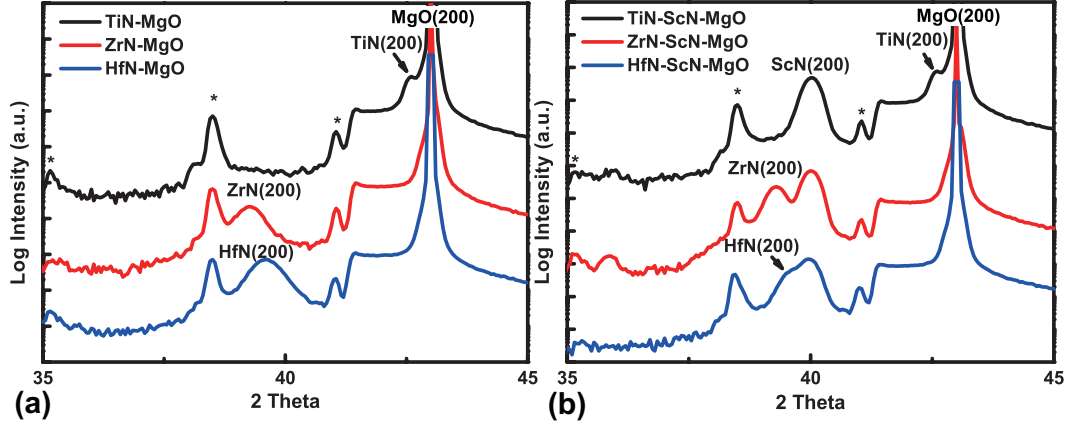


**Figure 5.1:** (a) XRD of TiN (black), ZrN (red) and HfN (blue) on MgO substrate; (b) XRD of TiN (black), ZrN (red) and HfN (blue) on ScN nitride film/MgO substrate

in the metal without significantly effecting the optical phonon band structure.

## 5.2 Experiment

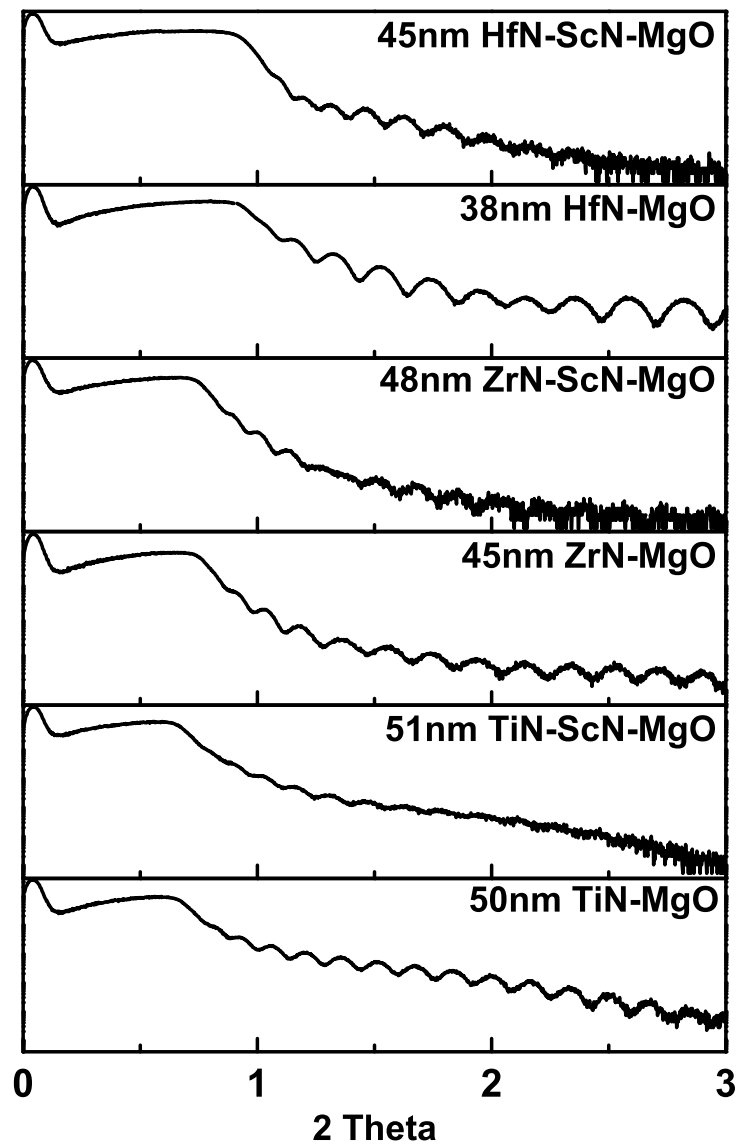
The nitrides in this project were grown on MgO(100) substrates at 750 °C in 10mtorr Ar/N<sub>2</sub> (4 sccm Ar/6 sccm N<sub>2</sub>) from the elemental Titanium (99.99%), Zirconium (99.99%), Hafnium (99.99%) and Scandium (99.998%) by DC reactive magnetron sputtering (PVD Products, Inc.)[107]. Ti, Zr and Hf are all group IV elements with increasing atomic mass. The corresponding nitrides are rock-salt crystal structure with lattice parameters of 4.28 Å for TiN, 4.58 Å for ZrN and 4.54 Å for HfN[108]. Meanwhile, MgO and ScN are dielectric materials also with rock-salt crystal structure with lattice parameters of 4.21 Å and 4.51 Å. Therefore, MgO and ScN are a great template for epitaxial growth of the group IV metal nitrides. As it is shown in Figure 5.1, the group IV metal nitrides all formed epitaxial structure on MgO(100) wafer or MgO(100) with ScN(100) under-layer.

The ITC of group IV metal nitrides on MgO and on ScN interfaces were measured with TDTR. The nitride films have excellent thermorefectance coefficient and were used as the transducer. Since the reported ITC of epitaxial TiN-MgO is high, in

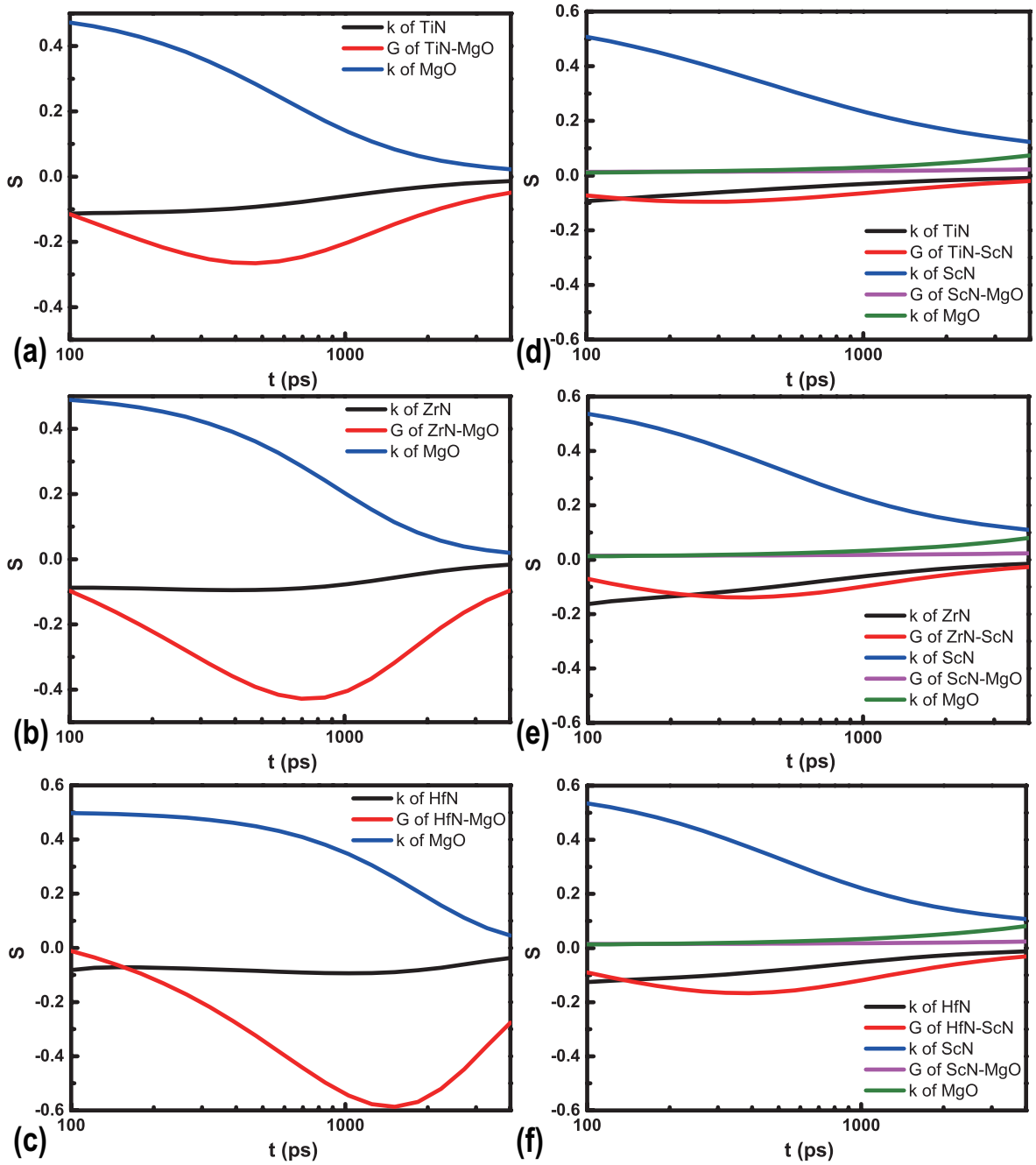
order to get enough sensitivity to the ITC in the TDTR measurement, the thickness of the group IV metal nitrides is kept small, around 40 to 50 nm. This decreases the sensitivity of the experiments to the metal transducer thermal conductivity, since the transducer thermal conductivity can only be independently estimated by Weidemann Franz Law. The challenge of using such a thin layer of transducer in TDTR is that, it then becomes critical to get precise value of the thickness of transducer for an accurate interpretation of TDTR data. This was accomplished by XRR. Figure 5.2 is the transducer thickness measured by XRR. For the ITC of group IV metal nitrides on ScN, the thickness of ScN is controlled to be around 450 nm (i.e. thick) to reduce the influence from ScN/MgO interface. Since the thickness of ScN is large it was independently measured by cross-section SEM, which yields acceptable uncertainty (5%) for data fitting purposes.

Figure 5.3 shows the sensitivity plots of group IV metal nitrides on MgO and ScN. For the group IV metal nitrides on MgO, the measurements have good sensitivity to the ITC and very little sensitivity to the thermal conductivity of the metal transducer. For the group IV metal nitrides on ScN, the sensitivity to ITC is not as good as that on MgO. The reason is that the extraordinarily high ITC value on ScN and the relatively low thermal conductivity of ScN combine to partially mask the thermal resistance of the interface. Note than the thermal conductivity of ScN is about half of thermal conductivity of MgO. Especially for TiN/ScN/MgO, the sensitivity to ITC is rather small making the measurement of TiN/ScN/MgO challenging. However, because the *shape* of the sensitivity curve is distinguishable from  $k_{TiN}$  and  $k_{ScN}$ , we will show that it is possible to perform a 3-variable fit to the data and achieve acceptable accuracy.

Since some of the desired measurement quantities in this chapter have smaller-than-usual sensitivities, it is important to calculate the error bars correctly. The estimation of error bars in the data analysis for this chapter was thus processed in an more advanced way. In traditional TDTR data analysis, the error estimation is dealt with using linear analysis, in other words sending an single perturbation for each related



**Figure 5.2:** XRR measurements of transducer thickness of epitaxial TiN/MgO, TiN/ScN/MgO, ZrN/MgO, ZrN/ScN/MgO, HfN/MgO, HfN/ScN/MgO.



**Figure 5.3:** Sensitivity plots of group IV metal nitrides on MgO and ScN at room temperature. (a)TiN/MgO sample; (b)ZrN/MgO; (c)HfN/MgO; (d)TiN/ScN/MgO; (e)ZrN/ScN/MgO; (f)HfN/ScN/MgO

input parameter to get absolute values of error on the fitting parameters, and then calculating the overall error by taking the square root of the sum of the squares resulting from independent ‘error bars’ for all the different perturbations. This calculated RMS error implicitly assumes symmetric errorbars consistent with linear analysis. In this project, the error is treated instead using a Monte-Carlo type statistical approach: we send perturbations on all the inputs, each following Gaussian distributed errors, simultaneously and then repeat the process 20 times per fitting variable (i.e. if we fit 3 variables simultaneously, we fit the data 60 times using different randomly generated sets of input parameters, consistent with the statistical uncertainty in the input values). To obtain the plus and minus error bars we take the RMS of all the positive errors and negative errors separately. We have verified that this approach reproduces symmetric errorbars with size consistent with our usual linear-analysis approach for simple test cases where linear-analysis applies. Both approaches implicitly consider cross-correlation of errors when a multivariable fit is performed.

### 5.3 Results and discussion

Figure 5.4(a)-(c) show the comparison of phonon density of states of nitride transducers and MgO. Unlike the group IV nitrides, the phonon density of states for MgO is distributed continuously from 0 to 21 THz. In TiN, phonon density of states is distributed from 0 to 8.5 THz and 15 to 17 THz, with a phonon band gap in between. In ZrN, phonon density of states is distributed from 0 to 7 THz and 13 to 15 THz, with a phonon band gap between 7 to 13 THz. In HfN, phonon density of states is distributed from 0 to 6 THz and 16 to 18 THz, with a phonon band gap of 6 to 16 THz. From TiN to HfN, the phonon band gap increase substantially. The maximum frequency of acoustic phonon decreases substantially while the optical phonon has exhibits only a modest change. This causes the phonon density of states the group IV nitrides and MgO to overlap less and less as the group IV mass is increased. The reason that the phonon band gap widens in the nitrides is because of the increasing difference of atomic masses of the metal atom and nitrogen atom. The maximum acoustic phonon

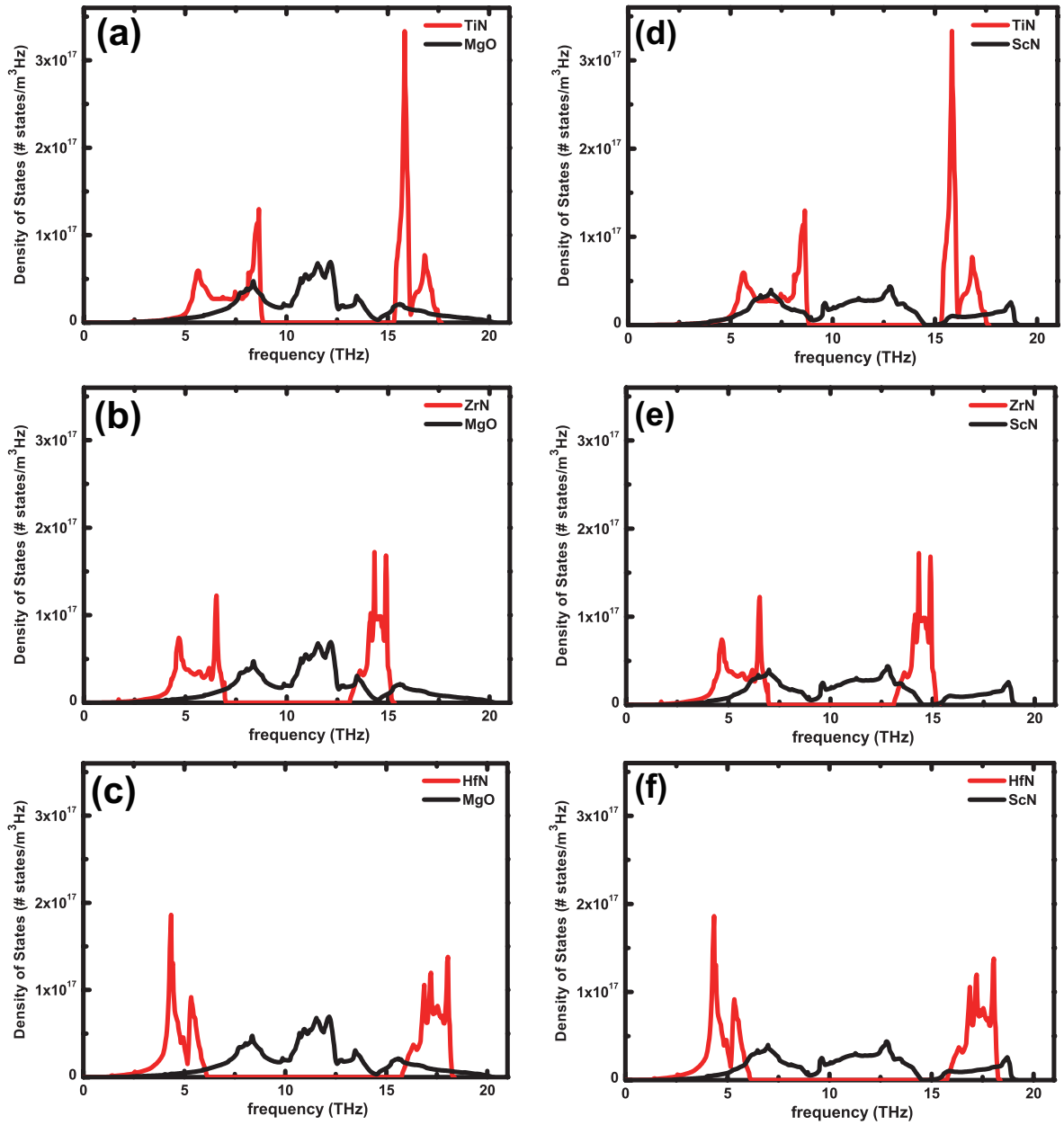


**Figure 5.4:** Comparison of phonon density of states of the nitride transducer and the beneath dielectric material. Red and black lines are respectively referring to nitride transducer and dielectrics. (a) TiN-MgO; (b) ZrN-MgO; (c) HfN-MgO; (d) TiN-ScN; (e) ZrN-ScN; (f) HfN-ScN.

frequency decreases due to the fact that average molecular weight is increasing. As a result, going from TiN to HfN, the acoustic velocity decreases from 10.1 km/s to 6.4 km/s. Therefore, we are expecting to see a decrease in ITC from TiN to HfN when interfaces with MgO. Figure 5.4(d)-(f) show the comparison of phonon density of states of nitride transducer and ScN. The electronic structure and chemistry of ScN are very different from that of TiN (or ZrN, HfN), and ScN is in fact known to be a semiconductor. In ScN, there is no phonon band gap in its phonon dispersion. In fact, the phonon dispersion in ScN is quite similar to that in MgO. The phonon modes are distributed from 0 to 19.5 THz continuously in ScN. Since the phonon dispersion of ScN and MgO are similar, we would expect to see a similar ITC between the group IV metals nitrides on MgO and on ScN, if the interface conductance only depends on the bulk dispersion relations (as predicted by models such as the DMM and the AMM).

The temperature dependent ITCs of epitaxial TiN-MgO, ZrN-MgO, and HfN-MgO interfaces are shown in Figure 5.5. The ITC of the TiN-MgO interface is the highest, which is about 2.5 times of ITC of ZrN-MgO interface and 3.8 times of ITC of HfN-MgO interface. The room temperature ITC of our epitaxial TiN-MgO interface is measured about 860 MW/m<sup>2</sup>K, which is higher than previous reported value 700 MW/m<sup>2</sup>K [3]. To make sure our result is correct and repeatable, we have repeated the experiment and data reduction at a different locations on our epitaxial TiN-MgO interface and found identical results to within the indicated measurement uncertainty; we would note that the original data of Ref. [3] was reported in 2003, and was in fact one of the first papers to ever use TDTR; as such, Ref. [3] predated the accurate mathematical formalism used for the data reduction (first reported in 2004[48]) as well as the two-tint method now used to prevent anomalous pump signals (first reported in 2008[47]). Given the challenging nature of the measurement, we believe either of these facts could explain the discrepancy between experimental results). ITC in these materials system also is found insensitive to dislocation densities consistent with previous literature[3] and our own work on silicides[81]. If phonon scattering at the interface was dominated by misfit dislocation density, then the ITC of ZrN-MgO or

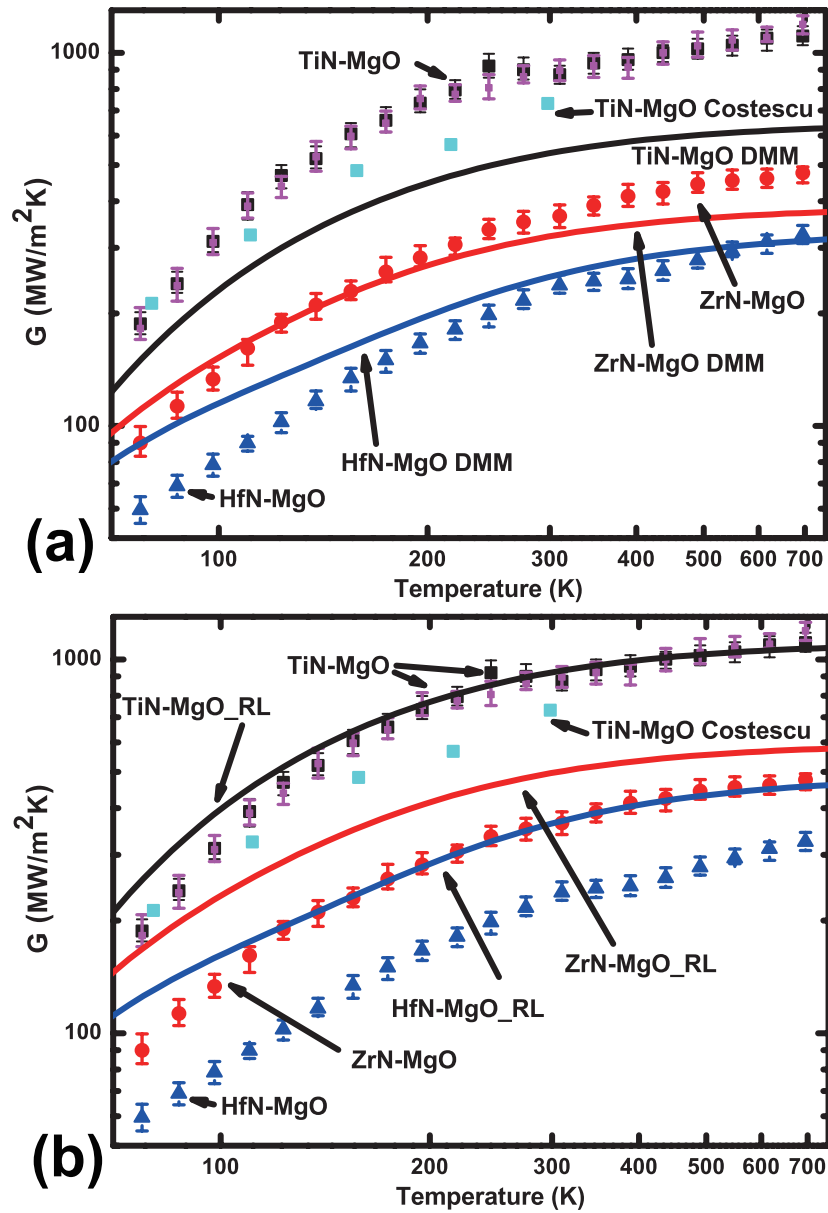


**Figure 5.5:** Comparison of Experiment and calculated ITC of group IV metal nitrides on MgO. TiN on MgO interface (black); ZrN on MgO interface (red); HfN on MgO interface (blue); remeasured TiN on MgO interface (magenta); TiN/MgO reported by Costescu[3] (cyan). (a) Symbols represents experimental data, line represents DMM calculated results; (b) Symbols represents experimental data, line represents elastic phonon radiation limit.

HfN-MgO might be expected to be lower than that of TiN-MgO since these have much larger lattice mismatch with MgO (9% vs 1%).

We’ve calculated the phonon dispersions for all material measured using DFPT as implemented in Quantum Espresso. The exchange correlation energy was approximated under the generalized gradient approximation (GGA) using the Perdew-Burke-Ernzerhof (PBE) functional form. Rappe-Rabe-Kaxiras-Joannopoulos (RRKJ) ultrasoft pseudopotentials from the PSLibrary were used with k-mesh and energy cutoffs chosen for appropriate convergence. Our phonon dispersion calculations compare favorably to previous DFPT calculations[108] including the appearance of soft phonon modes in ScN and phonon anomalies in the group IV metal nitrides. We use the phonon dispersions obtained to estimate the interface conductance in the DMM framework. It is found that the DMM significantly underestimates the experimentally observed results (by about 80 %); note, that Costescu’s previous theoretical results based on crude Debye theory *overestimated* results by about 300%); this shows clearly that use of full-dispersion DMM, as we do throughout this thesis, is required to correctly assess the DMM’s validity. In fact, we have calculated the upper limit for transport consistent with elastic transport, sometimes called the ‘radiation limit’ (see Section 2.2.4 for details), and we find that the ITC is so high that it appears to match or barely exceed the upper limit. To do so would imply that mechanisms other than elastic phonon-phonon transmission carry heat across the interface. MgO is a dielectric material, meaning that electrons cannot carry heat across the interface directly. However mechanisms such as inelastic phonon scattering or direct cross-interfacial electron-phonon coupling are potential explanations. Determining whether these mechanisms are reasonable will require further investigation involving rather challenging supercell DFPT including local electron-phonon coupling effects and anharmonic bond modeling as in our recent publication with collaborators[46].

A similar but much more extreme violation of the radiative limit is found when the same metals are grown on ScN. Figure 5.6 shows the measured temperature dependent of ITC of epitaxial TiN-ScN, ZrN-ScN and epitaxial HfN-ScN interfaces. Due

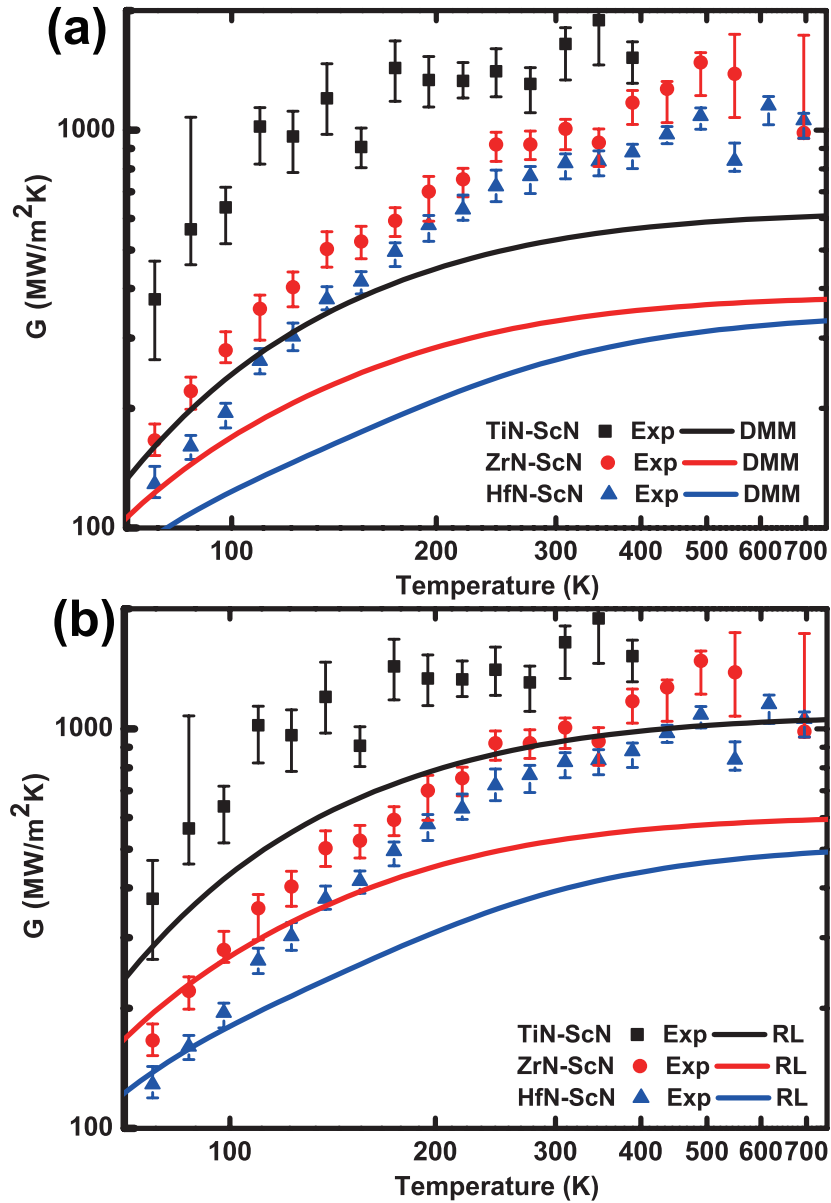


**Figure 5.6:** Comparison of Experiment and calculated ITC of group IV metal nitrides on ScN. TiN on ScN (black); ZrN on ScN interface (red); HfN on ScN interface (blue). (a) Symbols represents experimental data, line represents DMM calculated results; (b) Symbols represents experimental data, line represents elastic phonon radiation limit.

to the high conductance value and low thermal conductivity of ScN, the measured ITC of TiN-ScN is noisy and with relatively large error bar. The room temperature ITC of epitaxial TiN/ScN is measured about  $1.5 \text{ GW/m}^2\text{-K}$  with an asymmetric error ( $1.25 \text{ GW/m}^2\text{-K} < G(\text{TiN/ScN}) < 1.63 \text{ GW/m}^2\text{-K}$ ), which is extremely high value for metal-semiconductor interface but similar to the effective ITC  $1.2 \pm 0.12 \text{ GW/m}^2\text{-K}$  we extract from a TiN/(AlSc)N interface via the superlattices in Ref. [106]. In the nitride transducer-ScN interfaces, the experiment results are much higher than that DMM prediction, and also clearly higher than the elastic radiation limit. There are a few possible reasons account for the high value of ITC in group IV metal nitrides on ScN. First, the electronic portion of thermal conductivity in ScN is about  $3 \text{ to } 4 \text{ W/m-K}$ , [4] which could lead a considerable electron-electron coupling transportation across the interface. Though direct electron-electron transport is a possible explanation, we do not find it likely. Previous investigations of Al/Cu interfaces have found ITC of  $\approx 4 \text{ GW/m}^2\text{-K}$ , consistent with a diffuse mismatch model for electrons. However, in the current system the density of states in ScN is likely to be about 3 orders of magnitude smaller than in a pure metal like Cu or Al, meaning that electron transmission coefficients should be high. In principle, one could consider testing this theory by conducting through-plane electronic measurements of the electronic contact resistance (the ITC is related via the Weidemann-Franz law). However, if the ITC was indeed electronic in origin, it would imply a total electrical contact resistance of  $\sigma_c = G/(L_0T) \approx 136 \times 10^{12}/\Omega\text{-m}^2$ , making the measurement resistance less than  $1 \mu\Omega$  even for lithographically patterned test patches.

Note that due to similar crystal structure and chemical composition between group IV metal nitrides and ScN, the chemical bonding at the interface is expected to be stronger. It has been shown, both theoretically & experimentally, that weakly bonded interfaces can cause lower interface conductance[28, 29]. However, once the bonding is sufficiently strong, it is known that effect of bonding strength becomes unimportant[109]. The fact that TiN/MgO grows epitaxially indicates that there is at least some cross-interface bonding but the strength is currently unknown. Third,

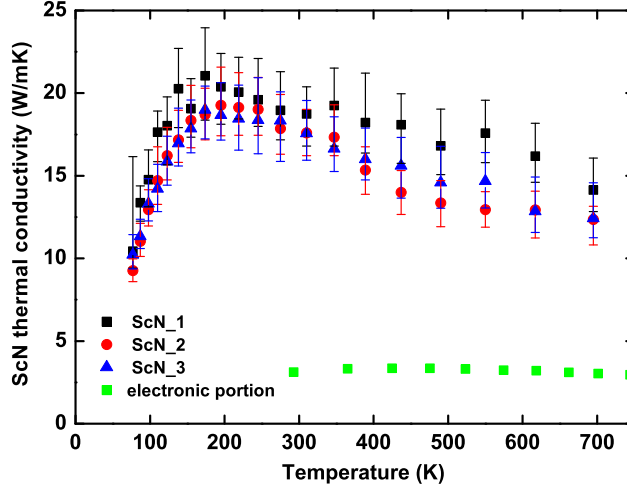


**Figure 5.7:** Temperature dependent thermal conductivity of ScN; black, red and blue respectively represent thermal conductivity measured under TiN, ZrN and HfN; green represents the electronic portion thermal conductivity calculated from reference[4]

other phonon transport mechanisms, like cross interface electron-phonon coupling and anharmonic phonon transport could lead the high interfacial thermal conductance. In general, the group IV transition metal nitrides do have higher *bulk* electron-phonon coupling constants than most pure metals, but it is not clear how or whether this carries over to near interfacial electron-phonon coupling.

The temperature dependent thermal conductivity of ScN(100) has not previously been reported. As it is one of the fitting parameters, we show it in Fig. 5.7. The thermal conductivity of ScN is  $\approx 10$  W/m-K at 77K. As the temperature increases, the thermal conductivity reaches a maximum value of  $\approx 20$  W/m-K at about 180K, then decrease to  $\approx 13$  W/m-K at 700K. The maximum value of ScN thermal conductivity (turning point) is at 180K, which is much higher than where it appears for most bulk single crystal Si (30K[110]), Ge(10K[110]) and GaAs(30K[111]). The reason for this is that for thin films boundary scattering remains dominant over a wider temperature

range[112]. In our case, a mean-free-path limitation of 450nm is imposed by the film thickness. At high temperature, the downward trend is caused by phonon-phonon scattering as usual.

## 5.4 Summary

The ITC of epitaxial group IV metal nitrides on MgO and on ScN interfaces are measured with TDTR and the experiment results are compared with DMM calculation as well as the radiation limit. By varying the Group IV metal, the mass of the metal's light atom was independently tuned, allowing the ability to tune the acoustic phonon frequencies in the metal without significant effect to optical phonon band structure. We find that the ITC of all the studied interfaces are quite high, significantly exceeding the DMM predictions, and in the case of XN-ScN interfaces even exceed the radiative limit for elastic phonon transport. The results imply that mechanisms such as anharmonic phonon transmission, strong cross-interfacial electron phonon coupling, or direct electric transmission are required to explain the transport. The TiN-ScN interface conductance is the highest room temperature metal-dielectric conductance ever reported. As future research it would be useful to use computation techniques, such as the ones developed for our earlier work on silicides [46], to determine whether either cross-interface electron-phonon coupling or anharmonicity are expected to exist at these interfaces.

## Chapter 6

### MULTIVALLEY III-V ALLOYS FOR IMPROVED THERMOELECTRICS

#### 6.1 Motivation

Thermoelectric (TE) devices are capable of directly converting the flow of heat to the flow of electricity and visa versa. As solid state devices, these heat engines have numerous advantages including long lifespan, high power densities, light weight, and in some cases superior cost[113, 114, 115]. While TE devices are at least a factor of 2 away from having competitive power generating efficiency and both improved device design and better materials properties will be critical for achieving higher performance TE devices. The efficiency of a given material to produce thermoelectric power is related to its dimensionless figure of merit  $ZT$ ,

$$ZT = \frac{\sigma \cdot S^2 \cdot T}{k_e + k_{ph}} \quad (6.1)$$

$\sigma$  is electrical conductivity,  $S$  is Seebeck coefficient,  $T$  is temperature,  $k_e$  and  $k_{ph}$  are respectively electronic and phonon portion of thermal conductivity. In order to achieve high efficiency  $ZT$ , we need materials with high  $\sigma$  and  $S$ , but low thermal conductivity  $k = k_e + k_{ph}$ . However, this is difficult to achieve in practice since these material parameters are interdependent in a complicated way.

In the framework of Boltzmann transport theory, the Seebeck coefficient can be derived in terms of the electronic band structure and electronic relaxation time as,[10]

$$S = \frac{\frac{e}{3T} \int v^2 \tau (E - E_f) \frac{\partial f_0}{\partial E} D(E) dE}{-\frac{e^2}{3} \int v^2 \tau \frac{\partial f_0}{\partial E} D(E) dE} \quad (6.2)$$

$e$  is charge of electron,  $v$  is group velocity of electrons,  $\tau$  is relaxation time,  $E_f$  is Fermi energy,  $E$  is single electron energy state,  $D(E)$  is density of states of electron with

energy  $E$ ,  $f_0$  is Fermi-Dirac distribution. Within the same framework, the electrical is found as

$$\sigma = e^2 \int v^2 \tau \frac{\partial f_0}{\partial E} D(E) dE \quad (6.3)$$

Note then that the denominator of equation 6.2 is proportional to the electrical conductivity. In fact, if the integrand of Eq. 6.3 is defined as the differential electrical conductivity, then the Seebeck coefficient can be seen to be the first moment of differential conductivity with respect to energy with a ‘centroid’ located at the chemical potential of the system. To obtain large Seebeck (i.e. large thermoelectric response in V/K), one would like to place the electronic carriers as far away from the chemical potential as possible to obtain a large moment. This favors lightly doped semiconductors for large Seebeck coefficient. However, if the chemical potential is very far from the chemical potential then very few carriers are actually excited, leading to low electrical conductivity. In the opposite extreme (a metal), there are many excited carriers, but there are almost as many above the chemical potential as below, so the moment is small and the Seebeck coefficient is low. As a tradeoff, optimal thermoelectric materials generally balance the need for simultaneously high  $\sigma$  and high Seebeck coefficient by using degenerately doped semiconductors. In other words, the doping is optimized to seek a maximum power factor defined as,

$$power\ factor = \sigma S^2 \quad (6.4)$$

The maximum power factor is essentially an intrinsic property of any given semiconductor and is dictated by the bandstructure. However, a survey of historically successful thermoelectric materials offers an important insight: thermoelectric materials with state-of-the-art performance typically have multiple bands with equivalent energy structure. This allows materials to boost the value of their Seebeck coefficient by raising the density of electron states, but without slowing down the electrons and sacrificing electrical conductivity. In traditional thermoelectric materials ( $\text{Bi}_2\text{Te}_3$ , [116])

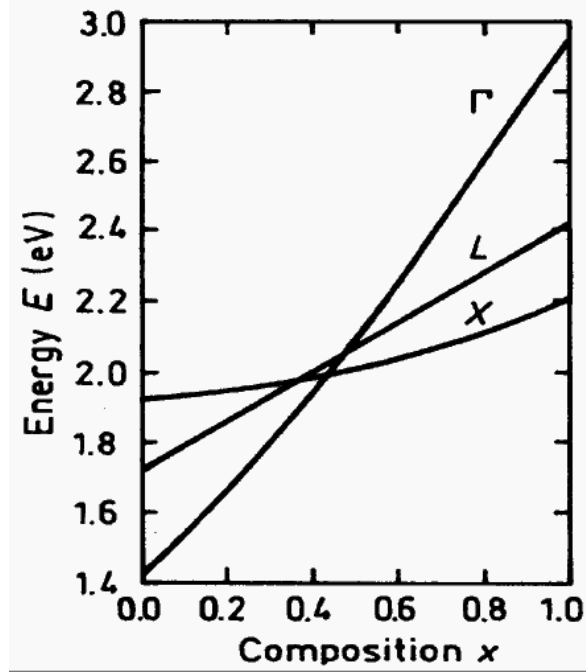


**Figure 6.1:** Energy separation between  $\Gamma$ -,  $X$ - and  $L$ - conduction band minima in  $\text{Al}_x\text{Ga}_{1-x}\text{As}$  with composition of  $x$ . Reprinted from Ref. [5]

$\text{PbTe}_{1-x}\text{Se}_x$ , [117]  $\text{Si}_{1-x}\text{Ge}_x$  [118]), this degeneracy exists naturally in the form of conduction band minima located at symmetrically equivalent faces of the Brillouin zone. In FCC materials, this is a 14-sided polygon that defines the allowable electron states.

The III-V semiconductors, with high saturation electron velocity and mobility, are widely studied for light emission devices [119, 120], solar cells [121, 122], quantum wells [123, 124] and quantum molecules [125, 125]. The goal of this chapter is to extend the idea of multi-valley conduction to III-V semiconductor materials such as  $\text{Al}_x\text{Ga}_{1-x}\text{As}$  by designing alloys which have both symmetry-required degeneracy and multiple types of bands with equal energy. The literature reported band structure of  $\text{Al}_x\text{Ga}_{1-x}\text{As}$  with composition are shown in Figure 6.1 [5]. The  $\Gamma$ -,  $X$ - and  $L$ - band minima in  $\text{Al}_x\text{Ga}_{1-x}\text{As}$  crossed at composition between  $x = 0.35$  to  $x = 0.47$ . In order to study the effects of band degeneration in  $\text{Al}_x\text{Ga}_{1-x}\text{As}$  on the thermoelectric properties, a collaborator (Prof. Zide, UD) help us prepare  $\text{Al}_x\text{Ga}_{1-x}\text{As}$  films with different

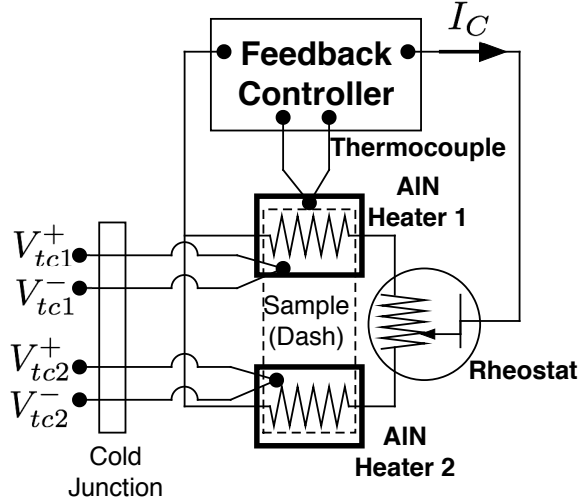


**Figure 6.2:** Circuit diagram and measurement schematic for the high temperature/vacuum integrated Seebeck measurement.

alloy compositions (from  $x = 0.30$  to  $x = 0.6$ ) while fixing the doping concentration in all the samples.

## 6.2 Experiment

### 6.2.1 Sample preparation

All  $\text{Al}_x\text{Ga}_{1-x}\text{As}$  samples in this chapter were prepared using a OSEMI NextGen molecular beam epitaxy (MBE) system by molecular beam epitaxy growth by the Zide lab.  $1\mu\text{m}$  thick  $\text{Al}_x\text{Ga}_{1-x}\text{As}$  films were grown on intrinsic GaAs wafers with a 50 nm GaAs buffer layer. Alloy composition  $x$  were controlled to be  $x = 0.30, 0.37, 0.45, 0.52, 0.60$ . Epitaxial  $\text{Al}_x\text{Ga}_{1-x}\text{As}$  films were doped n-type with Si concentrations of  $1 \times 10^{19} \text{ cm}^{-3}$ . A more detailed description of the growth conditions can be found elsewhere[126].

### 6.2.2 Seebeck coefficient stage designing and assembling

In order to perform high temperature thermoelectric measurements, a custom thermal stage was designed and built which was integrated into a MMR vacuum probe

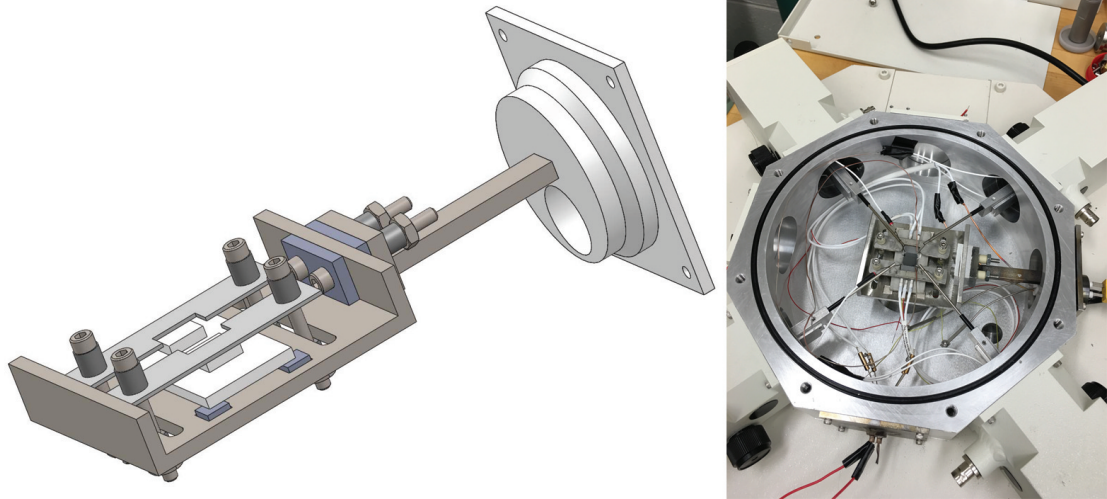


**Figure 6.3:** Left: 3D drawing of the Seebeck coefficient stage designed for the vacuum probe station; Right: The actual machined Seebeck coefficient stage assembled in the MMR vacuum chamber.

station in the Zide lab. The goal of the measurement platform is to create a small temperature gradient ( $\approx 1$  K/mm) across thin film samples ( $\approx 1$  cm square) while maintaining a fixed and controllable average sample temperature over the intermediate range between 300-700 K. The final design is shown in Fig. 6.2 uses two high heat flux resistive heaters (watlow, CER-1-01-00334) a larger base to generate the small temperature gradient for Seebeck coefficient measurement. The heaters are fixed on the stage by clamps and screws. All the joints are separated with machined Glass-Mica Ceramic Sheets for thermal insulating. One of the heaters has an embedded thermocouple which is feed to a feedback controller that adjusts the current until the correct temperature is achieved. To adjust the temperature gradient, a manually operated Rheostat divides the current between the two heaters until the desired gradient is achieved. In a typical Seebeck measurement, the temperature difference between heaters would be adjusted 5 times (2 above the base temperate, 2 above, and 1 with approximately zero difference). The 3D drawing and the actual machined Seebeck coefficient stage assembled in the MMR vacuum probe station are shown in Figure 6.3. The working temperature range

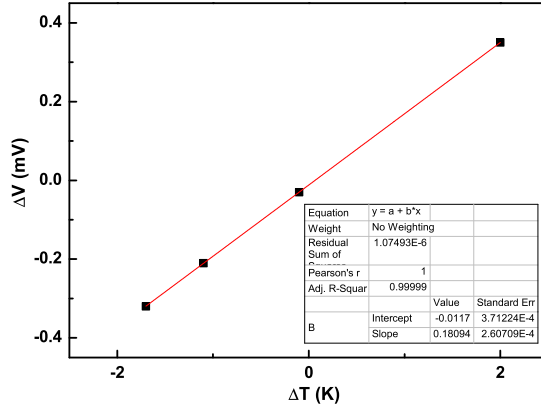


**Figure 6.4:** A typical Seebeck coefficient measurement data and fitting of the slope for  $\text{Al}_{0.52}\text{Ga}_{0.48}\text{As}$  at 350 K

of the final stage is from room temperature to 300 °C in vacuum.

### 6.2.3 TE properties characterization

Seebeck coefficient and electrical conductivity measurement of  $\text{Al}_x\text{Ga}_{1-x}\text{As}$  films were performed on the home-built Seebeck coefficient measurement stage. Before measurement, the samples were cut into square with size of 1 cm  $\times$  1 cm. Then photo-resist was manually brushed onto the sample surface to leave four corners with size of 1 mm  $\times$  1 mm exposed. After metallization, these corners served as electrodes for van der Pauw measurements. Samples with photoresist were baked at 100 °C for 3 minutes before putting into PVD chamber. Samples were coated with 400 nm silver, followed by ultrasonic cleaning of the photoresist in acetone. The sample temperature and the temperature difference were read with k-type thermocouple mounted on two of the electrodes at the sample surface. Silver paste was applied to mount the thermocouple to ensure good thermal and electrical contact. The voltage difference was read through a Keithley 2000 Multimeter, with resolution of  $0.1\mu\text{V}$ . The Seebeck coefficient was measured by linear regression of the  $\Delta V$  vs.  $\Delta T$  data (typically  $-2\text{K} \leq \Delta T \leq 2\text{K}$ ). Figure 6.4 shows a typical Seebeck coefficient measurement data and fitting of the slope

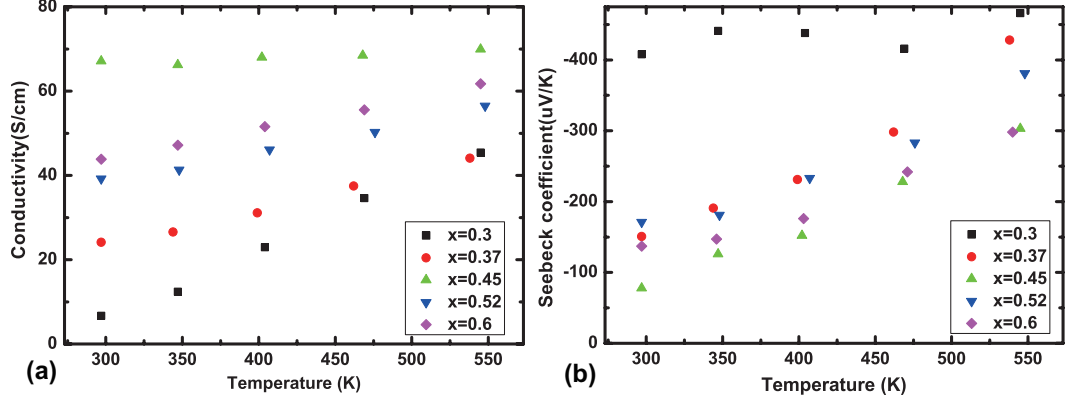


**Figure 6.5:** (a) The electrical conductivity of  $\text{Al}_x\text{Ga}_{1-x}\text{As}$  from room temperature to 300 °C for different alloy compositions; (b) The Seebeck coefficient of  $\text{Al}_x\text{Ga}_{1-x}\text{As}$  from room temperature to 300 °C for different alloy compositions

for  $\text{Al}_{0.52}\text{Ga}_{0.48}\text{As}$  at 350 K, and the slope indicates a Seebeck coefficient of 181  $\mu\text{V}/\text{K}$ . The electrical conductivity of the sample were measured with van der Pauw method. After Seebeck coefficient measurement, Hall effect measurements in the van der Pauw geometry were performed using an separate system in order to determine the electron carrier concentration and mobility. The Hall system allowed data collection from 50 K to 700 K, with resistivity, mobility, and carrier concentration being measured.

### 6.3 Results and discussion

The electrical conductivity and Seebeck coefficient are shown in Figure 6.5. As the Al content in the alloy increases, the electrical conductivity increase and is largest value at a composition  $x = 0.45$ , where the  $\Gamma$ -,  $X$ - and  $L$ - conduction band minima overlap. The highest electrical conductivity value in these samples are around 70 S/cm, which is still about one order of magnitude lower than that of a typical good thermoelectric material. However, the Seebeck coefficient of the sample with composition  $x = 0.45$  is actually the lowest. The Seebeck coefficient at  $x = 0.45$  is lowest among the compositions. This is unexpected since higher electronic density states effective mass at the multi-valley bands should lead higher Seebeck coefficient.

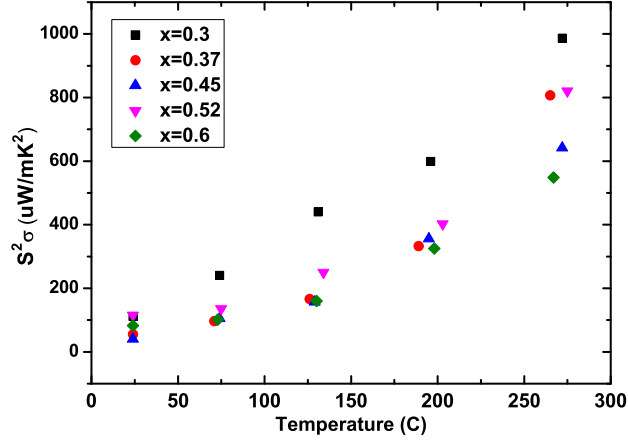


**Figure 6.6:** The power factor of  $\text{Al}_x\text{Ga}_{1-x}\text{As}$  from room temperature to 300 °C for different alloy compositions

The highest Seebeck coefficient, about 400  $\mu\text{V}/\text{K}$ , is achieved in composition  $x = 0.3$ . The Seebeck coefficient for different composition are found to be anti-correlated with the electrical conductivity.

As it is shown in Figure 6.6, the power factors for  $\text{Al}_x\text{Ga}_{1-x}\text{As}$  alloy increases with temperature, with a maximum output power factor of 1  $\text{mW}/\text{m}\cdot\text{K}^2$  (about a factor of 2 lower than for state-of-the-art thermoelectric based on PbTe). For different alloy compositions, the power factors are similar only except in composition  $x = 0.3$ . The power factor in  $x = 0.3$  sample is higher than other compositions due to its high Seebeck coefficient.

Figure 6.7 shows the electron concentration from 50 K to 700 K measured by wide temperature hall effect measurement. Surprisingly it is found that the electronic carrier concentrations in all the samples are less than  $10^{18} \text{ cm}^{-3}$ , and in some samples much less. Note that the Si dopants were controlled to have a fixed concentration of  $10^{19} \text{ cm}^{-3}$  in all samples. While literature based on Si:GaAs doping had suggested that doping efficiency would be  $\sim 8 : 1$  (i.e. 1 substitutional dopant per 8 Si atoms) in the high concentration limit, the addition of AIAs to the GaAs apparently reduces

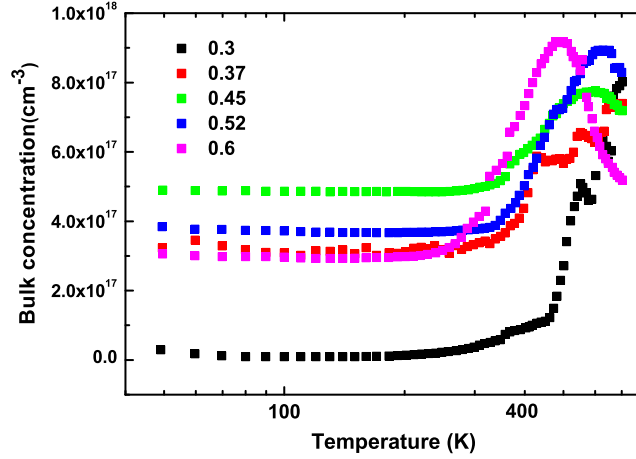


**Figure 6.7:** The bulk concentration of  $\text{Al}_x\text{Ga}_{1-x}\text{As}$  from 50 K temperature to 700 K for different alloy compositions measured by hall effect

the doping efficiency by at least an additional order of magnitude. This low doping efficiency is also reported and discussed by Chand[127] and Breiland[128]. The reason is due to a high activation energy of the donors. The doping is found to be sensitive to the Al content[128]. The unexpected low carrier concentrations in  $\text{Al}_x\text{Ga}_{1-x}\text{As}$  accounts for the low electrical conductivity and the low power factors found in thermoelectric measurement, despite the favorable multivalley band structure.

In Figure 6.7, three distinct regimes of activation are observed: (1) From 50 K-300 K, dopants show no change in thermal activation, indicating that some percentage of dopants are activated at very low temperature, but the majority are not active. The activated dopant levels in this regime are especially low in the case of direct band gap  $\text{Al}_{0.30}\text{Ga}_{0.70}\text{As}$  indicating that band degeneracy seems to improve the dopant activation. (2) From room temperature up to 550K, dopants undergo a round of thermal activation, increasing the carrier concentration by  $\sim 2$ -fold in most cases. (3) At higher temperatures, the carrier concentration begins to reduce, which could be a sign of a second activation which is detrimental to n-type doping; the mechanism is not fully understood, but could possibly originate from anti-site doping. Whatever the

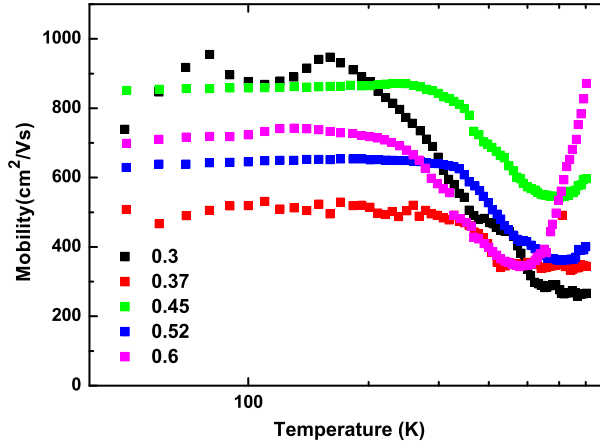


**Figure 6.8:** The electron mobility of  $\text{Al}_x\text{Ga}_{1-x}\text{As}$  from 50 K temperature to 700 K for different alloy compositions measured by Hall effect

mechanism, the end result is that the alloys cannot reach high enough doping levels using conventional doping mechanisms to exploit the multivalley band structure..

The electron mobility in  $\text{Al}_x\text{Ga}_{1-x}\text{As}$  vs. temperature is found with opposite trend to that of the electronic concentration. This suggest that the electron scattering mechanisms in these alloys are dominated by electron and electron scattering. The electron mobility measured in this project is found to be consistent with other experiments results[5, 128].

## 6.4 Summary

A Seebeck coefficient stage for vacuum probe measurements of thermoelectric properties was designed and used to characterize the thermoelectric properties of  $\text{Al}_x\text{Ga}_{1-x}\text{As}$  films. The Seebeck coefficient and power factor of  $\text{Al}_x\text{Ga}_{1-x}\text{As}$  alloy with degenerate bands were found not to exhibit extraordinary thermoelectric properties. Hall effect results suggest that this is because the carrier concentration is about one order of magnitude lower than that of the target donor concentration. Low doping efficiency caused by high doping activation energy in these samples prevents the testing

of the materials at activated carrier concentrations consistent with optimal thermoelectric power factor. One possible solution to the low doping efficiency could be using other donors with higher doping efficiency in  $\text{Al}_x\text{Ga}_{1-x}\text{As}$ .

## 6.5 Future work

In order to perform the electronic band engineering thermoelectrics project in a better way, much more emphasis should be given to controlling the carrier concentration or chemical potential, since our band convergence hypothesis was formulated assuming chemical potential is fixed. Since Si doping efficiency in  $\text{Al}_x\text{Ga}_{1-x}\text{As}$  is found to be low, both in this work or in literature. A better way to perform this research is using dopant with higher efficiency so that we can control the carrier concentration better. Potential dopants include Sn, Ge, Zn and Te. Sn and Te in particular are interesting candidates. Sn doping AlGaAs has been reported to achieve a carrier concentration as high as  $1 \times 10^{19} \text{ cm}^{-3}$ , [129], while Te is reported with highest doping concentration among the four [130]. However, Sn and Te are not elements that would typically be used in MBE of As-containing III-V materials and our chamber does not possess these elements.

Another way to advance this research might be to make short period superlattices of pure GaAs/AlAs that are spaced close enough together that their electrons wavefunctions overlap and create alloy-like band structure, but such that Al atoms would not directly be in contact with dopants. By using conventional doping in the GaAs layer if the digital alloys (i.e.  $n^{++}$ -GaAs/si-AlAs), we may be able to encourage chemical substitution of the Si atoms, yet still achieve the multiband structure.

## Chapter 7

### CREATION OF ION DEFECTS IN TRANSITION METAL FREE $K_2NiF_4$ STRUCTURE

#### 7.1 Motivation

Solid oxide fuel cells (SOFCs) are a promising alternative power generation source with an electrolyte that is a ceramic conductor of oxygen ions. Compared to proton exchange membrane fuel cells (PEMFCs) and alkaline fuel cells (AFCs), which are typically limited in the choice of operational fuel, SOFCs can make use of a wide variety of fuels including hydrogen, hydrocarbons, alcohols, and other alternatives[131, 132]. In order to achieve sufficiently high electrolyte conductivity, SOFCs are usually operated at temperatures of 800 C or above, which causes a number of issues including delicate gas sealing,[133] materials degradation,[134, 135] and slow start-up and shut-down. Therefore, new electrolytes with larger oxygen ion conductivity are required to reduce the operating temperature. Materials with the cubic fluorite crystal structure, such as doped zirconia and ceria, are the conventional electrolyte materials for SOFCs[136, 137, 138]. More recently, (La,Sr)(Ga,Mg)O<sub>3- $\delta$</sub>  (LSGM) with the perovskite structure has been developed as a solid electrolyte with high ionic conductivity,[139, 140, 141] and materials with more exotic crystal structures are being actively explored, too[142, 143, 144]. Oxide materials that adopt the  $K_2NiF_4$  crystal structure have been known for quite some time[145, 146]. Recently,  $La_2NiO_4$  and related compositions with this structure have received renewed attention for their potential application as the cathode material[147, 148] in a solid oxide fuel cell (SOFC). The materials exhibit mixed ionic and electronic conducting (MIEC) behavior with relatively large values for both forms of conductivity. Using mixed conductors as electrodes

in SOFCs enlarges the electrochemically active region from an essentially linear triple-phase boundary to the entire MIEC surface[149]. The crystal structure of  $\text{La}_2\text{NiO}_4$  is formed by alternatively stacking perovskite  $\text{LaNiO}_3$  layers (P-layer) and rocksalt  $\text{LaO}$  layers (R-layer)[150, 151]. Unlike most other oxygen ion conductors, hyperstoichiometric oxygen ions can be accommodated in the crystal. Mobile, interstitial oxygen ions reside in the R-layer[152, 153], and there is some evidence as well that oxygen vacancies can exist in the P-layer[8]. Recent reports[151, 154, 155, 156] have ascribed the existence of interstitial oxygen ions to tensile stresses in the R-layers arising from equilibration of the lattice parameters of the R-layers and P-layers. The oxygen ion conductivity of  $\text{La}_2\text{NiO}_4$  was determined by Bassat, et al.[152] and Shaula, et al.[157] using oxygen isotope exchange and found to be at least comparable to that of conventional YSZ[158, 159]. Nevertheless,  $\text{La}_2\text{NiO}_4$  is mainly a p-type hole conductor, and exhibits a semiconductor-metal transition at a temperature between 250 °C and 450 °C. Electron/hole conduction in these materials is strongly correlated to the presence of the transition metal in the B-site,[160, 161] typically Ni but often substituted with Fe, Cu, or Co[162]. Here, new oxide compositions with the  $\text{K}_2\text{NiF}_4$  crystal structure are reported. The B-site cation in  $\text{La}_2\text{NiO}_4$  has been replaced with the non-transition metal elements Mg and Al in attempt to obtain an oxide electrolyte with ion transference number close to unity. This notion was previously attempted using a base composition of  $\text{LaSrAlO}_4$ [163]. Unfortunately, that effort was unsuccessful, as the authors showed that the crystal structure was not stable to oxygen defect formation when the La/Sr ratio was altered. This is believed to be because the net charge balance of the R-layer and P-layer in  $\text{LaSrAlO}_4$  (assuming complete randomization on the A-site) is +0.5 and -0.5, respectively, as compared to the +1 and -1, respectively, found in  $\text{La}_2\text{NiO}_4$ . Coulombic interaction between the oxygen defects and the surrounding lattice may thus be important in stabilizing the crystal structure against stoichiometry.

In this work, compositions in the  $\text{La}_{2-a}\text{Ni}_{1-x}\text{Mg}_x\text{O}_4$  series,  $\text{La}_{2-y}\text{Sr}_y\text{Ni}_{1-x}\text{Mg}_x\text{O}_4$  series, and  $\text{La}_{2-y}\text{Sr}_y\text{Al}_y\text{Ni}_{1-x}\text{Mg}_{x-y}\text{O}_4$  series are presented. The compositions are defined so that x always represents the amount of Ni removed from the baseline  $\text{La}_2\text{NiO}_4$

composition (i.e.,  $x = 1$  represents complete removal of Ni). The main goals were to have as little Ni and as much charge separation in the R-layer and P-layer as possible while maintaining the  $\text{K}_2\text{NiF}_4$  crystal structure. The electrical conductivity of a few promising compounds were investigated to determine the influence of decreasing Ni content as well as the possibilities for obtaining an oxide electrolyte from this crystal structure. First, Transition-metal-free  $\text{K}_2\text{NiF}_4$  structure materials with composition  $\text{La}_{1.6}\text{Sr}_{0.4}\text{Al}_{0.4}\text{Mg}_{0.6}\text{O}_4$  (LSAM) were synthesized and shown to have significantly reduced electron conductivity (this part is also published on [164]). Then, Ca, Ga, or Zn substitute for Sr, Al, or Mg, respectively, in LSAM and the effects of these substitutions on phase stability and conductivity are studied (this part is also published on [165]). Ca substitution is chosen because its smaller ionic radius is known to increase the concentration of oxygen interstitials in  $\text{La}_2\text{NiO}_4$ [156]. Ga is selected to replace Al based on the previous success of high oxygen ion conductivity in the related perovskite LSGM. Zn is examined in the interest of increasing the cell volume to promote ion mobility[166]. Of specific interest is whether these substitutions are able to increase oxygen defect mobility and/or increase available defect concentrations by allowing increased P-layer/R-layer charge separation with nominal compositions beyond  $(\text{A}_{1.6}^{3+}\text{A}_{0.4}^{2+})(\text{B}_{0.4}^{3+}\text{B}_{0.6}^{2+})\text{O}_4$ .

## 7.2 Experiments

### 7.2.1 Synthesis and structural characterization

$\text{K}_2\text{NiF}_4$  structure oxides with different compositions were all prepared by solid state reaction. Reagents of synthesized starting from powders of  $\text{La}_2\text{O}_3$  (99.999%, Inframat Advanced Materials),  $\text{SrCO}_3$  (99.5+%, Inframat Advanced Materials),  $\text{Mg}(\text{OH})_2$  (98.4%, Alfa Aesar),  $\text{Al}_2\text{O}_3$  (99.5% metals basis, Alfa Aesar),  $\text{Ga}_2\text{O}_3$  (99.99% metals basis, Alfa Aesar),  $\text{ZnO}$  (99.9% metals basis, Alfa Aesar) and  $\text{CaCO}_3$  (99.5% metals basis, Alfa Aesar) were used as the starting raw materials. These reagents were weighed stoichiometrically and then ball milled using spherical YSZ milling media for 20 hours in deionized water. The grinding media were removed from

the mixed reagents, and then rinsed with DI water for 5 min in an ultrasonic bath 5 times, after which the rinse water was visually clean. All of the rinsed water was collected and heated with the milled dispersion on a hotplate to reduce the loss of chemicals. Finally, the dried precursors were milled in agate mortar and calcined at 1350 °C for 5 hours with equal heating and cooling rates of 100 °C/h. The as-synthesized materials were structurally characterized in conventional  $\theta$ -2 $\theta$  geometry on a PANalytical XPert X-ray diffractometer (XRD) using Cu-K $\alpha$  radiation. The lattice parameters were determined from XRD patterns using Jade software (ver. 5.0, Materials Data, Inc). Calcined powders were uniaxially pressed without binder at a pressure of 300 MPa and then sintered at 1450 °C for 10 h with equal heating and cooling rate of 100 °C/h to obtain pellets with density > 95%. The densities of the pellets were determined by Archimedes method to be > 96%. The pellets were polished into desired shape (12mm  $\times$  5mm  $\times$  1mm) by hand. The microstructures of the sintered pellets were characterized by scanning electron microscopy (SEM, JOEL JSM-7400F) with a 3 keV accelerating voltage. Imaged surfaces were polished to 800-grit, thermally etched in air at 1150 °C for 6 h, and then coated with roughly 10 nm of gold/palladium (60% Au, 40% Pd).

### 7.2.2 Conductivity measurement

The sintered pellets were polished by hand into rectangular shape with dimension 12 mm $\times$ 5 mm $\times$ 1 mm. Four silver paint electrodes were applied along the length of the sample for four-probe DC conductivity measurement. Electrical measurements were collected using a Keithley 2601A Sourcemeter linearly sweeping voltages between -1 V and +1 V. This relatively wide voltage range was used to reduce noise in the current signal despite high sample resistances. The linearity of the current-voltage relationship over the entire range suggested that no oxidization or reduction of the materials under test occurred. Temperature was controlled between 300 °C and 660 °C in a tube furnace and directly measured with a thermocouple in close proximity to the sample. Flowing dry air and commercial Ar/O<sub>2</sub> mixtures were used to change the

oxygen partial pressure. Errors in the conductivity data mostly come from imprecision in the geometry of the sample.

### 7.3 Results and discussions

Powders with nominal composition  $\text{La}_2\text{Ni}_{1-x}\text{Mg}_x\text{O}_4$  ( $x = 0, 0.1, 0.2, 0.3, 0.4,$  and  $0.5$ ) were all black in color. Their x-ray diffraction (XRD) patterns are shown in Figure 7.1(a). As expected for the  $x = 0$  sample, pure  $\text{K}_2\text{NiF}_4$  phase is obtained, and the powders are well crystallized. The same is found for samples with  $x = 0.1, 0.2,$  and  $0.3,$  with no impurity peaks observed. However, upon decreasing the amount of Ni to  $0.6,$  second phase peaks of  $\text{La}_2\text{O}_3$  appear. Interestingly, no corresponding peaks of MgO appear. Decreasing the amount of Ni further to  $0.5$  causes the impurity peaks of  $\text{La}_2\text{O}_3$  to become larger with still no MgO (or other Mg-containing phase) impurity peaks. The destination of the Mg is unclear in these samples.  $\text{La}_{1.85}\text{Ni}_{1-x}\text{Mg}_x\text{O}_4$  series powders with A-site deficiency were also prepared. As Figure 7.1(b) shows,  $\text{La}_2\text{O}_3$  impurity peaks appear when the amount of Ni is below  $0.6,$  similar to  $\text{La}_2\text{Ni}_{1-x}\text{Mg}_x\text{O}_4$  series. Thus, A-site deficient samples have little effect on stabilizing the crystal structure towards reduced amount of Ni.

In order to reduce the Ni content further, Sr doping was used. Sr doping on the A-site of  $\text{La}_2\text{NiO}_4$  is known to affect the lattice parameters due to the larger ionic radius of  $\text{Sr}^{2+}$  relative to  $\text{La}^{3+}$ [156]. According to Ganguli, the ratio of ionic radii between the 9-fold coordinated A-site cation and the 6-fold coordinated B-site cation,  $r_A(IX)/r_B(VI),$  should be between about  $1.7$  and  $2.4$  in order to stabilize the  $\text{K}_2\text{NiF}_4$  phase[167]. Since the radius of  $\text{Mg}^{2+}$  is larger than both  $\text{Ni}^{2+}$  and  $\text{Ni}^{3+},$  a larger average A-site radius should provide a more stable configuration. Nevertheless, in order to maintain maximal charge separation between the R-plane and P-plane, a minimal amount of Sr doping is desired. Figure 7.2 shows X-ray diffraction patterns for the  $\text{La}_{2-y}\text{Sr}_y\text{Ni}_{1-x}\text{Mg}_x\text{O}_4$  series of samples. As can be seen,  $\text{La}_{1.8}\text{Sr}_{0.2}\text{NiO}_4$  is phase pure, with no significant second phase apparent. A peak marked with a circle indicates that moderate  $\text{Sr}^{2+}$  doping leads the crystal structure to change from tetragonal to a

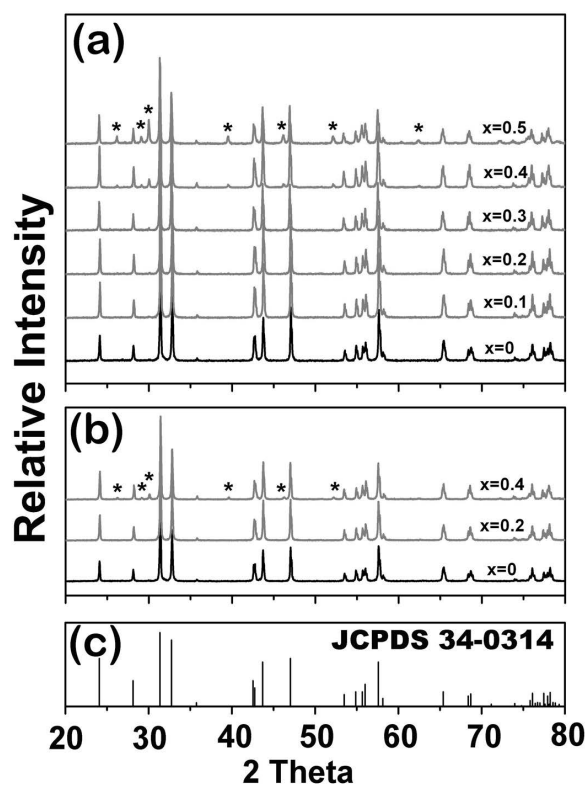


**Figure 7.1:** X-ray diffraction patterns of (a)  $\text{La}_2\text{Ni}_{1-x}\text{Mg}_x\text{O}_4$  and (b)  $\text{La}_{1.85}\text{Ni}_{1-x}\text{Mg}_x\text{O}_4$  series powders after calcination. (c) JCPDS card #34-0314 refers to tetragonal  $\text{La}_2\text{NiO}_4$ . Peaks marked with an \* are indicative of  $\text{La}_2\text{O}_3$  phase.

highly similar orthorhombic, with the (103) and (031) peaks split. JCPDS cards #87-0222, #87-0223 and #87-0224, which are all samples of Sr<sup>2+</sup> doped La<sub>2</sub>NiO<sub>4</sub>, indicate similar behavior. With 10% Sr doping on the A-site, i.e. La<sub>1.8</sub>Sr<sub>0.2</sub>Ni<sub>1-x</sub>Mg<sub>x</sub>O<sub>4</sub>, 50% Ni can be replaced with Mg before secondary La<sub>2</sub>O<sub>3</sub> phase is found. That number increases to 60% replacement for 25% Sr doping (La<sub>1.5</sub>Sr<sub>0.5</sub>Ni<sub>1-x</sub>Mg<sub>x</sub>O<sub>4</sub>). Still, reducing the Ni content to 40% leads to a sample that is black in color, which along with electrical conductivity measurements gives strong indication that the sample maintains significant electron/hole conduction.

In order to decrease the Ni content further, Al is introduced into the system. Al is believed to stabilize the K<sub>2</sub>NiF<sub>4</sub> crystal structure due to its smaller ionic radius and ability to provide charge balance for Sr doping on the A-site. Figure 7.3 shows x-ray diffraction patterns for samples with La<sub>2-y</sub>Sr<sub>y</sub>Al<sub>y</sub>Ni<sub>1-x</sub>Mg<sub>x-y</sub>O<sub>4</sub> compositions. As opposed to the previous compositional series, both low and high amounts of Mg can lead to secondary phase formation in this series. Samples with low Mg content indicate the formation of LaAlO<sub>3</sub> as a second phase, which disappeared with Mg content greater than about 50%. This effect may be caused by increasing Mg, with large ionic radius, reducing the lattice strain caused by the inclusion of the rather small Al. Samples with high Mg content cause formation of La<sub>2</sub>O<sub>3</sub> second phase until the equal amounts of Sr and Al reach 0.4. The composition La<sub>1.6</sub>Sr<sub>0.4</sub>Al<sub>0.4</sub>Mg<sub>0.6</sub>O<sub>4</sub> appears to have the smallest amount of Sr and Al that allows complete removal of transition metals from the B-site. At this level of Sr and Al doping, as Mg replaces Ni such that the Ni concentration is 0.2, 0.1, and 0, the color of the powders changes from black, to dark green and then pale yellow. This color change indicates the removal of free electronic carriers.

To summarize the above results, Figure 7.4 indicates in a quasi-ternary phase diagram the largest amount of Ni could be removed while maintaining the K<sub>2</sub>NiF<sub>4</sub> crystal structure. Generally speaking, directly replacing Ni with Mg in the baseline La<sub>2</sub>NiO<sub>4</sub> composition can only be accomplished up to about 30%. The addition of Sr and, even more so, equal amounts of Sr and Al rapidly increases the amount of Ni that can be removed.

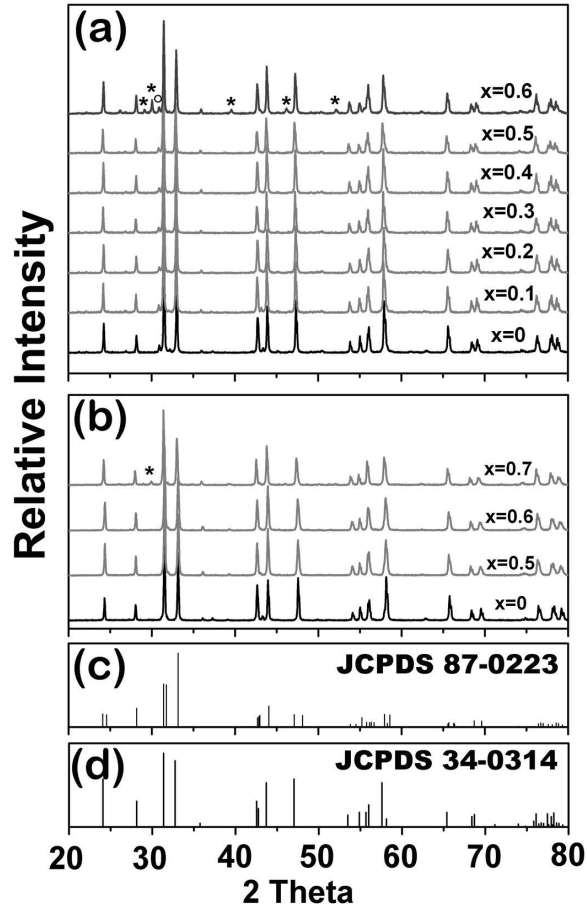


**Figure 7.2:** X-ray diffraction patterns of  $\text{La}_{2-y}\text{Sr}_y\text{Ni}_{1-x}\text{Mg}_x\text{O}_4$  series powders after calcination, with (a)  $y=0.2$  and (b)  $y=0.5$ . (c) JCPDS card #87-0223 refers to  $(\text{La}_{1.75}\text{Sr}_{0.25})(\text{NiO}_{2.212})$ . (d) JCPDS card #34-0314 refers to tetragonal  $\text{La}_2\text{NiO}_4$ . Peaks marked with an asterisk are indicative of  $\text{La}_2\text{O}_3$  phase; peaks marked with a circle are indicative of an orthorhombic  $\text{La}_2\text{NiO}_4$  phase.

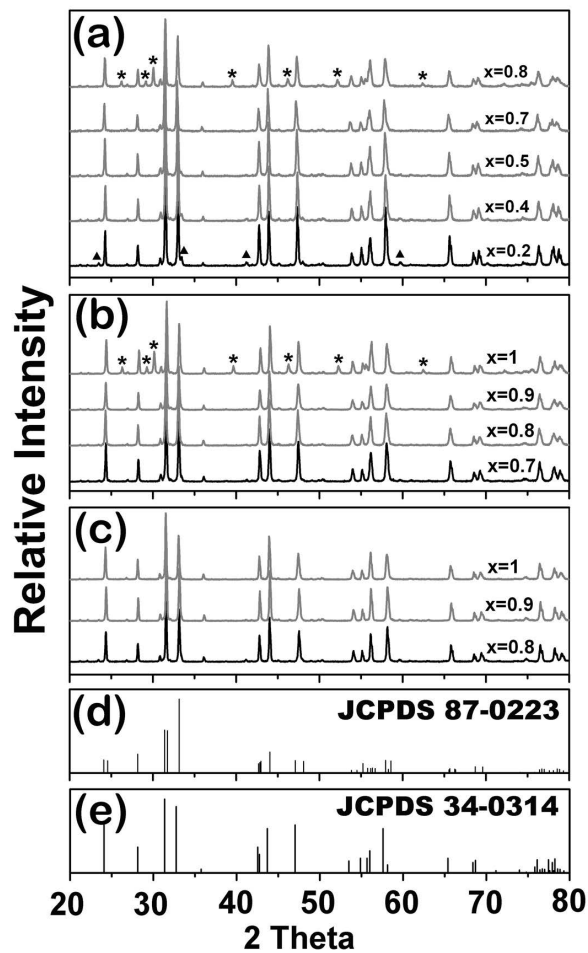


**Figure 7.3:** X-ray diffraction patterns of  $\text{La}_{2-y}\text{Sr}_y\text{Al}_x\text{Ni}_{1-x}\text{Mg}_{x-y}\text{O}_4$  series powders after calcination, with (a)  $y=0.2$ ; (b)  $y=0.3$ ; (c)  $y=0.4$ . (d) JCPDS card #87-0223 refers to  $(\text{La}_{1.75}\text{Sr}_{0.25})(\text{NiO}_{2.212})$ . (e) JCPDS card #34-0314 refers to  $\text{La}_2\text{NiO}_4$ . Peaks marked with \* are indicative of  $\text{La}_2\text{O}_3$  phase; peaks marked with a triangle are indicative of  $\text{LaAlO}_3$ .

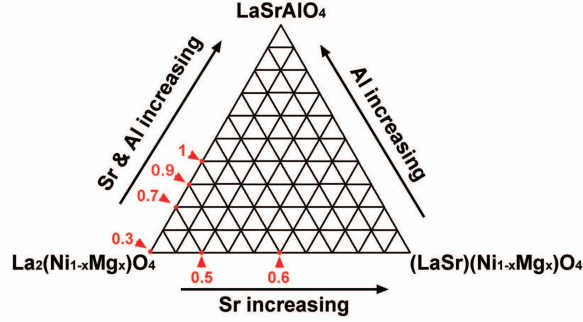


**Figure 7.4:** Quasi-ternary  $\text{K}_2\text{NiF}_4$  phase diagram indicating the largest amount Ni that can be replaced while maintaining the  $\text{K}_2\text{NiF}_4$  crystal structure.

In order to create nonstoichiometric oxygen interstitials or vacancies, the La/Sr ratio was then changed from the baseline  $\text{La}_{1.6}\text{Sr}_{0.4}\text{Al}_{0.4}\text{Mg}_{0.6}\text{O}_4$  base composition. XRD results are shown in Figure 7.5. The crystal structure remains stable as the La/Sr ratio is decreased to  $\text{La}_{1.5}\text{Sr}_{0.5}\text{Al}_{0.4}\text{Mg}_{0.6}\text{O}_{3.95}$ . Decreasing the La/Sr ratio further caused the appearance of peaks from an unidentified impurity phase. When increasing the La/Sr ratio, compositions up to  $\text{La}_{1.65}\text{Sr}_{0.35}\text{Al}_{0.4}\text{Mg}_{0.6}\text{O}_{4.025}$  were achieved before second phase peaks appeared. Further increases in the La/Sr ratio caused the appearance of peaks indicating the  $\text{La}_4\text{Al}_2\text{MgO}_{10}$  phase.

The total electrical conductivity of  $\text{La}_{1.6}\text{Sr}_{0.4}\text{Al}_{0.4}\text{Ni}_{1-x}\text{Mg}_{x-0.4}\text{O}_4$  decreases as Ni is removed from the  $\text{K}_2\text{NiF}_4$  lattice. As shown in Figure 7.6(a), the conductivities of the synthesized samples indicate thermally activated conduction with a single activation energy over the entire temperature range of the measurement. This result is different from that of  $\text{La}_2\text{NiO}_4$ , which exhibits a semiconductor-metal transition[7], but is consistent with reported results for  $\text{LaSrAlO}_4$ [163]. The semiconductor-metal transition thus seems to be closely related to the presence of the transition metal at concentrations above at least 20%. The activation energy increases as Ni is removed from the crystal.

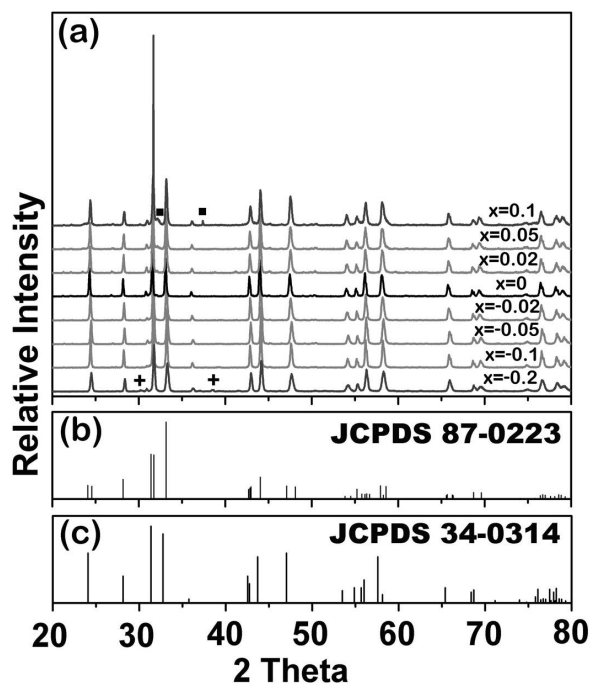


**Figure 7.5:** (a) X-ray diffraction patterns of  $\text{La}_{1.6+x}\text{Sr}_{0.4-x}\text{Al}_{0.4}\text{Mg}_{0.6}\text{O}_{4+x/2}$  series powders after calcinations; (b) JCPDS card #87-0223 refers to  $(\text{La}_{1.75}\text{Sr}_{0.25})(\text{NiO}_{2.212})$ . (c) JCPDS card #34-0314 refers to  $\text{La}_2\text{NiO}_4$ . Peaks marked with a square are indicative of  $\text{La}_4\text{Al}_2\text{MgO}_{10}$  phase; peaks marked with a cross are indicative of an unidentified impurity phase.

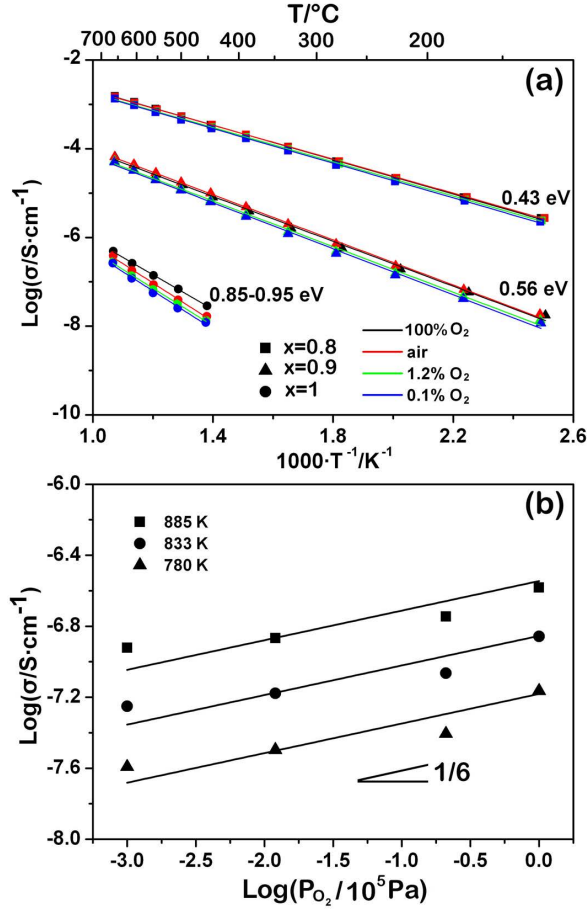


**Figure 7.6:** (a) Arrhenius plots of the total electrical conductivities of  $\text{La}_{1.6}\text{Sr}_{0.4}\text{Al}_{0.4}\text{Ni}_{1-x}\text{Mg}_{x-0.4}\text{O}_4$  samples, showing values for compositions with  $x = 0.8, 0.9,$  and  $1$ . Measurements made in differing oxygen partial pressures are indicated by color, though these values overlap strongly for the  $x = 0.8$  and  $0.9$  compositions. The activation energies of the conductivity-temperature product are listed next to each sample (as detailed in the text, the activation energy increased with decreasing oxygen partial pressure for the  $x = 1$  sample). (b) Total electrical conductivity of  $\text{La}_{1.6}\text{Sr}_{0.4}\text{Al}_{0.4}\text{Mg}_{0.6}\text{O}_4$  vs. oxygen partial pressure at the three temperatures indicated. In both (a) and (b), error bars are smaller than the data points.

When  $x = 1$ , the activation energy decreases as oxygen partial pressure increases, from 0.95 eV in 0.1% O<sub>2</sub> to 0.85 eV in 100 % O<sub>2</sub>. Though the data is over a limited oxygen partial pressure range, the dependence of the electrical conductivity on the oxygen partial pressure suggests that either  $\sigma \propto P_{O_2}^{1/6}$  or, alternatively, constant conductivity at low oxygen partial pressure rising to  $\sigma \propto P_{O_2}^{1/4}$  at high oxygen partial pressure. This relationship should be related to the oxygen nonstoichiometry value  $\delta$ . In La<sub>2</sub>NiO<sub>4</sub>,  $P_{O_2}^{1/6}$  dependence has been reported for oxygen non-stoichiometry,  $\delta$  [168], as well as the total conductivity [169] and the oxygen ion conductivity specifically [170].

A  $P_{O_2}^{1/6}$  dependence would indicate that the number of intrinsic carriers is low and that, as in La<sub>2</sub>NiO<sub>4</sub>, most of the carriers in La<sub>1.6</sub>Sr<sub>0.4</sub>Al<sub>0.4</sub>Mg<sub>0.6</sub>O<sub>4</sub> are created by an oxidation process:



where  $V_i^X$  represents empty interstitial sites,  $O_i''$  represents oxygen interstitials, and  $h^\bullet$  represents holes. Both the oxygen interstitials and holes are proportional to  $\delta$  as derived from a mass action law for the oxidation process

$$K_O = \frac{[O_i''] \cdot p^2}{P_{O_2}^{1/2}} \quad (7.2)$$

where  $p$  represents the hole concentration. Since the predominant source of the interstitial oxygen ions and holes is the oxidation reaction,  $2[O_i''] \approx p$ , and thus

$$2[O_i''] = p = \sqrt[3]{2K_O} \cdot (P_{O_2})^{1/6} \quad (7.3)$$

If this is the correct mechanism to explain the conductivity results, it is not clear yet whether the mobile defect responsible for the measured conductivity in these samples is holes or oxygen interstitials, but the larger activation energies measured here for La<sub>1.6</sub>Sr<sub>0.4</sub>Al<sub>0.4</sub>Mg<sub>0.6</sub>O<sub>4</sub> are near reported values for oxygen ion diffusivity in La<sub>2</sub>NiO<sub>4</sub> [170]. An alternative mechanism to explain these conductivity results suggests high

intrinsic ionic carrier density due to Frenkel disorder on the anion sublattice. The Frenkel pair formation reaction is



where  $O_O^X$  represents an oxygen on the oxygen site and  $V_O^\cdot$  represents an oxygen vacancy. The mass action law for this reaction is

$$K_{Fr} = \frac{[O_i''] \cdot [V_O^\cdot]}{[V_i^X] \cdot [O_O^X]} \quad (7.5)$$

where  $[V_i^X]$  and  $[O_O^X]$  are essentially constant. If  $K_{Fr}$  is large, this reaction is the predominant source of oxygen interstitials and oxygen vacancies at intermediate oxygen partial pressures. From this, the estimate can be made  $[O_i''] \approx [V_O^\cdot] = \sqrt{K_{Fr}[V_i^X][O_O^X]}$ . Combined with formula 7.2,

$$p = \frac{\sqrt{K_O}}{\sqrt[4]{K_{Fr}[V_i^X][O_O^X]}} \cdot P_{O_2}^{1/6} \quad (7.6)$$

If this is the correct mechanism to explain the conductivity results, then the data plotted in Figure 7.6(b) exhibits a transition between predominantly ionic conductivity at lower oxygen partial pressures and predominantly hole conductivity at higher oxygen partial pressures. At low  $P_{O_2}$ , the conductivity is nearly constant as the ionic defect concentration is fixed; at high  $P_{O_2}$ , the conductivity is proportional to the hole concentration, increasing as  $P_{O_2}^{1/4}$ . While some evidence for this change in slope can be found in Figure 7.6(b), it is not possible to make a strong claim based on the data collected so far.

For samples with  $x = 0.8$  and  $0.9$ , the conductivities are less influenced by oxygen partial pressure. This result is unexpected, since transition metals like Ni tend to easily change valence states. Given the reduction in conductivity with reduced Ni content and the low activation energies of conduction, the mobile carriers are more likely to be predominantly electronic and not ionic. It is possible that the redox reaction was

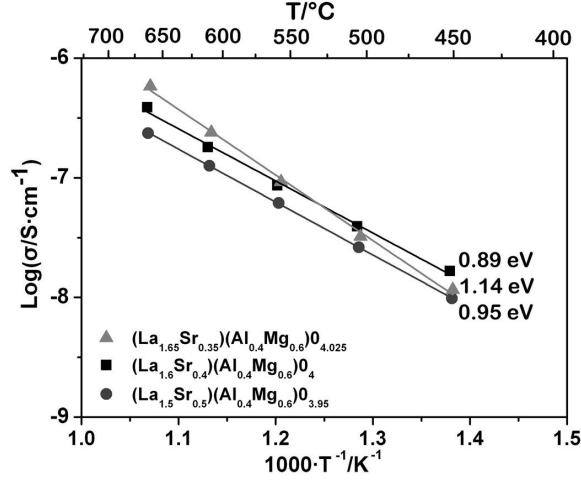


**Figure 7.7:** Arrhenius plot of total electrical conductivity of stoichiometric and non-stoichiometric samples measured in air. Error bars are smaller than the data points.

kinetically limited in these two samples, and the conductivity values do not represent equilibrium conditions.

The electrical conductivities of the  $\text{La}_{1.6+x}\text{Sr}_{0.4-x}\text{Al}_{0.4}\text{Mg}_{0.6}\text{O}_{4+x/2}$  compositions with nonstoichiometric oxygen interstitials and vacancies are shown in Figure 7.7. There is a small but clear change in activation energy between the three compositions, though the conductivity is never much increased relative to that of the stoichiometric compound. This result indicates that neither oxygen vacancies nor interstitials are sufficiently mobile to provide reasonable conductivity at the carrier concentrations available near this baseline composition.

The maximum possible ionic defect mobilities in  $\text{La}_{1.65}\text{Sr}_{0.35}\text{Al}_{0.4}\text{Mg}_{0.6}\text{O}_{4.025}$  and  $\text{La}_{1.5}\text{Sr}_{0.5}\text{Al}_{0.4}\text{Mg}_{0.6}\text{O}_{3.9}$  can be calculated based on the defect concentrations and the measured conductivity. The conductivity from doubly-charged ionic defects is related to the mobility by:

$$\sigma = 2e\mu C \quad (7.7)$$

where  $\mu$  is the mobility,  $C$  is the concentration, and  $e$  is the elementary charge. Since

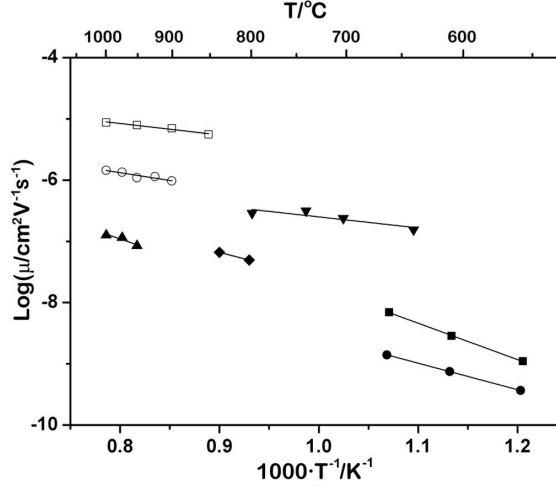


**Figure 7.8:** Comparison of defect mobilities from literature with the maximum possible mobility (as discussed in the text) in the materials measured here. Maximum defect mobility in  $\blacksquare$   $\text{La}_{1.65}\text{Sr}_{0.35}\text{Al}_{0.4}\text{Mg}_{0.6}\text{O}_{4.025}$  and  $\bullet$   $\text{La}_{1.5}\text{Sr}_{0.5}\text{Al}_{0.4}\text{Mg}_{0.6}\text{O}_{3.9}$ ; mobility calculated from reported diffusivity of  $\square$   $\text{La}_2\text{NiO}_{4+\delta}$  [6],  $\circ$   $\text{La}_{1.9}\text{Sr}_{0.1}\text{NiO}_{4+\delta}$  [7],  $\blacktriangle$   $\text{La}_{1.8}\text{Sr}_{0.2}\text{NiO}_{4+\delta}$  [7],  $\blacktriangledown$   $\text{La}_{1.9}\text{Sr}_{0.1}\text{NiO}_{4+\delta}$  [7] and  $\blacklozenge$   $\text{La}_{1.8}\text{Sr}_{0.2}\text{NiO}_{4+\delta}$  [8]. Error bars are smaller than the data points.

the identity of the charge carrier is unclear in these compositions, the use of this model calculates the maximum possible mobility of ionic defects; if the carriers are in fact electronic, then the mobility of background ionic defects must be even less than the value so calculated. In Figure 7.8, the maximum defect mobilities measured here are compared with the oxygen ion  $T$  mobility as calculated from reported oxygen self-diffusivity in  $\text{La}_{2-x}\text{Sr}_x\text{NiO}_{4+\delta}$  [171, 6]. The oxygen mobility is calculated from the diffusivity  $D$  using the Einstein relation:

$$D = \frac{\mu k_B T}{2e} \quad (7.8)$$

where  $k_B$  is Boltzmann's constant and  $T$  is the absolute temperature. As shown in Figure 7.8, the mobility in  $\text{La}_{2-x}\text{Sr}_x\text{NiO}_{4+\delta}$  decreases by about one order of magnitude when the amount of Sr increases from  $x = 0$  to 0.1 and again as it increases to 0.2. Therefore, low mobility in our samples with  $x \approx 0.4$  is not surprising.

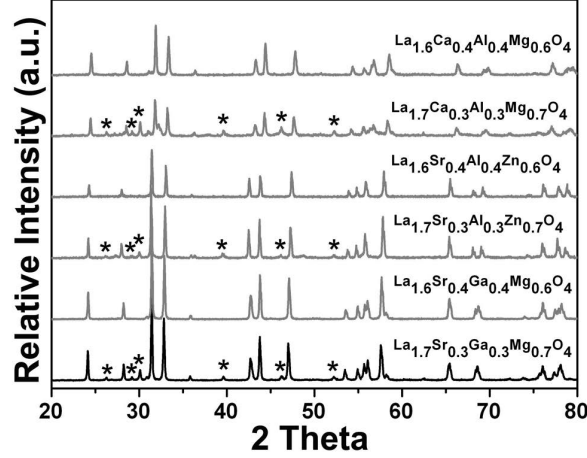


**Figure 7.9:** XRD of Ga, Zn, and Ca substituted samples. Peaks marked by \* indicate secondary phase of  $\text{La}_2\text{O}_3$ .

Starting from a composition of  $\text{La}_{1.6}\text{Sr}_{0.4}\text{Al}_{0.4}\text{Mg}_{0.6}\text{O}_4$ , efforts were made to increase the P-layer/R-layer charge separation when substituting Ga, Zn, or Ca. As seen in Figure 7.9, direct substitution for Al, Mg, and Ca maintained the  $\text{K}_2\text{NiF}_4$  crystal structures; however, for all three substitutions, the charge separation could not increase from  $-0.8/+0.8$  to  $-0.85/+0.85$  by changing the nominal composition from  $(\text{A}_{1.6}^{3+}\text{A}_{0.4}^{2+})(\text{B}_{0.4}^{3+}\text{B}_{0.6}^{2+})\text{O}_4$  to  $(\text{A}_{1.7}^{3+}\text{A}_{0.3}^{2+})(\text{B}_{0.3}^{3+}\text{B}_{0.7}^{2+})\text{O}_4$ . Increasing the charge separation in all cases led to the appearance of second phase  $\text{La}_2\text{O}_3$ .

By comparing the XRD results of the samples with nominal composition  $(\text{A}_{1.6}^{3+}\text{A}_{0.4}^{2+})(\text{B}_{0.4}^{3+}\text{B}_{0.6}^{2+})\text{O}_4$  in Figure 7.9, the peak locations of the Ca substituted sample are clearly shifted to higher angle compared to the corresponding peaks of the Ga or Zn containing samples, indicating reduced lattice parameters. Lattice parameters for these and other compositions could be determined from the XRD. The results shows that both the a and c lattice parameters of LSAM are increased by Ga and Zn substitution, while they are both reduced by Ca substitution. These results are intuitive, since the ionic radii of Ga and Zn are larger than those of Al and Mg, but Ca is smaller than Sr.

As shown in Figure 7.10, the microstructures of the sintered pellets reveal that

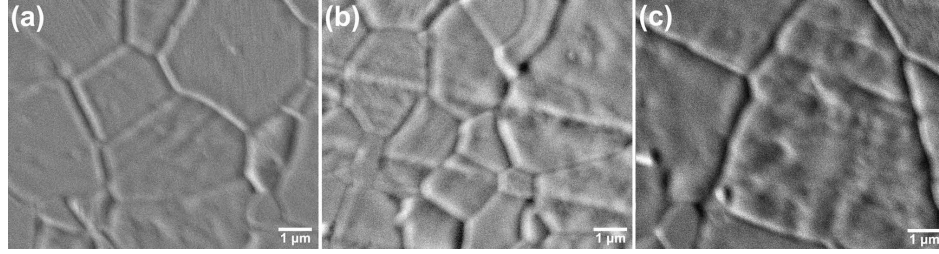


**Figure 7.10:** Representative SEM micrographs of the polished and thermally etched surfaces of sintered pellets with composition (a)  $\text{La}_{1.6}\text{Ca}_{0.4}\text{Al}_{0.4}\text{Mg}_{0.6}\text{O}_4$ , (b)  $\text{La}_{1.6}\text{Ga}_{0.4}\text{Al}_{0.4}\text{Mg}_{0.6}\text{O}_4$ , and (c)  $\text{La}_{1.6}\text{Sr}_{0.4}\text{Al}_{0.4}\text{Zn}_{0.6}\text{O}_4$ .

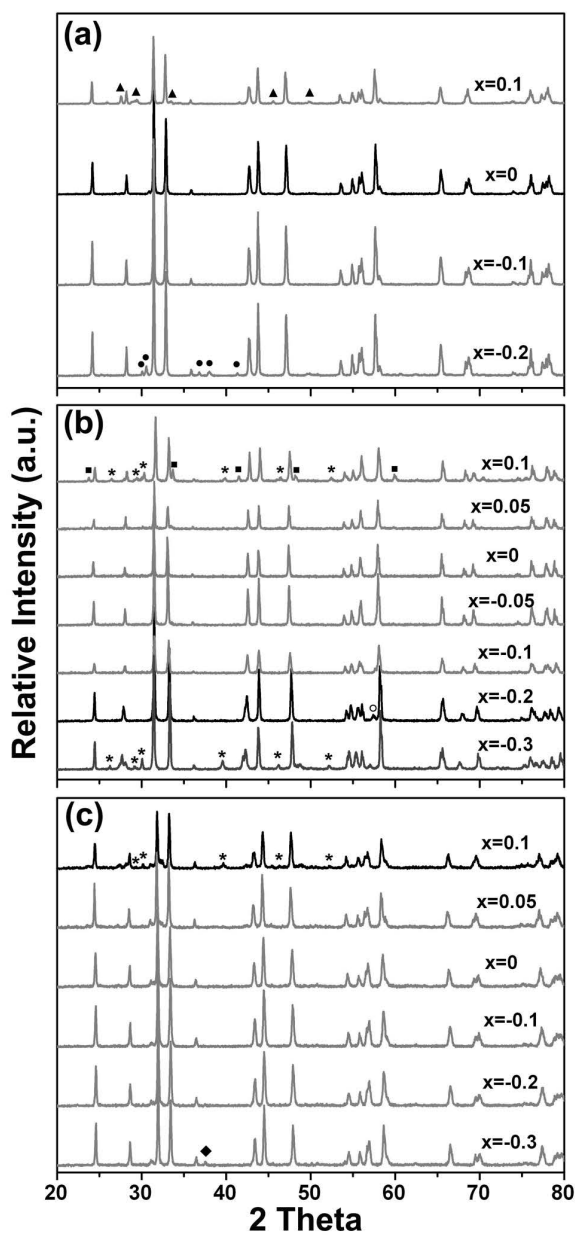
dense ceramic structures with little porosity are obtained for all three stoichiometric samples. This result is consistent with the  $\approx 95\%$  pellet densities determined by Archimedes method. The grain sizes for the sintered pellets are between  $1\ \mu\text{m} - 8\ \mu\text{m}$ . No intergranular phases are observed in the micrographs, though they may be present at quantities/thicknesses smaller than could be observed presently.

Figure 7.11 shows the results of adjusting the A-site ratio in order to create ionic defects. Increasing the ratio of  $\text{A}^{3+}/\text{A}^{2+}$  ( $x > 0$ ) in  $(\text{A}_{1.6+x}^{3+}\text{A}_{0.4-x}^{2+})(\text{B}_{0.4}^{3+}\text{B}_{0.6}^{2+})\text{O}_{4+x/2}$  ideally creates oxygen interstitials, while decreasing the ratio ( $x < 0$ ) creates oxygen vacancies. The XRD results in Figure 7.11 indicate that, for all samples studied, a higher concentration of oxygen vacancies could be created relative to oxygen interstitials before the appearance of secondary phases. In Ga containing samples,  $x$  could be  $-0.1$  without second phases, whereas  $\text{La}_4\text{Ga}_2\text{O}_9$  peaks appear when  $x = +0.1$ . For both Zn and Ca substitutions, the  $\text{K}_2\text{NiF}_4$  structure was stable when  $-0.2 \leq x \leq +0.05$ . In the Zn containing specimen, increasing amounts of oxygen vacancies leads to reduction in the  $a$  lattice parameter and increase in the  $c$  parameter. This leads to increased peak splitting between the (133) and (008) peaks. Thus, the peak at  $2\theta = 57.41^\circ$  marked with  $\circ$  for the  $x = -0.2$  sample in Figure 7.11 (b) is the (008) peak of the  $\text{K}_2\text{NiF}_4$  structure. Since the ionic radii of the A-site cations are  $r_{(\text{Sr}^{2+},\text{IX})} = 1.31\ \text{\AA} > r_{(\text{La}^{3+},\text{IX})} = 1.216\ \text{\AA} > r_{(\text{Ca}^{2+},\text{IX})} = 1.18\ \text{\AA}$ , reducing the La/Sr ratio in Zn containing samples caused significant increase of lattice parameter  $c$ , while reducing the La/Ca ratio in

Ca containing samples led to significant decrease of lattice parameter  $c$ . In general, reducing the La/Sr or La/Ca ratio caused a slight decrease in lattice parameter  $a$ .

Substitution of Ca on the A-site caused relatively little change in the total electrical conductivity. As shown in Figure 7.12, increasing the La/Ca ratio in order to create oxygen interstitials caused an increase in both the high temperature conductivity and activation energy of conduction. The electrical conductivity of  $\text{La}_{1.6+x}\text{Ca}_{0.4-x}\text{Al}_{0.4}\text{Mg}_{0.6}\text{O}_4$  is very similar to the previously reported values for  $\text{La}_{1.6+x}\text{Sr}_{0.4-x}\text{Al}_{0.4}\text{Mg}_{0.6}\text{O}_4$ . [164] The inset in Figure 7.12 plots the conductivity at 650 °C vs. the oxygen stoichiometry and suggests a moderate amount of interstitial conductivity in both the superstoichiometric and stoichiometric compositions. When the La/Ca ratio is reduced such that vacancies are expected on the oxygen sublattice, the conductivity values are within experimental error of that of the previously reported  $\text{La}_{1.6}\text{Sr}_{0.4}\text{Al}_{0.4}\text{Mg}_{0.6}\text{O}_4$  sample. These results indicate that the vacancies have low mobility. The similarity of the conductivity values for these samples, despite the increasing vacancy concentration, suggests that the charge carrier concentration does not change with composition. The carrier concentration is thus determined by either intrinsic defects or impurities acting as dopants.

Figure 7.13 shows the conductivity of the  $\text{La}_{1.6+x}\text{Ca}_{0.4-x}\text{Al}_{0.4}\text{Mg}_{0.6}\text{O}_{4+x/2}$  samples at 550 °C over a range of oxygen partial pressures. The conductivities of all compositions are essentially independent of the oxygen partial pressure, with the slopes of the best-fit lines  $\leq 0.007$ . This result gives further indication that the dominant charge carriers are ionic,[172, 173] since electronic carriers are expected to have concentrations that are determined by oxidation reactions and thus dependent upon the oxygen partial pressure[174, 175]. Nevertheless, the small change in conductivity despite  $x$  varying between +0.05 and -0.2 implies low mobility of the created defects. A similar phenomenon was observed in  $\text{La}_{1.6+x}\text{Sr}_{0.4-x}\text{Al}_{0.4}\text{Mg}_{0.6}\text{O}_{4+x/2}$ , [164, 176] which has the same B-site composition. The reason that defect mobilities are low in  $\text{K}_2\text{NiF}_4$  materials that have only period 3 elements in the B-site remains an open question, but



**Figure 7.11:** (a) XRD of  $\text{La}_{1.6+x}\text{Sr}_{0.4-x}\text{Ga}_{0.4}\text{Mg}_{0.6}\text{O}_{4+x/2}$ ; (b) XRD of  $\text{La}_{1.6+x}\text{Sr}_{0.4-x}\text{Ga}_{0.4}\text{Mg}_{0.6}\text{O}_{4+x/2}$ ; (c) XRD of  $\text{La}_{1.6+x}\text{Ca}_{0.4-x}\text{Al}_{0.4}\text{Mg}_{0.6}\text{O}_{4+x/2}$ . Peaks marked by: \* indicate  $\text{La}_2\text{O}_3$ , ▲ indicate  $\text{La}_4\text{Ga}_2\text{O}_9$ , ● indicate  $\text{LaSr}_2\text{GaO}_5$ , ■ indicate  $\text{LaAlO}_3$ , and ◆ indicate  $\text{CaO}$ .

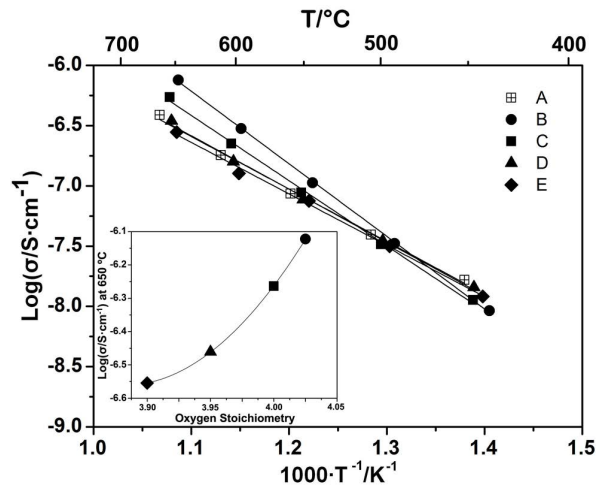


**Figure 7.12:** Arrhenius plot of total electrical conductivity measured in air for A.  $\text{La}_{1.6}\text{Sr}_{0.4}\text{Al}_{0.4}\text{Mg}_{0.6}\text{O}_4$ ; and the Ca substituted samples B.  $\text{La}_{1.65}\text{Ca}_{0.35}\text{Al}_{0.4}\text{Mg}_{0.6}\text{O}_{4.025}$ ; C.  $\text{La}_{1.6}\text{Ca}_{0.4}\text{Al}_{0.4}\text{Mg}_{0.6}\text{O}_4$ ; D.  $\text{La}_{1.5}\text{Ca}_{0.5}\text{Al}_{0.4}\text{Mg}_{0.6}\text{O}_{3.95}$ ; E.  $\text{La}_{1.4}\text{Ca}_{0.6}\text{Al}_{0.4}\text{Mg}_{0.6}\text{O}_{3.9}$ . The inset figure displays the conductivity at  $650^\circ\text{C}$  vs. the oxygen stoichiometry.

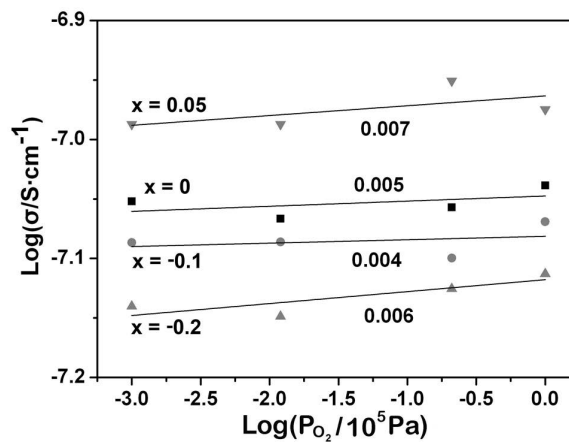


**Figure 7.13:** Total electrical conductivity at  $550^\circ\text{C}$  of  $\text{La}_{1.6+x}\text{Ca}_{0.4-x}\text{Al}_{0.4}\text{Mg}_{0.6}\text{O}_{4+x/2}$  vs. oxygen partial pressure for compositions with  $x = -0.2, -0.1, 0,$  and  $+0.05$ . The near-zero slopes of the best fit lines are indicated next to each line.

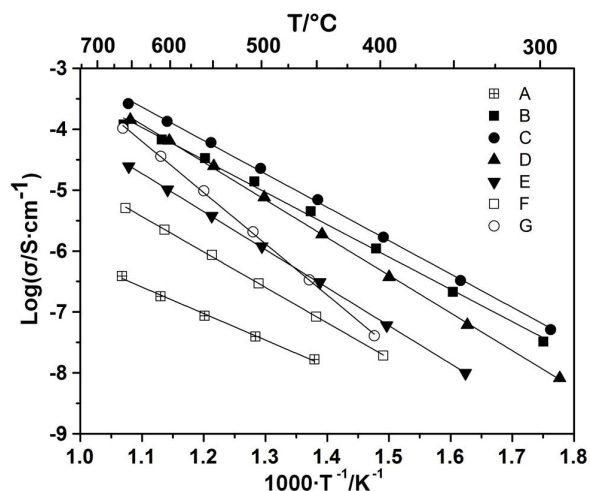


**Figure 7.14:** Arrhenius plot of the total electrical conductivity measured in air for A.  $\text{La}_{1.6}\text{Sr}_{0.4}\text{Al}_{0.4}\text{Mg}_{0.6}\text{O}_4$ ; and the B-site substituted samples B.  $\text{La}_{1.6}\text{Sr}_{0.4}\text{Al}_{0.4}\text{Zn}_{0.6}\text{O}_4$ ; C.  $\text{La}_{1.5}\text{Sr}_{0.5}\text{Al}_{0.4}\text{Zn}_{0.6}\text{O}_{3.95}$ ; D.  $\text{La}_{1.4}\text{Sr}_{0.6}\text{Al}_{0.4}\text{Zn}_{0.6}\text{O}_{3.9}$ ; E.  $\text{La}_{1.65}\text{Sr}_{0.35}\text{Al}_{0.4}\text{Zn}_{0.6}\text{O}_{4.025}$ ; F.  $\text{La}_{1.6}\text{Ga}_{0.4}\text{Al}_{0.4}\text{Mg}_{0.6}\text{O}_4$ ; G.  $\text{La}_{1.5}\text{Sr}_{0.5}\text{Ga}_{0.4}\text{Mg}_{0.6}\text{O}_{3.95}$ . In all cases, square symbols indicate compositions with stoichiometric oxygen content.

is perhaps due to the small cell volume[166] and/or low polarizability[177] related to their small ionic radii.

Figure 7.14 shows that B-site substitutions caused a much greater change in conductivity than A-site substitutions. For the oxygen stoichiometric compositions, Ga substitution yielded roughly one order of magnitude increase in the electrical conductivity relative to the original LSM composition, and Zn substitution caused a further increase by a little over one order of magnitude. Unlike the LSM or the Ca-substituted compositions, decreasing the La/Sr ratio from that of the stoichiometric composition in the Ga- and Zn- substituted samples increased the conductivity. In the Zn-containing compositions, the conductivity improves from  $x = 0$  to  $x = -0.1$ , however, further increases in the defect concentration at  $x = -0.2$  yields lower conductivity. The reason for this may be an impurity phase not perceptible by XRD or SEM. A strong possibility is a Sr-rich phase, which is often observed to form a poorly-conducting layer

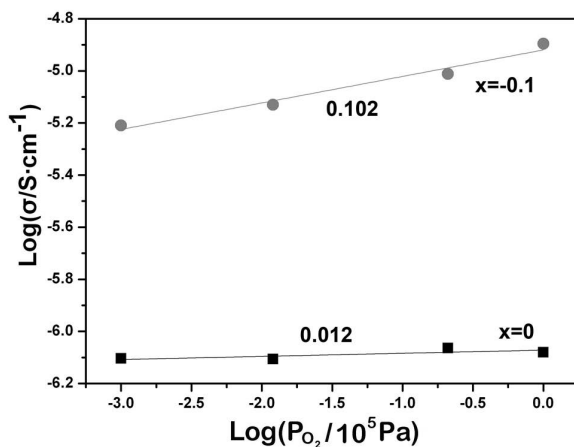


**Figure 7.15:** Total electrical conductivity at 550 °C of  $\text{La}_{1.6+x}\text{Sr}_{0.4-x}\text{Ga}_{0.4}\text{Mg}_{0.6}\text{O}_{4+x/2}$  vs. oxygen partial pressure for compositions with  $x = -0.1$  and 0. The slopes of the best-fit lines are indicated.

at grain boundaries in perovskite oxide ion conductors[178]. An increase in activation energy from 1.15 eV for  $x = -0.1$  to 1.30 eV for  $x = -0.2$  could be seen as evidence for this hypothesis, but confirmation is still needed. Increasing the La/Sr ratio from that of the stoichiometric composition in the Zn-substituted samples (which was not possible in the Ga-substituted samples) reduced the conductivity significantly.

Figure 7.15 shows the total electrical conductivity at 550 °C of  $\text{La}_{1.6+x}\text{Sr}_{0.4-x}\text{Ga}_{0.4}\text{Mg}_{0.6}\text{O}_{4+x/2}$  measured in various oxygen partial pressures. The electrical conductivity of stoichiometric  $\text{La}_{1.6}\text{Ga}_{0.4}\text{Al}_{0.4}\text{Mg}_{0.6}\text{O}_4$  has near-zero dependence on the oxygen partial pressure, indicating that the conduction mechanism is via intrinsic defects at a concentration larger than is created by redox reactions. Studies of the similar compositions  $\text{LaSrGa}_{1-x}\text{Mg}_x\text{O}_{4-x/2}$  (for which a low value of 0.03 was reported as the maximum possible  $x$ , consistent with our theory of defects being stabilized by charge separation between the P-layer and R-layer), found evidence of oxygen ion conduction,[179] but ionic conduction cannot be definitively determined here. Oxygen substoichiometric  $\text{La}_{1.5}\text{Sr}_{0.5}\text{Ga}_{0.4}\text{Mg}_{0.6}\text{O}_{3.95}$  exhibited a more clear oxygen partial pressure dependence of

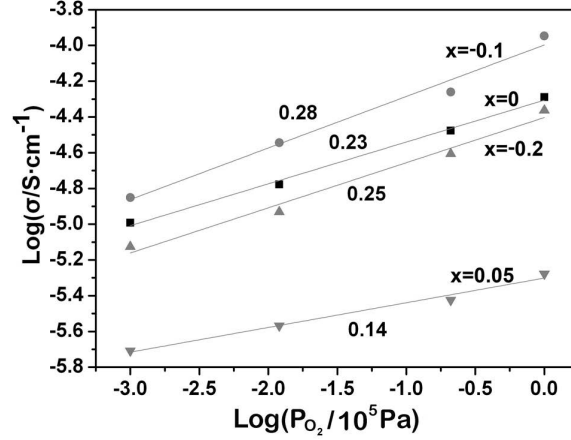


**Figure 7.16:** Total electrical conductivity at 550 °C of  $\text{La}_{1.6+x}\text{Sr}_{0.4-x}\text{Ga}_{0.4}\text{Mg}_{0.6}\text{O}_{4+x/2}$  vs. oxygen partial pressure for compositions with  $x = -0.2, -0.1, 0,$  and  $+0.05$ . The slopes of the best fit lines are indicated.

conductivity. The total conductivity can be represented by[174, 175]

$$\sigma_{tot} = \sigma_{ion} + \sigma_h^o P_{O_2}^{1/6} \quad (7.9)$$

where  $\sigma_{tot}$  is total conductivity,  $\sigma_{ion}$  is oxygen ionic conductivity and  $\sigma_h^o$  is hole conductivity at  $P_{O_2} = 1$  atm. Equation 7.9 indicates that oxygen ion conductivity is independent of oxygen partial pressure while hole conductivity has a 1/4 power law dependence[174, 175]. The oxygen partial pressure dependence of conductivity measured for  $\text{La}_{1.5}\text{Sr}_{0.5}\text{Ga}_{0.4}\text{Mg}_{0.6}\text{O}_{3.95}$  is about 0.102. The deviation from classic 1/4 power dependence is very common in other mixed conducting materials[169]. Since the conductivity increases with oxygen substoichiometry, the predominant charge carrier in  $\text{La}_{1.5}\text{Sr}_{0.5}\text{Ga}_{0.4}\text{Mg}_{0.6}\text{O}_{3.95}$  seems to be mixed between vacancies and holes.

Figure 7.16 shows the total electrical conductivity at 550 °C of the  $\text{La}_{1.6+x}\text{Sr}_{0.4-x}\text{Ga}_{0.4}\text{Mg}_{0.6}\text{O}_{4+x/2}$  series samples over a range of oxygen partial pressures. When  $x$  is between 0 and -0.2, the conductivity has a roughly 1/4 power law dependence over the entire range of oxygen partial pressures. This result indicates that the main charge carriers are holes, as described previously. For the  $x = +0.05$  composition, where interstitial defects are expected, the slope of the oxygen partial pressure dependence

appears to be 1/6. This result suggests that the defect concentration is no longer fixed by the stoichiometry, but rather the charge carrier concentrations are determined by the oxidation reaction.

In this work, A-site and B-site substitutions caused contrasting effects on the conductivity. While all of the tested compositional changes caused increases in the conductivity of stoichiometric samples, the A-site substitution of Ca caused the conductivity to increase with increasing interstitial defects and decrease with vacancy defects. In contrast, both B-site substitutions caused the conductivity to increase with the presence of vacancies and decrease with interstitial defects if the crystal structure even allowed them. This result further supports the notion that positively charged vacancies prefer to inhabit a negatively charged perovskite layer with composition  $ABO_3$  and negatively charged interstitials prefer to inhabit a positively charged rocksalt layer with composition  $AO$ . Still, the presence of mixed conduction in the B-site substituted samples indicates that getting sufficient oxide ion mobility without coincident electron/hole conductivity in the  $K_2NiF_4$  structure will be difficult.

In the transition-metal-free  $K_2NiF_4$  oxides, the electronic conductivity could be greatly suppressed compared to prototype  $La_2NiO_4$  materials. Large amounts of oxygen defects could also be created. Nonetheless, probably due to the presence of alkaline earth metal/post-transition metals in the B-site, the as-created oxygen defects had low mobility. Therefore, although oxygen ion conductors were achieved with A-site substitution of Ca, the ionic conductivity remained extremely low. In future work, new strategy to select B-site atoms that increase the mobility of oxygen defects without reintroducing electronic conductivity would be key to the success of designing  $K_2NiF_4$  electrolyte materials.

## 7.4 Summary

New oxide compositions that adopt the  $K_2NiF_4$  crystal structure despite a B-site free of transition metals have been achieved with the  $La_{1.6}Sr_{0.4}Al_{0.4}Mg_{0.6}O_4$  composition. Substitution of Ni by Mg and Al leads to orders of magnitude decreases in total

electrical conductivity due to the removal of the  $\text{Ni}^{3+}/\text{Ni}^{2+}$  polaron carriers. The conductivity of all measured samples in the compositional series  $\text{La}_{1.6}\text{Sr}_{0.4}\text{Al}_{0.4}\text{Ni}_{1-x}\text{Mg}_{x-0.4}\text{O}_4$  is controlled by oxygen nonstoichiometry. While more detailed defect chemistry studies are needed to definitively ascertain the charge carriers in these compositions, the increased charge separation between the rocksalt and perovskite layers relative to  $\text{LaSrAlO}_4$  seemed to allow the creation of moderate concentrations of both vacancy and interstitial oxygen ion defects. Nevertheless, the total conductivity and thus the maximum possible mobility of the ionic defects remained low, which is likely related to the increased concentration of Sr.  $\text{La}_{1.6+x}\text{Sr}_{0.4-x}\text{Ga}_{0.4}\text{Mg}_{0.6}\text{O}_{4+x/2}$  ( $-0.1 \leq x \leq 0$ ),  $\text{La}_{1.6+x}\text{Sr}_{0.4-x}\text{Ga}_{0.4}\text{Mg}_{0.6}\text{O}_{4+x/2}$  ( $-0.2 \leq x \leq +0.05$ ) and  $\text{La}_{1.6+x}\text{Ca}_{0.4-x}\text{Al}_{0.4}\text{Mg}_{0.6}\text{O}_{4+x/2}$  ( $-0.2 \leq x \leq +0.05$ ) with  $\text{K}_2\text{NiF}_4$  structure were synthesized without impurity phases. Compared to the electrical conductivity of LSAM, the electrical conductivity was relatively constant when replacing Sr with Ca, but increased by between 1 and 2.5 orders of magnitude when substituting Al or Mg with Ga or Zn. Electrochemical analysis revealed that  $\text{La}_{1.6+x}\text{Ca}_{0.4-x}\text{Al}_{0.4}\text{Mg}_{0.6}\text{O}_{4+x/2}$  appeared to support electrolytic conduction of interstitial oxygen ions, though with low conductivity. Conversely, the main carriers in  $\text{La}_{1.6+x}\text{Sr}_{0.4-x}\text{Ga}_{0.4}\text{Mg}_{0.6}\text{O}_{4+x/2}$  seemed to be holes. In  $\text{La}_{1.6+x}\text{Sr}_{0.4-x}\text{Ga}_{0.4}\text{Mg}_{0.6}\text{O}_{4+x/2}$ ,  $x = 0$  appeared to be predominantly an ionic conductor while  $x = -0.1$  was a mixed conductor of holes and oxygen vacancies. The results indicate that electrolytic conduction is possible in transition-metal-free  $\text{K}_2\text{NiF}_4$  oxides, but high ionic mobility has yet to be achieved.

## Chapter 8

### CONCLUSIONS AND FUTURE WORK

#### 8.1 Conclusions

We have investigated interfacial thermal conductance between a range of clean and structurally well-characterized metal-semiconductor interfaces using the Time-Domain Thermoreflectance (TDTR) experimental technique, and have provided theoretical/computational insight to the experimental data where possible. By studying the interfaces between a variety of materials systems, each with unique aspects to their tunability, we have been able to answer a number of outstanding questions regarding the importance of interfacial quality (epitaxial/non-epitaxial interfaces), semiconductor doping, matching of acoustic and optical phonon band structure, and the role of phonon transport mechanisms apart from direct elastic transmission on ITC.

In Chapter 3, I fabricate  $\text{CoSi}_2$ ,  $\text{TiSi}_2$ ,  $\text{NiSi}$  and  $\text{PtSi}$  films with different structures and interfaces on  $\text{Si}(100)$  and  $\text{Si}(111)$  wafer. Then TDTR is applied to measure the ITC of these silicides-silicon interfaces with clean and well-characterized interfaces.  $\text{CoSi}_2$ ,  $\text{TiSi}_2$  and  $\text{NiSi}$  are demonstrated to be extremely good thermal interface conductance materials for Si, and are some of the highest ever measured for a metal-semiconductor interface. Interestingly, we find that the interfacial thermal conductance is not dependent on whether the interface is epitaxially grown or what the substrate orientation is. Above 100 K a coherent AGF approach significantly underpredicts interface conductance in the case of  $\text{CoSi}_2$  suggesting that energy transport does not occur purely by coherent transmission of phonons, even for epitaxial interfaces.  $\text{CoSi}_2$  comparison to a coherent (i.e. non-diffuse) model can also explain the experimental data, but only when anharmonic and near-interface electron-phonon coupling are accurately considered. A full-dispersion diffuse mismatch model closely predicts the experimentally

observed interface conductances for CoSi<sub>2</sub>, NiSi, and TiSi<sub>2</sub> interfaces, while it remains an open question whether inelastic scattering, cross-interfacial electron-phonon coupling, or other mechanisms could also account for the high temperature behavior. The effect of degenerate semiconductor dopant concentration on metal-semiconductor thermal interface conductance was also investigated with the result that we have found no dependencies of the thermal interface conductances up to (n-type or p-type)  $\approx 1 \times 10^{19}$  cm<sup>-3</sup>, indicating that there is no significant direct electronic transport and no transport effects which depend on long-range metal-semiconductor band alignment.

Then, in Chapter 4, we tune the phonon band structure of NiAl<sub>1-x</sub>Ga<sub>x</sub> by changing the composition of the alloy, and study the influences of the phonon band structure on the ITC of the epitaxial NiAl<sub>1-x</sub>Ga<sub>x</sub>-GaAs interfaces. While  $x$  increases from 0 to 0.6, the phonon band demonstrates a decrease in phonon band gap, as well as the optical phonon in NiAl<sub>1-x</sub>Ga<sub>x</sub> alloy continuously decreases with a best matched with that of GaAs at alloy composition of  $x = 0.6$ . As  $x$  increases from 0.6 to 1, the optical phonon in NiAl<sub>1-x</sub>Ga<sub>x</sub> alloy becomes smaller than that of GaAs, as well as acoustic phonon density of states of NiAl<sub>1-x</sub>Ga<sub>x</sub> alloy aligned better with that of GaAs. ITC results from TDTR experiment data shows a linearly increase from  $x = 0$  to  $x = 1$ , with a 30% of increasement. Full-phonon DMM predicts an increasing behavior from  $x = 0$  to 0.6 with 100% of increasement and a nearly constant value from  $x = 0.6$  to  $x = 1$ .

Last, in Chapter 5 we form a series of epitaxial interface with increasing metal atomic mass in group IV metal nitrides, whereby acoustic phonons are tuned to lower the frequency without significantly changing the optical phonons. The ITC of epitaxial group IV metal nitrides on MgO and on ScN interfaces are measured with TDTR and the full-phonon dispersion DMM are calculated. The results indicate that ITC of these interfaces is generally quite high. Interestingly, despite the fact that MgO and ScN have similar phonon dispersions, group IV metal nitrides grown on ScN exhibit much high interface conductance than those on MgO, indicating the phonon dispersion cannot be the sole factor influencing transport. Some of the experiment results are clearly

higher than elastic phonon radiation limit, demanding that other phonon transport mechanisms, like direct electron transport, cross interface electron-phonon coupling and inelastic phonon transmission must be important in these interfaces.

## 8.2 Future work

Most of the modeling by DMM in this work aims to understand the role of the elastic phonon transport process across metal-semiconductor interfaces. We do find that in some cases (e.g. group IV nitrides on ScN), the elastic phonon transport process is not dominant. More advanced simulation methods, like LD, AGF and MD, must be applied to understand the thermal transport processes from inelastic phonons, cross interface electron-phonon coupling and electron-phonon coupling within the metal in these interfaces. In addition, some other interesting research experiments could be conducted and possibly can help us sort the contributions of these processes out. (Like what?)

First, better understanding of simpler interfaces could help. For example, semiconductor-semiconductor interfaces are less complicated systems could begin with. The study of semiconductor-semiconductor interface can improve the understanding the mechanisms of the elastic and inelastic phonon transport processes. The challenge of measuring semiconductor-semiconductor interfaces is that, in current TDTR setup, a metal transducer is required for the laser power absorption and thermoreflectance signal collecting. The appearance of the metal layer complicates data analysis in the measurement of ITC of semiconductor-semiconductor interfaces. Recently, no-transducer measurements based on a combination of time-domain and frequency-domain thermoreflectance setup is reported[180], which can be a feasible way for precise single semiconductor-semiconductor interface measurement.

Another interesting study of the ITC would be thermal transport between metal and metal-semiconductor alloy interfaces. The transition behavior of ITC from metal-metal to metal-semiconductor interfaces would enable to sort out the ITC contribution

from different processes. The challenge of this project is to find metal and semiconductors that can form arbitrary alloy composition without a second phase as well as with decent thermal conductivity for enough sensitivity to the ITC when measured by TDTR.

Metals with low Debye temperature would be another interesting aspect of ITC research. For the metals with low Debye temperature, like Pb (Debye temperature 105 K), the phonon modes are ‘fully’ activated in a wide temperature range, in which the elastic phonon transport contribution remains the same. The temperature dependent ITC of Pb-semiconductor interface should be from phonon transport by electron-phonon coupling and inelastic phonon transport. Combined with advanced simulation, the contribution from the electron-phonon coupling and inelastic phonon transport could be determined. Nonetheless, Pb cannot form epitaxial films on common semiconductor substrates. Possible candidates are InSb and YSZ substrate. The challenges are the lattice mismatch of InSb and Pb (about 8 to 10%) is relatively large. For YSZ, the thermal conductivity of YSZ is small (around 7 W/m-K), but the expected ITC is about 50 MW/m<sup>2</sup>-K which mean the measurements should be still sensitive to the interface of Pb/YSZ.

## BIBLIOGRAPHY

- [1] Carolyn A Paddock and Gary L Eesley. Transient thermorefectance from thin metal films. *Journal of Applied Physics*, 60(1):285–290, 1986.
- [2] Sridhar Sadasivam, Ning Ye, Joseph P Feser, James Charles, Kai Miao, Tillmann Kubis, and Timothy S Fisher. Thermal transport across metal silicide-silicon interfaces: First-principles calculations and green’s function transport simulations. *Physical Review B*, 95(8):085310, 2017.
- [3] Ruxandra M. Costescu, Marcel A. Wall, and David G. Cahill. Thermal conductance of epitaxial interfaces. *Physical Review B*, 67(5), 2003.
- [4] Polina V Burmistrova, Jesse Maassen, Tela Favalaro, Bivas Saha, Shuaib Salamat, Yee Rui Koh, Mark S Lundstrom, Ali Shakouri, and Timothy D Sands. Thermoelectric properties of epitaxial ScN films deposited by reactive magnetron sputtering onto MgO(001) substrates. *Journal of Applied Physics*, 113(15):153704, 2013.
- [5] AK Saxena. The conduction band structure and deep levels in  $\text{Ga}_{1-x}\text{Al}_x\text{As}$  alloys from a high-pressure experiment. *Journal of Physics C: Solid State Physics*, 13(23):4323, 1980.
- [6] Jens B Smith and Truls Norby. On the steady-state oxygen permeation through  $\text{La}_2\text{NiO}_{4+\delta}$  membranes. *Journal of the Electrochemical Society*, 153(2):A233–A238, 2006.
- [7] P Ganguly and CNR Rao. Electron transport properties of transition metal oxide systems with the  $\text{K}_2\text{NiF}_4$  structure. *Materials Research Bulletin*, 8(4):405–412, 1973.
- [8] VV Kharton, AP Viskup, AV Kovalevsky, EN Naumovich, and FMB Marques. Ionic transport in oxygen-hyperstoichiometric phases with  $\text{K}_2\text{NiF}_4$ -type structure. *Solid State Ionics*, 143(3):337–353, 2001.
- [9] Bryan C Gundrum, David G Cahill, and Robert S Averback. Thermal conductance of metal-metal interfaces. *Physical Review B*, 72(24):245426, 2005.
- [10] Gang Chen. Nanoscale energy transport and conversion. 2005.
- [11] Charles Kittel. *Introduction to solid state physics*. Wiley, 2005.

- [12] Rama Venkatasubramanian, Thomas Colpitts, Brooks OQuinn, Sandra Liu, Nadia El-Masry, and Michael Lamvik. Low-temperature organometallic epitaxy and its application to superlattice structures in thermoelectrics. *Applied Physics Letters*, 75(8):1104–1106, 1999.
- [13] Rama Venkatasubramanian, Edward Siivola, Thomas Colpitts, and Brooks O’quinn. Thin-film thermoelectric devices with high room-temperature figures of merit. *Nature*, 413(6856):597–602, 2001.
- [14] PL Kapitza. The study of heat transfer in helium ii. *J. Phys.(USSR)*, 4(1-6):181–210, 1941.
- [15] DM Lee and Henry A Fairbank. Heat transport in liquid He 3. *Physical Review*, 116(6):1359, 1959.
- [16] AC Anderson, JI Connolly, and JC Wheatley. Thermal boundary resistance between solids and helium below 1 K. *Physical Review*, 135(4A):A910, 1964.
- [17] CL Reynolds Jr and AC Anderson. Thermal boundary resistance to solid helium, hydrogen, deuterium, and neon. *Physical Review B*, 14(9):4114, 1976.
- [18] CL Reynolds Jr and AC Anderson. Thermal boundary resistance to solid helium, hydrogen, deuterium, and neon. ii. *Physical Review B*, 15(11):5466, 1977.
- [19] Gerald L Pollack. Kapitza resistance. *Reviews of Modern Physics*, 41(1):48, 1969.
- [20] Donald A Neeper and JR Dillinger. Thermal resistance at indium-sapphire boundaries between 1.1 and 2.1 K. *Physical Review*, 135(4A):A1028, 1964.
- [21] G Schmidt. Thermal boundary resistance at interfaces between two dielectrics. *Physics Letters A*, 50(4):241–242, 1974.
- [22] Silas E Gustafsson, Ernest Karawacki, and M Nazim Khan. Transient hot-strip method for simultaneously measuring thermal conductivity and thermal diffusivity of solids and fluids. *Journal of Physics D: Applied Physics*, 12(9):1411, 1979.
- [23] Silas E Gustafsson, Ernest Karawacki, and M Naushad Khan. Determination of the thermal-conductivity tensor and the heat capacity of insulating solids with the transient hot-strip method. *Journal of Applied Physics*, 52(4):2596–2600, 1981.
- [24] ET Swartz and RO Pohl. Thermal resistance at interfaces. *Applied Physics Letters*, 51(26):2200–2202, 1987.
- [25] R. J. Stoner and H. J. Maris. Kapitza conductance and heat flow between solids at temperatures from 50 to 300 K. *Physical Review B*, 48(22):16373–16387, 1993.

- [26] R. B. Wilson, Brent A. Apgar, Wen-Pin Hsieh, Lane W. Martin, and David G. Cahill. Thermal conductance of strongly bonded metal-oxide interfaces. *Phys. Rev. B*, 91:115414, Mar 2015.
- [27] Kimberlee C Collins, Shuo Chen, and Gang Chen. Effects of surface chemistry on thermal conductance at aluminum-diamond interfaces. *Applied Physics Letters*, 97(8):083102, 2010.
- [28] Mark D Losego, Martha E Grady, Nancy R Sottos, David G Cahill, and Paul V Braun. Effects of chemical bonding on heat transport across interfaces. *Nature materials*, 11(6):502–506, 2012.
- [29] Dong-Wook Oh, Seok Kim, John A Rogers, David G Cahill, and Sanjiv Sinha. Interfacial thermal conductance of transfer-printed metal films. *Advanced Materials*, 23(43):5028–5033, 2011.
- [30] Ho-Ki Lyeo and David G Cahill. Thermal conductance of interfaces between highly dissimilar materials. *Physical Review B*, 73(14):144301, 2006.
- [31] G. T. Hohensee, R. B. Wilson, and D. G. Cahill. Thermal conductance of metal-diamond interfaces at high pressure. *Nat Commun*, 6:6578, 2015.
- [32] Patrick E Hopkins, Leslie M Phinney, Justin R Serrano, and Thomas E Beechem. Effects of surface roughness and oxide layer on the thermal boundary conductance at aluminum/silicon interfaces. In *2010 14th International Heat Transfer Conference*, pages 313–319. American Society of Mechanical Engineers, 2010.
- [33] John C Duda and Patrick E Hopkins. Systematically controlling Kapitza conductance via chemical etching. *Applied Physics Letters*, 100(11):111602, 2012.
- [34] Patrick E Hopkins, John C Duda, Christopher W Petz, and Jerrold A Floro. Controlling thermal conductance through quantum dot roughening at interfaces. *Physical Review B*, 84(3):035438, 2011.
- [35] Caroline S Gorham, Khalid Hattar, Ramez Cheaito, John C Duda, John T Gaskins, Thomas E Beechem, Jon F Ihlefeld, Laura B Biedermann, Edward S Piekos, Douglas L Medlin, et al. Ion irradiation of the native oxide/silicon surface increases the thermal boundary conductance across aluminum/silicon interfaces. *Physical Review B*, 90(2):024301, 2014.
- [36] A. J. Minnich, J. A. Johnson, A. J. Schmidt, K. Esfarjani, M. S. Dresselhaus, K. A. Nelson, and G. Chen. Thermal conductivity spectroscopy technique to measure phonon mean free paths. *Phys. Rev. Lett.*, 107:095901, Aug 2011.
- [37] R. B. Wilson and D. G. Cahill. Anisotropic failure of fourier theory in time-domain thermoreflectance experiments. *Nat Commun*, 5:5075, 2014.

- [38] IM Khalatnikov. Teploobmen mezhdru tverdym telom i geliem-ii. *Zhurnal Eksperimentalnoi I Teoreticheskoi Fiziki*, 22(6):687–704, 1952.
- [39] Eric T Swartz and Robert O Pohl. Thermal boundary resistance. *Reviews of modern physics*, 61(3):605, 1989.
- [40] Wolfgang Eisenmenger. Phonon scattering at surfaces and interfaces. In *Phonon Scattering in Condensed Matter V*, pages 204–211. Springer, 1986.
- [41] Pramod Reddy, Kenneth Castelino, and Arun Majumdar. Diffuse mismatch model of thermal boundary conductance using exact phonon dispersion. *Applied Physics Letters*, 87(21):211908, 2005.
- [42] Sebastian G Volz and Gang Chen. Molecular-dynamics simulation of thermal conductivity of silicon crystals. *Physical Review B*, 61(4):2651, 2000.
- [43] ME Lumpkin, WM Saslow, and WM Visscher. One-dimensional Kapitza conductance: Comparison of the phonon mismatch theory with computer experiments. *Physical Review B*, 17(11):4295, 1978.
- [44] N Mingo and Liu Yang. Phonon transport in nanowires coated with an amorphous material: An atomistic greens function approach. *Physical Review B*, 68(24):245406, 2003.
- [45] Piyush Singh, Myunghoon Seong, and Sanjiv Sinha. Detailed consideration of the electron-phonon thermal conductance at metal-dielectric interfaces. *Applied Physics Letters*, 102(18):181906, 2013.
- [46] Sridhar Sadasivam, Umesh V. Waghmare, and Timothy S. Fisher. Electron-phonon coupling and thermal conductance at a metal-semiconductor interface: First-principles analysis. *Journal of Applied Physics*, 117(13):134502, 2015.
- [47] Kwangu Kang, Yee Kan Koh, Catalin Chiritescu, Xuan Zheng, and David G. Cahill. Two-tint pump-probe measurements using a femtosecond laser oscillator and sharp-edged optical filters. *Review of Scientific Instruments*, 79(11):114901, 2008.
- [48] David G. Cahill. Analysis of heat flow in layered structures for time-domain thermoreflectance. *Review of Scientific Instruments*, 75(12):5119–5122, 2004.
- [49] P. Giannozzi, S. Baroni, N. Bonini, M. Calandra, R. Car, C. Cavazzoni, D. Ceresoli, G. L. Chiarotti, M. Cococcioni, I. Dabo, A. Dal Corso, S. de Gironcoli, S. Fabris, G. Fratesi, R. Gebauer, U. Gerstmann, C. Gougoussis, A. Kokalj, M. Lazzeri, L. Martin-Samos, N. Marzari, F. Mauri, R. Mazzarello, S. Paolini, A. Pasquarello, L. Paulatto, C. Sbraccia, S. Scandolo, G. Sclauzero, A. P. Seitsonen, A. Smogunov, P. Umari, and R. M. Wentzcovitch. Quantum espresso: a

- modular and open-source software project for quantum simulations of materials. *J Phys Condens Matter*, 21(39):395502, 2009.
- [50] Paolo Giannozzi, Stefano De Gironcoli, Pasquale Pavone, and Stefano Baroni. Ab initio calculation of phonon dispersions in semiconductors. *Physical Review B*, 43(9):7231, 1991.
- [51] François Léonard and A. Alec Talin. Electrical contacts to one- and two-dimensional nanomaterials. *Nature Nanotechnology*, 6, 2011.
- [52] O. Vilkov, A. Fedorov, D. Usachov, L. V. Yashina, A. V. Generalov, K. Borygina, N. I. Verbitskiy, A. Gruneis, and D. V. Vyalikh. Controlled assembly of graphene-capped nickel, cobalt and iron silicides. *Sci Rep*, 3:2168, 2013.
- [53] S. M. Lee and David G. Cahill. Heat transport in thin dielectric films. *Journal of Applied Physics*, 81(6):2590, 1997.
- [54] Ce-Wen Nan, R. Birringer, David R. Clarke, and H. Gleiter. Effective thermal conductivity of particulate composites with interfacial thermal resistance. *Journal of Applied Physics*, 81(10):6692, 1997.
- [55] Kenneth E. Goodson and Y. Sungtaek Ju. Heat conduction in novel electronic films. *Annual Review of Materials Science*, 29:261–293, 1999.
- [56] D. Liu, R. Xie, N. Yang, B. Li, and J. T. Thong. Profiling nanowire thermal resistance with a spatial resolution of nanometers. *Nano Lett*, 14(2):806–12, 2014.
- [57] Hiroshi Ishiwara, Kohki Hikosaka, and Seijiro Furukawa. Channeling and backscattering studies of the crystalline perfection and the thermal stability of epitaxial PtSi films on Si. *Journal of Applied Physics*, 50(8):5302–5306, 1979.
- [58] M. Lawrence A. Dass, David B. Fraser, and Chih-hih Wei. Growth of epitaxial CoSi<sub>2</sub> on (100)Si. *Applied Physics Letters*, 58(12):1308–1310, 1991.
- [59] F. Arnaud D’Avitaya, S. Delage, E. Rosencher, and J. Derrien. Kinetics of formation and properties of epitaxial CoSi<sub>2</sub> films on Si(111). *Journal of Vacuum Science and Technology B*, 3(2):770–773, 1985.
- [60] D. Mangelinck, J. Y. Dai, J. S. Pan, and S. K. Lahiri. Enhancement of thermal stability of NiSi films on (100)Si and (111)Si by Pt addition. *Applied Physics Letters*, 75(12):1736–1738, 1999.
- [61] Wen-Kai Wan and Shinn-Tyan Wu. Epitaxial TiSi<sub>2</sub> on silicon by rapid thermal annealing. *Materials Letters*, 30(1):105 – 108, 1997.
- [62] Jun-Mo Yang, Ju-Chul Park, Dae-Gyu Park, Kwan-Yong Lim, Soun-Young Lee, Sung-Wook Park, and Youn-Joong Kim. Epitaxial C49-TiSi<sub>2</sub> phase formation on the silicon (100). *Journal of Applied Physics*, 94(6):4198–4202, 2003.

- [63] C. J. Chien, H. C. Cheng, C. W. Nieh, and L. J. Chen. Epitaxial growth of  $\text{VSi}_2$  on (111) Si. *Journal of Applied Physics*, 57(6):1887–1889, 1985.
- [64] K.H Kim, J.-S Kang, C.K Choi, J.Y Lee, and C.G Olson. The electronic structures of epitaxial  $\text{CrSi}_2$  film prepared on Si(111) substrate. *Applied Surface Science*, 150(14):8 – 12, 1999.
- [65] M.G. Grimaldi, G. Franz, S. Ravesi, A. Terrasi, C. Spinella, and A. La Mantia. Formation of epitaxial  $\text{-FeSi}_2$  and  $\text{-FeSi}_2$  layers on (111) Si. *Applied Surface Science*, 74(1):19 – 26, 1994.
- [66] M. Gurvitch, A. F. J. Levi, R. T. Tung, and S. Nakahara. Epitaxial yttrium silicide on (111) silicon by vacuum annealing. *Applied Physics Letters*, 51(5):311–313, 1987.
- [67] J. A. Knapp and S. T. Picraux. Epitaxial growth of rare-earth silicides on (111) Si. *Applied Physics Letters*, 48(7):466–468, 1986.
- [68] W. T. Lin and L. J. Chen. Localized epitaxial growth of hexagonal and tetragonal  $\text{MoSi}_2$  on (111) Si. *Applied Physics Letters*, 46(11):1061–1063, 1985.
- [69] C.J. Kircher. Metallurgical properties and electrical characteristics of palladium silicide-silicon contacts. *Solid-State Electronics*, 14(6):507 – 513, 1971.
- [70] I. C. Wu, J. J. Chu, and L. J. Chen. Localized epitaxial growth of  $\text{TaSi}_2$  on (111) and (001)Si by rapid thermal annealing. *Journal of Applied Physics*, 62(3):879–884, 1987.
- [71] W. T. Lin and L. J. Chen. Localized epitaxial growth of  $\text{WSi}_2$  on silicon. *Journal of Applied Physics*, 59(10):3481–3488, 1986.
- [72] Y. S. Chang and M. L. Chou. Solid-state epitaxy of osmium silicide on (111)Si under reducing atmosphere. *Journal of Applied Physics*, 66(7):3011–3013, 1989.
- [73] Ute Hörmann, Thilo Remmele, John E. Klepeis, Oleg Pankratov, Holger Grünleitner, Max Schulz, Meiken Falke, and Andrew Bleloch. Structure and electronic properties of epitaxial fluorite-type  $\text{IrSi}_2$  on Si(001). *Phys. Rev. B*, 79:104116, Mar 2009.
- [74] R. W. Fathauer, Q. F. Xiao, Shin Hashimoto, and C. W. Nieh. Columnar epitaxy of  $\text{PtSi}$  on Si(111). *Applied Physics Letters*, 57(7):686, 1990.
- [75] H. Kawarada, M. Ishida, J. Nakanishi, Ohdomari I., and Horiuchi S. High-resolution electron microscope study of the  $\text{PtSi-Si(111)}$  interface. *Philosophical Magazine A*, 54(5):729–741, 1986.

- [76] H. Kawarada, I. Ohdomari, and S. Horiuchi. Structural study of PtSi/(111)Si interface with high-resolution electron microscopy. *Japanese Journal of Applied Physics*, 23:L799–L802, 1984.
- [77] A. Wawro, S. Suto, and A. Kasuya. STM studies of PtSi formation on Si(111) by solid state epitaxy. *Physical Review B*, 72(20):205302, 2005.
- [78] M. Liehr, P. E. Schmid, F. K. LeGoues, and P. S. Ho. Correlation of schottky-barrier height and microstructure in the epitaxial Ni silicide on Si(111). *Physical Review Letters*, 54(19):2139–2142, 1985.
- [79] F. d’Heurle, C. S. Petersson, J. E. E. Baglin, S. J. La Placa, and C. Y. Wong. Formation of thin films of NiSi: Metastable structure, diffusion mechanisms in intermetallic compounds. *Journal of Applied Physics*, 55(12):4208, 1984.
- [80] H. Föll, P. S. Ho, and K. N. Tu. Transmission electron microscopy of the formation of nickel silicides. *Philosophical Magazine A*, 45(1):31–47, 1982.
- [81] Ning Ye, Joseph P Feser, Sridhar Sadasivam, Timothy S Fisher, Tianshi Wang, Chaoying Ni, and Anderson Janotti. Thermal transport across metal silicide-silicon interfaces: An experimental comparison between epitaxial and nonepitaxial interfaces. *Physical Review B*, 95(8):085430, 2017.
- [82] Brian M. Ditchek. Cobalt disilicide: Crystal growth and physical properties. *Journal of Crystal Growth*, 69:207–210, 1984.
- [83] V. Malhotra, T. L. Martin, and J. E. Mahan. Electronic transport properties of TiSi<sub>2</sub> thin films. *Journal of Vacuum Science & Technology B*, 2:10–15, 1984.
- [84] B. Meyer, U. Gottlieb, O. Laborde, H. Yang, J.C. Lasjaunias, A. Sulpice, and R. Madar. Some electronic properties of single crystalline NiSi. *Microelectronic Engineering*, 37-38:523–527, 1997.
- [85] Yuxin Wang, Ji Yong Park, Yee Kan Koh, and David G. Cahill. Thermoreflectance of metal transducers for time-domain thermoreflectance. *Journal of Applied Physics*, 108(4):043507, 2010.
- [86] M. G. Wardle, J. P. Goss, P. R. Briddon, and R. Jones. Structural and electronic properties of thin fluorite-structure NiSi<sub>2</sub>, CoSi<sub>2</sub> and FeSi<sub>2</sub> interfaces and precipitates in Si. *physica status solidi (a)*, 202(5):883–888, 2005.
- [87] John P. Perdew, Adrienn Ruzsinszky, Gábor I. Csonka, Oleg A. Vydrov, Gustavo E. Scuseria, Lucian A. Constantin, Xiaolan Zhou, and Kieron Burke. Restoring the density-gradient expansion for exchange in solids and surfaces. *Phys. Rev. Lett.*, 100:136406, Apr 2008.

- [88] G. Kresse and J. Hafner. Ab initio molecular dynamics for liquid metals. *Phys. Rev. B*, 47:558–561, Jan 1993.
- [89] G. Kresse and J. Furthmüller. Efficiency of ab-initio total energy calculations for metals and semiconductors using a plane-wave basis set. *Computational Materials Science*, 6(1):15 – 50, 1996.
- [90] G. Kresse and D. Joubert. From ultrasoft pseudopotentials to the projector augmented-wave method. *Phys. Rev. B*, 59:1758–1775, Jan 1999.
- [91] E. J. Graeber, R. J. Baughman, and B. Morosin. Crystal structure and linear thermal expansivities of platinum silicide and platinum germanide. *Acta Crystallographica Section B*, 29(9):1991–1994, Sep 1973.
- [92] A Togo and I Tanaka. First principles phonon calculations in materials science. *Scr. Mater.*, 108:1–5, Nov 2015.
- [93] Wu Li, Jess Carrete, Nebil A. Katcho, and Natalio Mingo. Shengbte: A solver of the boltzmann transport equation for phonons. *Computer Physics Communications*, 185(6):1747 – 1758, 2014.
- [94] Yuriy A. Kosevich. Fluctuation subharmonic and multiharmonic phonon transmission and Kapitza conductance between crystals with very different vibrational spectra. *Physical Review B*, 52(2):1017–1024, 1995.
- [95] Kiarash Gordiz and Asegun Henry. Phonon transport at crystalline Si/Ge interfaces: the role of interfacial modes of vibration. *Scientific Reports*, 6:23139, 2016.
- [96] M. Asheghi, K. Kurabayashi, R. Kasnavi, and K. E. Goodson. Thermal conduction in doped single-crystal silicon films. *Journal of Applied Physics*, 91(8):5079, 2002.
- [97] Ram Darolia. NiAl alloys for high-temperature structural applications. *JOM Journal of the Minerals, Metals and Materials Society*, 43(3):44–49, 1991.
- [98] DB Miracle. Overview no. 104 the physical and mechanical properties of NiAl. *Acta Metallurgica et Materialia*, 41(3):649–684, 1993.
- [99] Yoshihiro Terada, Kenji Ohkubo, Tetsuo Mohri, and Tomoo Suzuki. Thermal conductivity of intermetallic compounds with metallic bonding. *Materials transactions*, 43(12):3167–3176, 2002.
- [100] Li-Lien Lee, DE Laughlin, and DN Lambeth. NiAl underlayers for CoCrTa magnetic thin films. *IEEE Transactions on Magnetism*, 30(6):3951–3953, 1994.

- [101] Jie Zou, David E Laughlin, and David N Lambeth. CoCrTa intermediate layers on NiAl underlayers for CoCrPt longitudinal thin film magnetic media. *IEEE transactions on magnetics*, 34(4):1582–1584, 1998.
- [102] Zhijian Peng, Hezhuo Miao, Wei Wang, Size Yang, Chizi Liu, and Longhao Qi. Hard and wear-resistant titanium nitride films for ceramic cutting tools by pulsed high energy density plasma. *Surface and Coatings Technology*, 166(2):183–188, 2003.
- [103] M-A Nicolet. Diffusion barriers in thin films. *Thin Solid Films*, 52(3):415–443, 1978.
- [104] Mona Zebarjadi, Zhixi Bian, Rajeev Singh, Ali Shakouri, Robert Wortman, Vijay Rawat, and Tim Sands. Thermoelectric transport in a ZrN/ScN superlattice. *Journal of electronic materials*, 38(7):960–963, 2009.
- [105] En Yang, Sutatch Ratanaphan, Jian-Gang Zhu, and David E Laughlin. Structure and magnetic properties of L10-FePt thin films on TiN/RuAl underlayers. *Journal of Applied Physics*, 109(7):07B770, 2011.
- [106] Bivas Saha, Yee Rui Koh, Joseph P Feser, Sridhar Sadasivam, Timothy S Fisher, Ali Shakouri, and Timothy D Sands. Phonon wave effects in the thermal transport of epitaxial TiN/(Al, Sc)N metal/semiconductor superlattices. *Journal of Applied Physics*, 121(1):015109, 2017.
- [107] Jeremy L Schroeder, Bivas Saha, Magnus Garbrecht, Norbert Schell, Timothy D Sands, and Jens Birch. Thermal stability of epitaxial cubic-TiN/(Al,Sc)N metal/semiconductor superlattices. *Journal of materials science*, 50(8):3200–3206, 2015.
- [108] Eyvaz I Isaev, Si I Simak, IA Abrikosov, Rajeev Ahuja, Yu Kh Vekilov, MI Katsnelson, AI Lichtenstein, and Börje Johansson. Phonon related properties of transition metals, their carbides, and nitrides: A first-principles study. *Journal of applied physics*, 101(12):123519, 2007.
- [109] Ming Hu, Pawel Koblinski, and Patrick K. Schelling. Kapitza conductance of silicon/amorphous polyethylene interfaces by molecular dynamics simulations. *Phys. Rev. B*, 79:104305, Mar 2009.
- [110] CJ Glassbrenner and Glen A Slack. Thermal conductivity of silicon and germanium from 3 K to the melting point. *Physical Review*, 134(4A):A1058, 1964.
- [111] RO Carlson, GA Slack, and SJ Silverman. Thermal conductivity of GaAs and GaAs<sub>1-x</sub>P<sub>x</sub> laser semiconductors. *Journal of Applied Physics*, 36(2):505–507, 1965.

- [112] David G Cahill, Wayne K Ford, Kenneth E Goodson, Gerald D Mahan, Arun Majumdar, Humphrey J Maris, Roberto Merlin, and Simon R Phillpot. Nanoscale thermal transport. *Journal of Applied Physics*, 93(2):793–818, 2003.
- [113] Lon E. Bell. Cooling, heating, generating power, and recovering waste heat with thermoelectric systems. *Science*, 321(5895):1457–1461, 2008.
- [114] Francis J DiSalvo. Thermoelectric cooling and power generation. *Science*, 285(5428):703–706, 1999.
- [115] G Jeffrey Snyder and Eric S Toberer. Complex thermoelectric materials. *Nature materials*, 7(2):105–114, 2008.
- [116] Peter Zahn, Nicki F Hinsche, B Yu Yavorsky, and Ingrid Mertig. Bi<sub>2</sub>Te<sub>3</sub>: implications of the rhombohedral k-space texture on the evaluation of the in-plane/out-of-plane conductivity anisotropy. *Journal of Physics: Condensed Matter*, 23(50):505504, 2011.
- [117] Yanzhong Pei, Xiaoya Shi, Aaron LaLonde, Heng Wang, Lidong Chen, and G Jeffrey Snyder. Convergence of electronic bands for high performance bulk thermoelectrics. *Nature*, 473(7345):66–69, 2011.
- [118] Heng Wang, Yanzhong Pei, Aaron D LaLonde, and G Jeffrey Snyder. Material design considerations based on thermoelectric quality factor. In *Thermoelectric Nanomaterials*, pages 3–32. Springer, 2013.
- [119] Russell D Dupuis, PD Dapkus, Nick Holonyak Jr, EA Rezek, and R Chin. Room-temperature laser operation of quantum-well Ga<sub>1-x</sub>Al<sub>x</sub>As-GaAs laser diodes grown by metalorganic chemical vapor deposition. *Applied Physics Letters*, 32(5):295–297, 1978.
- [120] M Fischer, M Reinhardt, and A Forchel. GaInAsN/GaAs laser diodes operating at 1.52/spl mu/m. *Electronics Letters*, 36(14):1208–1209, 2000.
- [121] Steven R Kurtz, AA Allerman, ED Jones, JM Gee, JJ Banas, and BE Hammons. InGaAsN solar cells with 1.0 eV band gap, lattice matched to GaAs. *Applied Physics Letters*, 74(5):729–731, 1999.
- [122] Keisuke Nakayama, Katsuaki Tanabe, and Harry A Atwater. Plasmonic nanoparticle enhanced light absorption in GaAs solar cells. *Applied Physics Letters*, 93(12):121904, 2008.
- [123] LC West and SJ Eglash. First observation of an extremely large-dipole infrared transition within the conduction band of a GaAs quantum well. *Applied Physics Letters*, 46(12):1156–1158, 1985.

- [124] X. R. Zhou, J. H. Lee, G. J. Salamo, M. Royo, J. I. Climente, and M. F. Doty. Coulomb interaction signatures in self-assembled lateral quantum dot molecules. *Phys. Rev. B*, 87:125309, Mar 2013.
- [125] X. Zhou, S. Sanwlani, W. Liu, J. H. Lee, Zh. M. Wang, G. Salamo, and M. F. Doty. Spectroscopic signatures of many-body interactions and delocalized states in self-assembled lateral quantum dot molecules. *PHYSICAL REVIEW B*, 84(20), NOV 11 2011.
- [126] Laura E Clinger, Gilles Pernot, Trevor E Buehl, Peter G Burke, Arthur C Gosard, Christopher J Palmstrøm, Ali Shakouri, and Joshua MO Zide. Thermoelectric properties of epitaxial TbAs: InGaAs nanocomposites. *Journal of Applied Physics*, 111(9):094312, 2012.
- [127] Naresh Chand, Tim Henderson, John Klem, W Ted Masselink, Russ Fischer, Yia-Chung Chang, and Hadis Morkoç. Comprehensive analysis of Si-doped  $\text{Al}_x\text{Ga}_{1-x}\text{As}$  ( $x=0$  to 1): Theory and experiments. *Physical Review B*, 30(8):4481, 1984.
- [128] William G Breiland, Michael E Coltrin, J Randall Creighton, Hong Q Hou, Harry K Moffat, and Jeffrey Y Tsao. Organometallic vapor phase epitaxy OMVPE. *Materials Science and Engineering: R: Reports*, 24(6):241–274, 1999.
- [129] CR Abernathy, SJ Pearton, F Ren, and J Song. Sn doping of GaAs and AlGaAs by MOMBE using tetraethyltin. *Journal of crystal growth*, 113(3-4):412–416, 1991.
- [130] Xin Zhao, Kyle H Montgomery, and Jerry M Woodall. Hall effect studies of algaas grown by liquid-phase epitaxy for tandem solar cell applications. *Journal of electronic materials*, 43(11):3999, 2014.
- [131] Brian CH Steele and Angelika Heinzl. Materials for fuel-cell technologies. *Nature*, 414(6861):345–352, 2001.
- [132] Eric D Wachsman and Kang Taek Lee. Lowering the temperature of solid oxide fuel cells. *Science*, 334(6058):935–939, 2011.
- [133] Raj N Singh. High-temperature seals for solid oxide fuel cells SOFC. *Journal of Materials Engineering and Performance*, 15(4):422–426, 2006.
- [134] Natsuko Sakai, Teruhisa Horita, Katsuhiko Yamaji, Yue Ping Xiong, Haruo Kishimoto, Manuel E Brito, and Harumi Yokokawa. Material transport and degradation behavior of SOFC interconnects. *Solid State Ionics*, 177(19):1933–1939, 2006.

- [135] Zhenguo Yang, Matthew S Walker, Prabhakar Singh, and Jeff W Stevenson. Anomalous corrosion behavior of stainless steels under SOFC interconnect exposure conditions. *Electrochemical and Solid-State Letters*, 6(10):B35–B37, 2003.
- [136] Harry L Tuller. Ionic conduction in nanocrystalline materials. *Solid State Ionics*, 131(1):143–157, 2000.
- [137] CS Tedmon, HS Spacil, and SP Mitoff. Cathode materials and performance in high-temperature zirconia electrolyte fuel cells. *Journal of The Electrochemical Society*, 116(9):1170–1175, 1969.
- [138] HL Tuller and AS Nowick. Doped ceria as a solid oxide electrolyte. *Journal of the Electrochemical Society*, 122(2):255–259, 1975.
- [139] Tatsumi Ishihara, Hideaki Matsuda, and Yusaku Takita. Doped LaGaO<sub>3</sub> perovskite type oxide as a new oxide ionic conductor. *Journal of the American chemical society*, 116(9):3801–3803, 1994.
- [140] Shanwen Tao, Finn Willy Poulsen, Guangyao Meng, and Ole Toft Sørensen. High-temperature stability study of the oxygen-ion conductor La<sub>0.9</sub>Sr<sub>0.1</sub>Ga<sub>0.8</sub>Mg<sub>0.2</sub>O<sub>3-x</sub>. *Journal of Materials Chemistry*, 10(8):1829–1833, 2000.
- [141] Yuehui Wang, Xinran Zhou, Ting Wang, and Ji Zhou. Enhanced luminescence from lanthanide complex by silver nanoparticles. *Materials Letters*, 62(20):3582–3584, 2008.
- [142] Xiaojun Kuang, Mark A Green, Hongjun Niu, Pawel Zajdel, Calum Dickinson, John B Claridge, Laurent Jantsky, and Matthew J Rosseinsky. Interstitial oxide ion conductivity in the layered tetrahedral network melilite structure. *Nature materials*, 7(6):498–504, 2008.
- [143] Zhengwen Yang, Xinran Zhou, Xueguang Huang, Ji Zhou, Gang Yang, Qin Xie, Li Sun, and Bo Li. Energy transfer between fluorescent dyes in photonic crystals. *Optics letters*, 33(17):1963–1965, 2008.
- [144] PR Slater, JEH Sansom, and JR Tolchard. Development of apatite-type oxide ion conductors. *The chemical record*, 4(6):373–384, 2004.
- [145] SN Ruddlesden and P Popper. New compounds of the K<sub>2</sub>NiF<sub>4</sub> type. *Acta Crystallographica*, 10(8):538–539, 1957.
- [146] Gérard Demazeau, Michel Pouchard, and Paul Hagenmuller. Sur quelques nouveaux composés oxygénés du nickel+ iii de structure K<sub>2</sub>NiF<sub>4</sub>. *Journal of Solid State Chemistry*, 18(2):159–162, 1976.

- [147] Mathilde Rieu, R Sayers, MA Laguna-Bercero, SJ Skinner, Pascal Lenormand, and Florence Ansart. Investigation of graded  $\text{La}_2\text{NiO}_{4+\delta}$  cathodes to improve SOFC electrochemical performance. *Journal of The Electrochemical Society*, 157(4):B477–B480, 2010.
- [148] A Montenegro Hernández, L Mogni, and A Caneiro.  $\text{La}_2\text{NiO}_{4+\delta}$  as cathode for SOFC: Reactivity study with YSZ and CGO electrolytes. *international journal of hydrogen energy*, 35(11):6031–6036, 2010.
- [149] Stuart B Adler. Factors governing oxygen reduction in solid oxide fuel cell cathodes. *Chemical reviews*, 104(10):4791–4844, 2004.
- [150] EN Naumovich, MV Patrakeev, VV Kharton, AA Yaremchenko, DI Logvinovich, and FMB Marques. Oxygen nonstoichiometry in  $\text{La}_2\text{Ni}(\text{M})\text{O}_{4+\delta}$  (M= Cu, Co) under oxidizing conditions. *Solid state sciences*, 7(11):1353–1362, 2005.
- [151] Stephen J Skinner. Characterisation of  $\text{La}_2\text{NiO}_{4+\delta}$  using in-situ high temperature neutron powder diffraction. *Solid State Sciences*, 5(3):419–426, 2003.
- [152] Jean-Marc Bassat, P Odier, Antoine Villesuzanne, Christophe Marin, and Michel Pouchard. Anisotropic ionic transport properties in  $\text{La}_2\text{NiO}_{4+\delta}$  single crystals. *Solid State Ionics*, 167(3):341–347, 2004.
- [153] Licia Minervini, Robin W Grimes, John A Kilner, and Kurt E Sickafus. Oxygen migration in  $\text{La}_2\text{NiO}_{4+\delta}$ . *Journal of Materials Chemistry*, 10(10):2349–2354, 2000.
- [154] J Wan, JB Goodenough, and JH Zhu.  $\text{Nd}_{2-x}\text{La}_x\text{NiO}_{4+\delta}$ , a mixed ionic/electronic conductor with interstitial oxygen, as a cathode material. *Solid State Ionics*, 178(3):281–286, 2007.
- [155] X. Zhou and M. Doty. Design of 4-electrode optical device for application of vector electric fields to self-assembled quantum dot complexes. *Journal of Applied Physics*, 116(16):163101, 2014.
- [156] Hong-Seok Kim and Han-Ill Yoo. Effect of acceptor size and hole degeneracy on oxygen nonstoichiometry of  $\text{La}_2\text{NiO}_{4+\delta}$ . *Solid State Ionics*, 232:129–137, 2013.
- [157] AL Shaula, EN Naumovich, AP Viskup, VV Pankov, AV Kovalevsky, and VV Kharton. Oxygen transport in  $\text{La}_2\text{NiO}_{4+\delta}$ : Assessment of surface limitations and multilayer membrane architectures. *Solid State Ionics*, 180(11):812–816, 2009.
- [158] Hong-Seok Kim and Han-Ill Yoo. Defect-chemical analysis of the nonstoichiometry, conductivity and thermopower of  $\text{La}_2\text{NiO}_{4+\delta}$ . *Physical Chemistry Chemical Physics*, 12(18):4704–4713, 2010.

- [159] Jun Jiang, Xiaocao Hu, Ning Ye, and Joshua L Hertz. Microstructure and ionic conductivity of yttria-stabilized zirconia thin films deposited on MgO. *Journal of the American Ceramic Society*, 97(4):1131–1136, 2014.
- [160] KK Singh, P Ganguly, and JB Goodenough. Unusual effects of anisotropic bonding in cu (ii) and ni (ii) oxides with  $K_2NiF_4$  structure. *Journal of Solid State Chemistry*, 52(3):254–273, 1984.
- [161] JB Goodenough. Interpretation of the transport properties of  $Ln_2NiO_4$  and  $Ln_2CuO_4$  compounds. *Materials Research Bulletin*, 8(4):423–431, 1973.
- [162] Salam Abou-Warda, Walter Pietzuch, Gerd Berghöfer, Ute Kesper, Werner Massa, and Dirk Reinen. Ordered  $K_2NiF_4$  structure of the solids  $La_2Li_{1/2}M_{1/2}O_4$  (M (III)= Co, Ni, Cu) and the bonding properties of the  $MO_6$  polyhedra in various compounds of this type. *Journal of Solid State Chemistry*, 138(1):18–31, 1998.
- [163] Edwin S Raj, Stephen J Skinner, and John A Kilner. Solution synthesis and electrical properties of  $K_2NiF_4$  type  $LaSrAlO_4$ . *Solid state sciences*, 6(8):825–829, 2004.
- [164] Ning Ye and Joshua L Hertz. Creation of ionic defects in transition-metal-free oxides with  $K_2NiF_4$  structure. *Acta Materialia*, 63:123–129, 2014.
- [165] Ning Ye, Alexandra Hasbani, Jun Jiang, and Joshua L Hertz. Zn, ga, and ca substituted transition-metal-free oxides with  $K_2NiF_4$  structures. *Journal of Materials Chemistry A*, 2(20):7563–7569, 2014.
- [166] Tatsumi Ishihara, Hideaki Matsuda, Yukako Mizuhara, and Yusaku Takita. Improved oxygen ion conductivity of  $NdAlO_3$  perovskite-type oxide by doping with Ga. *Solid State Ionics*, 70:234–238, 1994.
- [167] Dibyendu Ganguli. Cationic radius ratio and formation of  $K_2NiF_4$ -type compounds. *Journal of Solid State Chemistry*, 30(3):353–356, 1979.
- [168] VV Vashook, II Yushkevich, LV Kokhanovsky, LV Makhnach, SP Tolochko, IF Kononyuk, H Ullmann, and H Altenburg. Composition and conductivity of some nickelates. *Solid State Ionics*, 119(1):23–30, 1999.
- [169] S-Y Jeon, M-B Choi, J-H Hwang, ED Wachsman, and S-J Song. Electrical conductivity and thermoelectric power of  $La_2NiO_{4+\delta}$ . *Journal of The Electrochemical Society*, 158(5):B476–B480, 2011.
- [170] S-Y Jeon, M-B Choi, H-N Im, J-H Hwang, and S-J Song. Oxygen ionic conductivity of  $La_2NiO_{4+\delta}$  via interstitial oxygen defect. *Journal of Physics and Chemistry of Solids*, 73(5):656–660, 2012.

- [171] SJ Skinner and JA Kilner. Oxygen diffusion and surface exchange in  $\text{La}_2\text{NiO}_{4+\delta}$ . *Solid State Ionics*, 135(1):709–712, 2000.
- [172] Tatsumi Ishihara, Taner Akbay, Haruyoshi Furutani, and Yusaku Takita. Improved oxide ion conductivity of Co doped  $\text{La}_{0.8}\text{Sr}_{0.2}\text{Ga}_{0.8}\text{Mg}_{0.2}\text{O}_3$  perovskite type oxide. *Solid State Ionics*, 113:585–591, 1998.
- [173] Keqin Huang and John B Goodenough. A solid oxide fuel cell based on Sr- and Mg-doped  $\text{LaGaO}_3$  electrolyte: the role of a rare-earth oxide buffer. *Journal of Alloys and Compounds*, 303:454–464, 2000.
- [174] Dorthe Lybye, Finn Willy Poulsen, and Mogens Mogensen. Conductivity of A- and B-site doped  $\text{LaAlO}_3$ ,  $\text{LaGaO}_3$ ,  $\text{LaScO}_3$  and  $\text{LaInO}_3$  perovskites. *Solid State Ionics*, 128(1):91–103, 2000.
- [175] I Kosacki and HL Tuller. Mixed conductivity in  $\text{SrCe}_{0.95}\text{Yb}_{0.05}\text{O}_3$  protonic conductors. *Solid State Ionics*, 80(3-4):223–229, 1995.
- [176] Ning Ye and Joshua L Hertz. Electrolytic conduction in transition-metal-free oxides with  $\text{K}_2\text{NiF}_4$  structure. In *Meeting Abstracts*, number 16, pages 743–743. The Electrochemical Society, 2014.
- [177] Stephen Hull. Superionics: crystal structures and conduction processes. *Reports on Progress in Physics*, 67(7):1233, 2004.
- [178] Keqin Huang, Robin S Tichy, and John B Goodenough. Superior perovskite oxide-ion conductor; strontium-and magnesium-doped  $\text{LaGaO}_3$ : I, phase relationships and electrical properties. *Journal of the American ceramic society*, 81(10):2565–2575, 1998.
- [179] Naoto Kitamura, Naoki Hamao, Sven C Vogel, and Yasushi IDEMOTO. Oxide-ion conduction, average and local structures of  $\text{LaSrGa}_{1-x}\text{Mg}_x\text{O}_{4-\delta}$  with layered perovskite structure. *Electrochemistry*, 81(6):448–453, 2013.
- [180] L Wang, R Cheaito, JL Braun, A Giri, and PE Hopkins. Thermal conductivity measurements of non-metals via combined time-and frequency-domain thermoreflectance without a metal film transducer. *Review of Scientific Instruments*, 87(9):094902, 2016.

**Appendix A**  
**REPRINT PERMISSION LIST**

Permissions for reprinting figures published in journals were provided by the respective publishers. A list for all the permissions is attached.



My Orders My Library My Profile

Welcome ningye@udel.edu Log out | Help

My Orders > Orders > All Orders

### My Orders

Orders Billing History Payable Invoices

#### SEARCH

Order Number:

Date Range: From  To  Go

View:  All  Response Required  Pending  Completed  Canceled  Denied  Credited

Results: 1-4 of 4

Order Date	Article Title	Publication	Type Of Use	Order Status	Order Number
14-Jul-2017	Creation of ionic defects in transition-metal-free oxides with K2NIF4 structure	Acta Materialia	reuse in a thesis/dissertation	Completed	<a href="#">4147780427736</a>
14-Jul-2017	Thermal transport across metal silicide-silicon interfaces: An experimental comparison between epitaxial and nonepitaxial interfaces	Physical Review B	Thesis/Dissertation	Completed	<a href="#">4147780295370</a>
14-Jul-2017	Thermal transport across metal silicide-silicon interfaces: First-principles calculations and Green's function transport simulations	Physical Review B	Thesis/Dissertation	Completed	<a href="#">4147771440657</a>
14-Jul-2017	Transient thermoreflectance from thin metal films	Journal of Applied Physics	Thesis/Dissertation	Completed	<a href="#">4147771029039</a>